Rotordynamic Forces Generated by Annular Leakage Flows in Centrifugal Pumps

Thesis by

Yun Hsu

In Partial Fulfillment of the Requirements

for the Degree of

Doctor of Philosophy

California Institute of Technology

Pasadena, California

2001

(Defended May 1, 2001)

Acknowledgements

I would like to thank my advisor Professor Christopher Brennen for his invaluable guidance and support during my studies at Caltech. I would also like to thank Professors Fredric Raichlen, Allan Acosta, Melany Hunt, and Tim Colonius for reviewing my thesis.

John Van Deusen and Rodney Rojas of the Mechanical Engineering Shop provided much help in the construction of test articles and maintenance of the facility. Special thanks to Rodney for his machining of the pitot tubes. I would also like to express my gratitude to Dana Young, Lynn Burgess, and Connie Yehle for their help with administrative matters.

The guidance provided by Robert Uy in helping me get started in running the lab is much appreciated. I would like also to thank Annan Karion and Gustavo Joseph for their help in computer and system administration tasks, and Fabrizio D'Auria for his work on effects of bubbly flows on rotordynamic forces.

To all my friends at Caltech I say thank you. And to my parents, thank you for your unconditional support and encouragement during my stay at Caltech.

Abstract

Fluid-induced rotordynamic forces in pumping machinery are well documented but poorly understood. The present research focuses on the rotordynamics due to fluid flow in annuli, in particular, the discharge-to-suction leakage flow in centrifugal pumps. There are indications that the contribution of the front shroud leakage flow can be of the same order of magnitude as contributions from the nonuniform pressure acting on the impeller discharge. Previous investigations have established some of the basic traits of these flows. This work furthers the experimental and computational approach to quantify and predict the shroud contribution to the rotordynamic stability of pumping machinery.

Childs' bulk flow model for leakage paths is carefully examined, and convective relations for vorticity and total pressure are deduced. This analysis leads to a new solution procedure for the bulk flow equations which does not resort to linearization or assumed harmonic forms of the flow variables.

Experimental results presented show the contributions of the inlet swirl velocities to the rotordynamic forces. Antiswirl devices are evaluated for their effectiveness in reducing instability. Additional tests measuring the pressure distributions and the inlet swirl velocities of the leakage flow confirm some of the predictions by numerical analysis.

Contents

List of Figures

Nomenclature

B	Depth of logarithmic spiral channel on swirl vane
C	Direct damping coefficient, normalized by $\rho\pi\Omega^2 R_2^2 L\varepsilon$
c	Cross-coupled damping coefficient, normalized by $\rho\pi\Omega^2 R_2^2 L\varepsilon$
F_n	Force normal to whirl orbit normalized by $\rho\pi\Omega^2 R_2^2 L\varepsilon$
F_t	Force tangent to whirl orbit normalized by $\rho\pi\Omega^2 R_2^2 L\varepsilon$
g_S, g_R	Shear stresses in rotating coordinate system on the stator and rotor respectively
H	Clearance between impeller shroud and housing
h	Film thickness in Hir's Model
K	Direct stiffness coefficient, normalized by $\rho\pi\Omega^2 R_2^2 L\varepsilon$
k	Cross-coupled stiffness coefficient, normalized by $\rho\pi\Omega^2 R_2^2 L\varepsilon$
L	Axial length of the impeller
M	Direct added mass coefficient, normalized by $\rho\pi\Omega^2 R_2^2 L\varepsilon$
m	Empirical frictional exponent in Hir's Model
m_r, m_s	Empirical frictional exponent for rotor and stator respectively
n	Empirical frictional constant for Hir's Model
n_r, n_s	Empirical frictional constants for rotor and stator respectively

P	Total pressure, defined in a rotating coordinate system in equation (4.11)
p	Static pressure
Q	Volumetric leakage flow rate
R	Radius of the rotor
R_2	Tip radius of rotor and leakage inlet
s	Path coordinate
u_s	Gap averaged leakage path velocity of fluid
u_Θ	Gap averaged circumferential velocity of fluid in fixed frame
u_θ	Gap averaged circumferential velocity of fluid in rotating frame
α	Turning angle of logarithmic spiral channel on swirl vane
Γ	The vorticity defined by equation (4.14)
ε	Eccentricity of whirl orbit
η	Dynamic viscosity in Hir's Model
Θ	Circumferential coordinate of the bulk flow model in fixed frame
θ	Circumferential coordinate in steady frame
Λ	Leakage inlet swirl ratio, $u_\theta/\Omega R_2$
ν	Kinematic viscosity
ξ	Streamline coordinate
ρ	Fluid density
τ	Wall shear stress in Hir's Model
τ_{Ss}, τ_{Rs}	Wall shear stress terms in the s direction acting on the stator and rotor respectively
$\tau_{S\theta}, \tau_{R\theta}$	Wall shear stress terms in the θ direction acting on the stator and rotor respectively
ϕ	Leakage flow coefficient, $u_s/\Omega R_2$ or $Q/2\Pi\Omega R_2^2 H$

ψ	Stream function defined in equation (4.9)
Ω	Main shaft radian frequency
ω	Whirl radian frequency

Chapter 1 Introduction

1.1 Background

Fluid-induced rotordynamic forces play an important role in the design of turbomachines. They occur as the result of movement in the axis of rotation of the impeller-shaft system of the turbomachine. General knowledge of the characteristics of these fluid forces are still incomplete, and they remain poorly understood. With increasing power requirements demanding increases in the rotational speeds of modern turbomachines, problems associated with rotordynamic forces will increase as the forces typically scale with the square of the rotational velocity. Fluid-induced forces altering the expected performance of undersea oil re-injection compressors, boiler feed pumps, and rocket engine pumps have motivated investigations of these fluid/structure interaction problems in order to provide sufficient information to predict the magnitude of destabilizing forces for the design process.

Ideally a turbomachine should operate where the centerline of its rotating part, or rotor, coincides with the machine axis of rotation at all times. This requires either all structures (rotor and stator) to be perfectly rigid and aligned, or that all loads have a perfectly symmetric distribution. All real turbomachines operate with vibrations in the rotor from load imbalance. Fluid flow induced by such vibrations, or whirls, will generate forces acting on solid surfaces in the lateral plane, from the non-axisymmetricity both in the pressure distributions and in the momentum fluxes. These forces are commonly referred to as rotordynamic forces. An example of the fluid forces acting on a seal displaced from a concentric position is depicted in figure 1.1. For low Reynolds number flows where viscous forces dominate, the fluid forces will be restoring, acting to reduce the eccentricity (Reynolds number of order 1 and less). For high Reynolds number flows, however, the sign of the fluid force is reversed and it will instead act to magnify the eccentricity. At high Reynolds numbers, higher

velocity means lower pressure; therefore the pressure at the side where the clearance is smaller is lower and there will be a net force acting on the rotor in the direction of the displacement. It is apparent that these rotordynamic forces can decrease the critical speed of the system, which often results in major shortfalls in performance.

Rotating machines have many possible sources of fluid-induced rotordynamic forces. In a centrifugal pump, the fluid forces acting on journal bearings, wear rings, and balance pistons must all be estimated, though often the analysis is incomplete. Geometric imperfections from manufacturing, such as a deviate vane, would also contribute to the total fluid forces. Among these elements, journal bearings have been studied most extensively. This has been accompanied by progress in the study of fluid forces on annular pressure seals.

Flow in the discharge to inlet leakage path of a shrouded centrifugal pump also induce fluid forces and are known to be a significant source. As a centrifugal pump lets fluid into the spinning impeller and discharges it at a higher pressure, some of the exiting fluid will flow back toward the low pressure inlet side through the leakage path between the front impeller shroud and the outer casing of the pump, depicted in figure 1.2. The geometry of the leakage path is somewhat similar to that of an annular seal except for the varying radii. Thus similar rotordynamic forces will arise.

The contribution of the rotordynamic forces from leakage flows has been studied experimentally, but its effects are still not well predicted by the models adapted from the turbulent annular seals. Time and cost make a full three-dimensional computational fluid dynamic code impracticable. This thesis offers a new approach to the computation of rotordynamic forces in the leakage path based on previous models.

1.2 Notation

Rotordynamic forces can have significant influence on the dynamic behavior of a system with a rotating shaft. The shaft speeds at which large displacements occur between the rotor and its centered rotational axis are usually termed the critical speed. Fluid induced forces may lower the critical speed dramatically, causing unforeseen

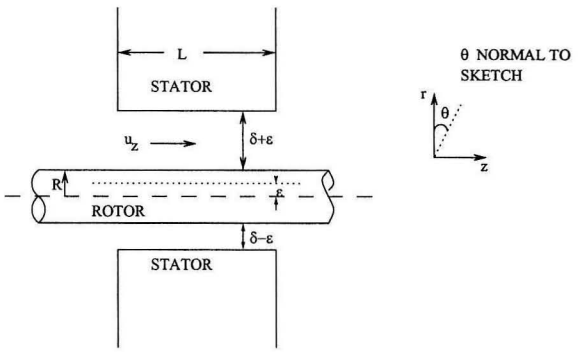

Figure 1.1: Seal demonstrating the inertia effect

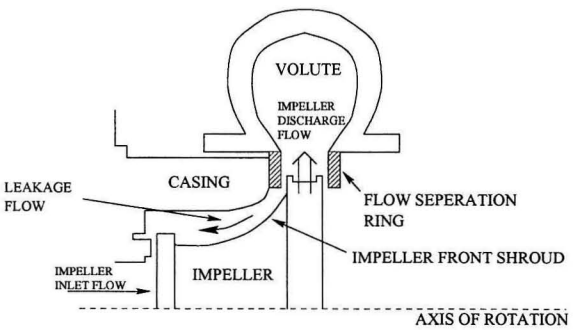

Figure 1.2: Impeller stage

limitations to the operating range.

The set of forces concerned are those caused by the displacement of the axis of rotation. Figure 1.3 shows the rotor, spinning at a speed of Ω, displaced to a distance ϵ from a fixed center. Assuming a small displacement, the fluid forces can be written as

$$\begin{Bmatrix} F_n \\ F_t \end{Bmatrix} = \begin{Bmatrix} F_{ox} \\ F_{oy} \end{Bmatrix} + [A] \begin{Bmatrix} x(t) \\ y(t) \end{Bmatrix} \tag{1.1}$$

where the displacement is given by $x(t)$ and $y(t)$, and $[A]$ would be independent of time in a linear model. Figure 1.3 depicts forces that the fluid imparts on the rotor in a plane perpendicular to the axis of rotation. F_{ox} and F_{oy} are referred to as radial forces; they are independent of rotor displacement and would be present even if the rotor is perfectly centered. Fluid can also exert forces on the rotor in a axial direction, a thrust, and also moments in various directions. Those are outside the scope of the present work.

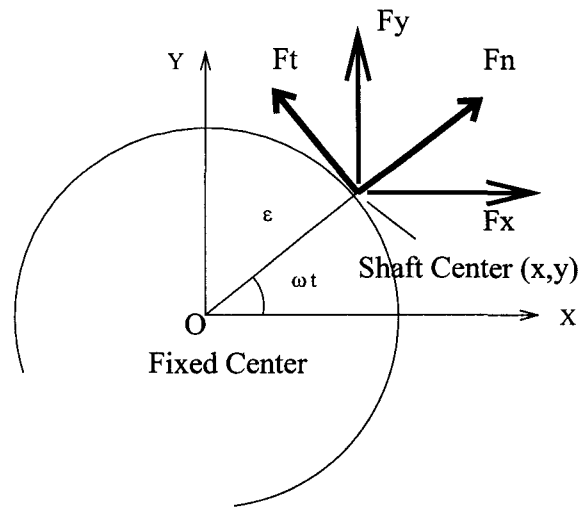

Figure 1.3: Force diagram in plane normal to the shaft axis

It is conventional for rotordynamists to decompose the function $[A]$ into

$$[A]\begin{Bmatrix} x(t) \\ y(t) \end{Bmatrix} = [M]\begin{Bmatrix} \ddot{x} \\ \ddot{y} \end{Bmatrix} + [C]\begin{Bmatrix} \dot{x} \\ \dot{y} \end{Bmatrix} + [K]\begin{Bmatrix} x \\ y \end{Bmatrix} \tag{1.2}$$

where $[M]$, $[C]$, $[K]$ are two-by-two constant matrices termed the hydrodynamically-induced mass, damping and stiffness matrices. Because the dynamics for the overall system are generally modelled by a linear system in a similar matrix form for the calculation of eigenfrequencies, the advantages for presenting the forces in this form are obvious. Since the rotordynamic forces would be the forcing functions in the equations for system dynamics, these hydrodynamically-induced matrices will just be incorporated into the dynamical matrices for the overall system.

Under the assumption of rotational invariance, the three rotordynamic matrices become

$$[M] = \begin{bmatrix} M & m \\ -m & M \end{bmatrix}; \quad [C] = \begin{bmatrix} C & c \\ -c & C \end{bmatrix}; \quad [K] = \begin{bmatrix} K & k \\ -k & K \end{bmatrix}$$

thus reducing the number of coefficients to six. This allows for another way to describe the coefficients. If the rotor center is rotating about the fixed center at a constant

speed ω, then the normal and tangential forces as defined in figure 1.3 become

$$F_n = M\left(\frac{\omega}{\Omega}\right)^2 - c\left(\frac{\omega}{\Omega}\right) - K \tag{1.3}$$

$$F_t = -C\left(\frac{\omega}{\Omega}\right) - k \tag{1.4}$$

and the dimensionless coefficients are termed the direct added mass (M), direct damping (C), cross-coupled damping (c), direct stiffness (K), and cross-coupled stiffness (k). The cross-coupled added mass (m) is generally very small, and is often disregarded. This provides an easier way to measure the coefficients experimentally and is the method used in the present thesis.

From a stability standpoint, a positive normal force F_n will increase the eccentricity and is therefore destabilizing. Negative direct stiffness coefficient therefore indicates destabilizing effects. Less stability would tend to suggest a lower critical speed of the overall system. When the whirl frequency ratio, ω/Ω, is positive, a positive tangential force F_t would be destabilizing since it would increase the forward whirl. The tangential force is generally more important in the design process since it is difficult to lessen its destabilizing effect. A convenient measure of rotordynamic stability is the ratio of cross-coupled stiffness to the direct damping, or simply k/C, which is termed the whirl ratio. This defines the range of whirl frequency ratios where the tangential forces is destabilizing since F_t is positive for $0 < \omega/\Omega < k/C$.

1.3 Literature Survey

Fluid forces on a centrifugal pump impeller are the sum of the shroud forces caused by pressure on external surface of the impeller shrouds and the volute section, and of the lateral forces due to a net momentum flux leaving the impeller. Many early experiments did not measure these contributions (Bolleter *et al.* , 1987; Jery, 1986). The lateral force is generally caused by impeller blade interaction with the volute and non-uniformities in discharge. Experiments done by Ohashi and Shoji (1987) report that the tangential component of the lateral forces was largely stabilizing.

Destabilizing forces occurred only when impeller operated above twice the critical speed and at partial flow rate. Research in this area generally used unsteady potential theory (Shoji & Ohashi, 1987; Fongang *et al.* , 1998), and some qualitative agreement with experimental results was found.

Various seals of the pump also induce rotordynamic forces; they are by far the most studied component. Experiments include measurements of forces (Nordmann & Massmann, 1984; Marquette, 1995), flow fields and shear stresses (Morrison *et al.* , 1991; Morrison *et al.* , 1996), of both the plain annular and the labyrinth seal. Leakage flows along the back shroud of an impeller can be important in multi-stage pumps where such leakage flows are possible. This type of flow and the resulting fluid moments have been examined experimentally (Tsujimoto *et al.* , 1997).

On the opposite side, the forces on the front shroud from the flow in the discharge-to-suction leakage path have also been examined. Bolleter (1987; 1989) measured and quantified some effects of the leakage flow on the unsteady forces acting on a centrifugal pump. A radial clearance wear ring, however, contributed significantly to the shroud forces. To isolate the effects of the leakage flows along the front shroud, Guinzburg (1992), using a solid rotor to model the front shroud of an impeller, examined the effects of eccentricity, rotational speed, and shroud clearance on the rotordynamic forces. Because Guinzburg tested a conical impeller, Uy (1998) examined the effects of the geometry of the leakage path by using two contoured impellers whose external profiles were more characteristic of modern centrifugal pump impellers. These were tested with various front and back seal configurations.

Comparison of the tests conducted by Guinzburg and Uy show relatively little effect of the curvature in the leakage path due to impeller profile. The effects of low pressure and high pressure seals at both ends of the leakage path are very significant and can be either stabilizing or destabilizing depending on design. The effects of small eccentricity and shaft speed on rotordynamic forces can both be scaled with the correct non-dimensionalization, and the fluid forces were roughly inversely proportional to clearance.

Much progress has been made in the study of annular pressure seals (Black, 1969;

Childs, 1983a; Nordmann & Massmann, 1984). One of the simpler computational models is the bulk flow model first proposed by Hirs (1973) and modified by Childs, who identified the necessity of the inertial terms in modeling the forces (Childs, 1983a), and the sensitivity to inlet swirl (Childs, 1983b).

The bulk flow model for the seal describes the gap-averaged flow between two cylinders and is thus two-dimensional, in the meridional direction and the tangential direction. This assumes that the velocity profiles within the annular region are self-similar and can be averaged without excessive error. Shear stress effects are only considered at the fluid-solid interfaces. Thus the bulk flow equation can be seen as the Euler's equation with four added terms to account for the shear stresses exerted by the two solid surfaces and acting on the fluid in the meridional and tangential directions.

The Childs perturbation method solved the bulk flow equations by assuming a harmonic perturbation of the flow field of a system without eccentricity (a perfectly centered seal). The results are now widely used for annular seals.

Since the geometry of the leakage flow is very similar to that of an annular seal, the Childs bulk flow equations were adapted to study shroud forces (Childs, 1989). For forces on the back shroud (Tsujimoto *et al.* , 1997), the model showed good agreement with experimental results. Unsteady wall shear stress terms had little effect on the flow in the passage, but the tangential swirl velocity was critical to the success of the model.

For fluid forces on the front shroud, the bulk flow has proven to be useful but is still inadequate in the prediction of the rotordynamic forces. One of the more contentious results was its prediction of resonant like behavior at certain positive whirl frequency ratios (Childs, 1989). Experiments showed no such resonances. To examine the limitations of the bulk flow model in the leakage flows, Sivo (1994b) took measurements of the flow field inside the leakage path using a laser Doppler velocimeter. Regions of flow recirculation and reversal were noted, especially close to the impeller near the tip. Other researchers have found similar results (Guelich *et al.* , 1989). The bulk flow model predicted that increased pre-rotation of fluid into

the leakage path will increase the destabilizing effects of rotordynamic forces. For this reason, Sivo (1995) examined the effects of swirl reduction devices in the leakage path. Grooves and brakes in the leakage path seemed to offer some help at reducing the rotordynamic forces for small flow coefficients.

Other models have been used to calculate the forces induced by leakage flow. Baskharone and Hensel (1991) devised a deformable finite element model, which proved capable of predicting flow reversals in the leakage flow. The Baskharone model still assumed a harmonic perturbation of the pressure field, but the zeroth order equation was an axisymmetric flow instead of a one-dimensional one. The model, however, was not able to predict the rotordynamic forces with any better accuracy. The model has since been expanded to examine the effect of flow interactions between pump primary flow and the leakage flow on rotordynamic forces (Baskharone & Wyman, 1999).

1.4 Taylor Vortices and Reynolds Number Effects

Before modelling these flows, one should examine the nature of fluid flows in annular regions. For Couette flows, one nondimensional number that must be considered is the Taylor number. The Taylor number for a typical leakage flow experiment is $Ta = 2 \times 10^7$ with it defined as

$$Ta = R_2 H^3 \frac{\Omega^2}{\nu^2} \tag{1.5}$$

where R_2 is the tip radius of the impeller, H the leakage path clearance, and Ω is the shaft frequency of the impeller. A critical Taylor number around 1700 denotes the transition region from laminar to Taylor vortex flow (Bjorklund & Kays, 1959), and hence different mechanisms of momentum and heat transfer. Above the critical Taylor number, momentum transfer occurs in sublayers close to the surface. While some experimental evidence from Sivo (1994) shows path velocity reversal that may indicate this type of rotating vortex pattern in the leakage path, the reversal is isolated

near the inlet area.

The typical value for transition to turbulence in a Taylor Couette flow is $Ta \approx 160000$, but some works have examined flow fields at $2.1 \times 10^7 < Ta < 5.5 \times 10^9$ and $7300 < Re_\Omega < 120000$ (Smith & Townsend, 1982), where $Re_\Omega = \Omega R_2/\nu$. Smith and Townsend reported the presence of large toroidal eddies at $Re_\Omega < 30000$ in the flow between concentric cylinders, and also that the coherence of the eddies disappears into fully irregular turbulent flow for values of Reynolds number above that. The experiments used an axial flow of about 1% of the rotational speed, and had a clearance equal to half the inner cylinder radius. A typical leakage flow experiment with a flow coefficient of $\phi = 0.06$ has an axial flow of the same order of magnitude but has a much smaller clearance between the solid surfaces, and Reynolds number $Re_\Omega \approx 30000$. Smith and Townsend also noted that the intensity of toroidal components compared to those of irregular turbulence motion decreased rapidly with increased speed above Reynolds numbers of 2×10^4. A later paper by Townsend (1984) found that toroidal eddies though more helical in shape still existed for values of Reynolds number above 30000. But the decrease in the energy of these eddies for increased speed still held true, and that the wall shear stresses were all unidirectional. It therefore is likely that the dominant flow field in the leakage flow experiments and the applications has incoherent structure of turbulent flows.

1.5 Research Objective

The objective of this research was to develop a computational method for calculating the rotordynamic forces induced by the discharge to suction leakage flows of centrifugal pump impellers. This was then extensively used for insights into the physical nature of rotordynamic flows. A new solution approach to the model is proposed with few assumptions about the functional form of the flow variables.

Experimental data for the rotordynamic forces induced by the discharge-to-suction leakage flow will also be presented. A more typical leakage flow geometry will be examined as well as the effects of swirl reduction devices. Some experiments previously

conducted at Caltech were examined in detail. Moreover, new experiments to measure the pressure distribution and the inlet swirl velocities of the leakage flow were conducted in order to carry out a more accurate comparison with the model.

Chapter 2 Test Apparatus

2.1 Rotor Force Testing Facility

The experiments described in this work were conducted in the Rotor Force Testing Facility at the California Institute of Technology. The apparatus has been in existence in one form or another for over 20 years (Ng, 1976), and has been used for many tests of turbomachinery and related components.

The current form of the facility (see figure 2.1) was configured by Jery (1986) to measure both the steady and unsteady forces on whirling pump impellers. In experiments, the rotor is forced to move in a circular whirl orbit of prescribed frequency and amplitude (eccentricity). To accomplish this, an eccentric drive was built to apply a whirl motion to the rotating main shaft. Thus fluid forces could be measured without having to approach the critical speed of the system. The eccentric drive is used to impose a circular whirling motion onto the main rotation of the impeller; the radius of the whirl (eccentricity) can be varied. With a separate whirl motor, the speed of the whirl orbit is varied through a range of subsynchronous (less than the main shaft speed) whirl frequencies from negative to positive values.

In the main flow loop (figure 2.1), the air bladder (airbag) and heat exchanger can be used to set the pressure and temperature, though neither was used in the present experiments. The working fluid is water containing sodium chromate for corrosion inhibition, and pH balanced by potassium chloride.

The auxiliary pumping unit pumps the water through the loop and the test section. The unit contains a digital flow meter and bypass loops with valves for manual adjustment of the flow rate, replacing the turbine flow meter and the silent throttle valve in the main loop. Smoothing sections exist both upstream and downstream of the test section. During experiments, inside the test section, an impeller is mounted onto the force balance and the main shaft, and it is spun as some fixed speed. Water

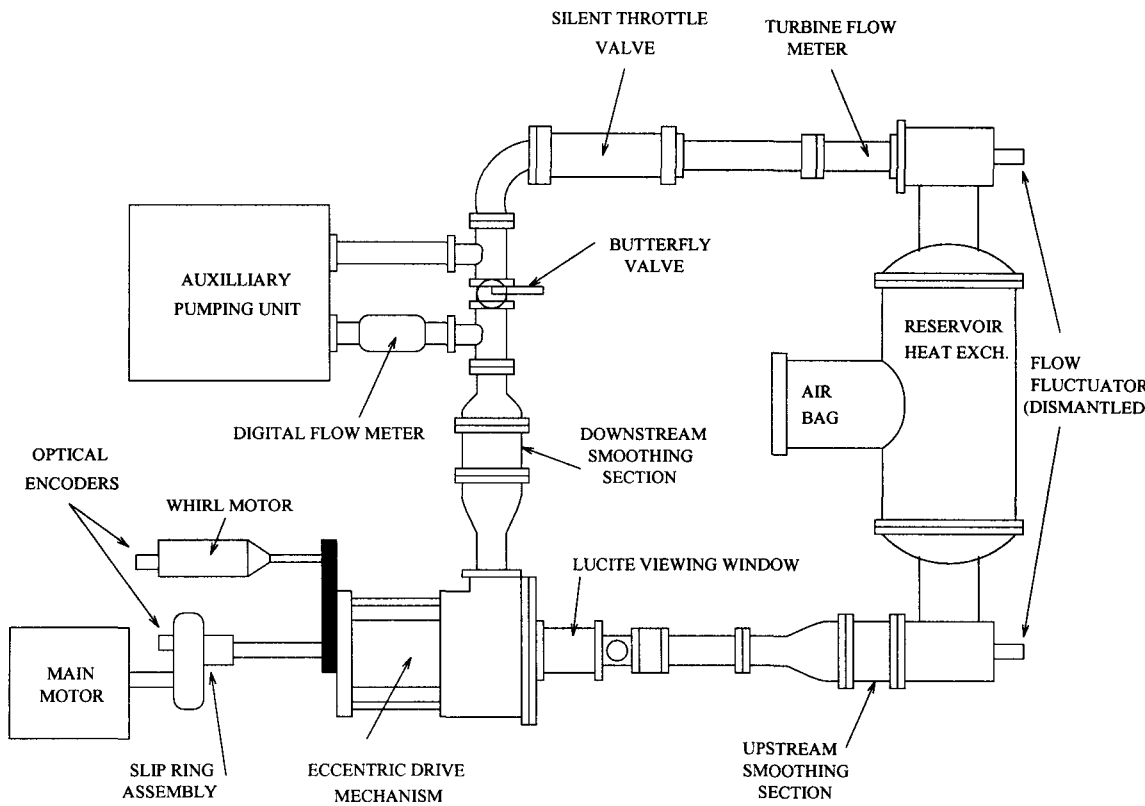

Figure 2.1: Schematic of the Rotor Forces Testing Facility, from Uy (1998)

is pumped from the tip of the rotor, where it has its maximum diameter, to the eye of the solid impeller through only the annular region between the stator and the rotating impeller. The center of the rotor is at a fixed eccentricity to the center of the stator mounted on its outside. As seen in figure 2.2, the main shaft rotates inside a double bearing system, in which the inner bearings are eccentric to the outer ones. Therefore when the auxillary motor rotates the whirl shaft via a chain/sprocket wheel, the main shaft constrained by the inner bearings will be rotating in an eccentric orbit. The digitally controlled auxiliary motor shaft connected to the chain/sprocket wheel drives the whirl motion to be synchronous with the main shaft rotation. The setup will provide a shaft whirling in a circular orbit, much like that diagrammed in figure 1.3 and described in section 1.2.

Both the $15kW$ DC main motor, offering speeds of up to 3000 rpm, and the $1.5kW$ DC whirl motor are driven with feedback controller systems that are coupled

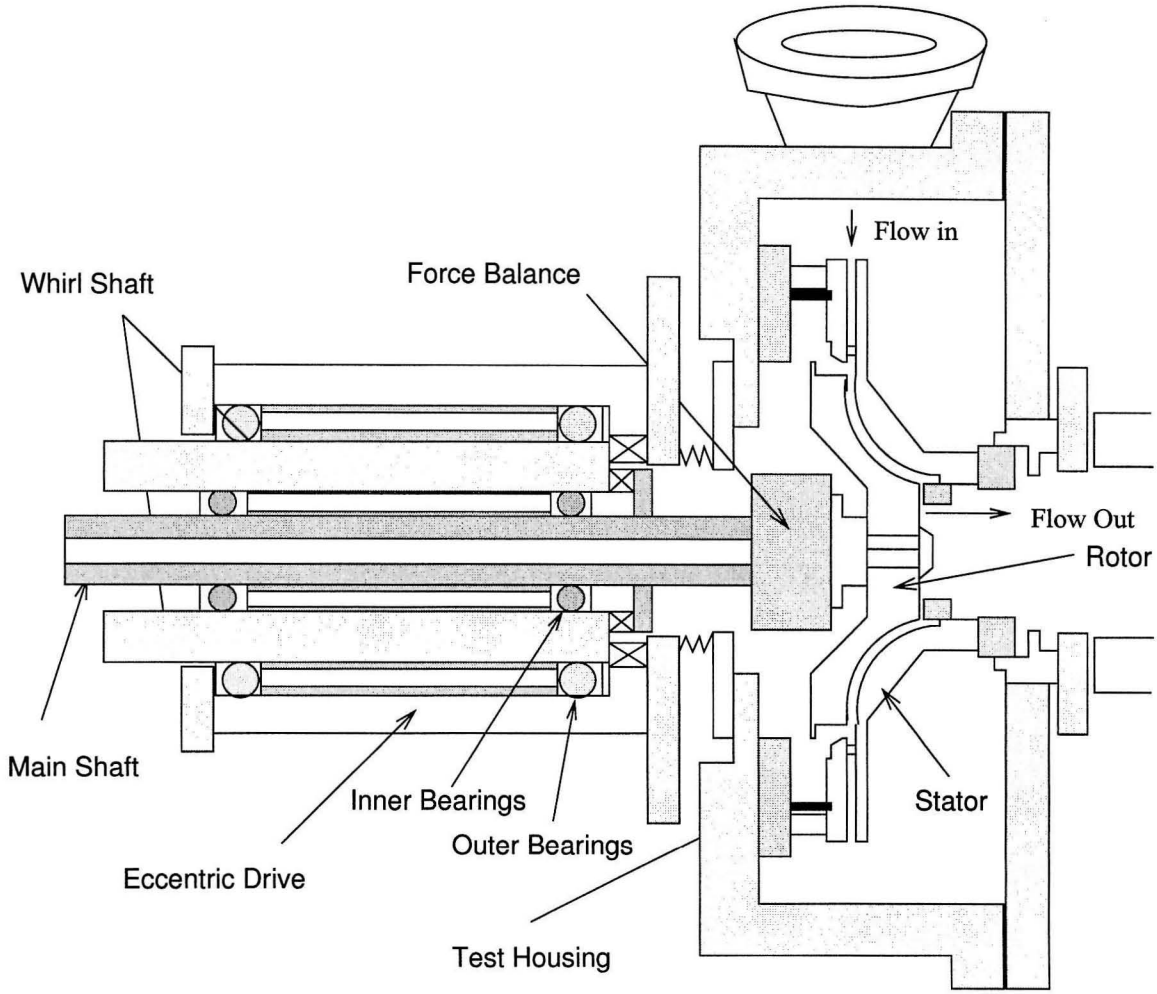

Figure 2.2: Main test section showing the eccentric drive with contoured impeller

to a data acquisition system. The force measurements come from an internal balance connected to the rotating rotor that measures the forces directly on the rotor. The rotating dynamometer inside the force balance involves nine strain-gage bridges which measure all six force components on the impeller. The construction, operation, and calibration of a six force component internal force balance are described in detail in Jery (1986).

In order to isolate the effects of the leakage flow, solid rotors were employed for all the present tests. Force contributions from blade interaction with the volute are therefore negated. The dummy impeller attempts to model the front clearance of a typical shrouded centrifugal impeller as closely as possible. In these tests, fluid is

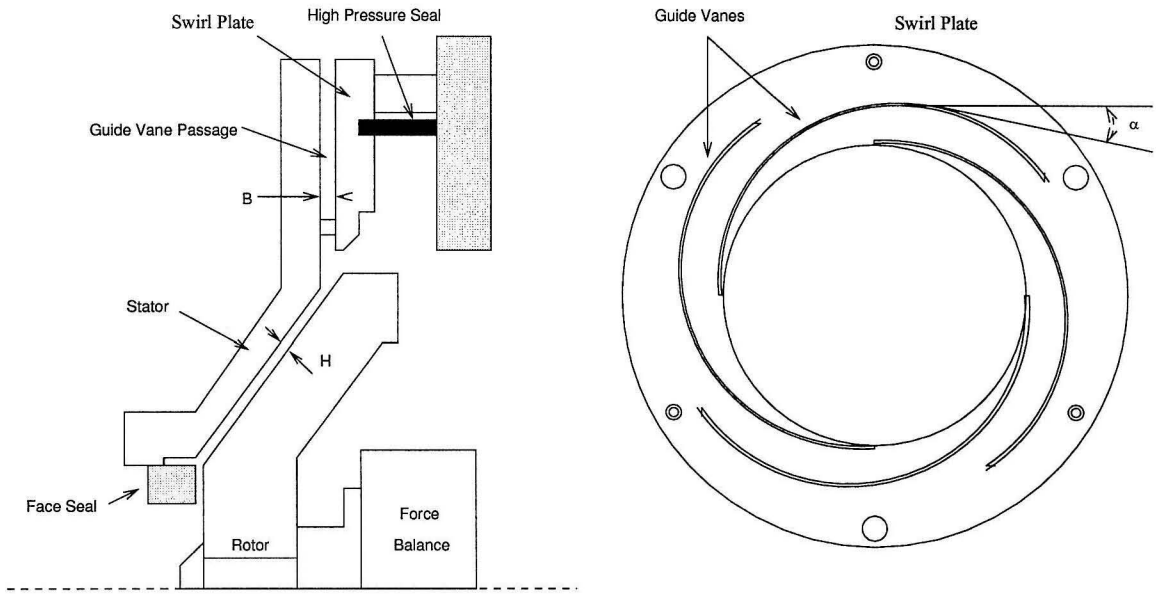

Figure 2.3: Swirl plate geometry

forced from the clearance at the tip of the impeller and the stator, the larger end, to the clearance at the eye. A suitable range of leakage flow rates was chosen for the tests.

2.2 Leakage Path

Experiments to compare different geometries of the pump discharge-to-inlet leakage paths were conducted in the Rotor Force Test Facility. The different leakage flow configurations are shown in figure 2.4. The conical shroud with a straight 45 degree leakage path was the first one built and has been extensively tested (Guinzburg, 1992; Sivo *et al.* , 1995). Along its stator, there exist numerous pressure taps to facilitate pressure measurements. The contoured impeller was constructed by Uy (1998) to match the axial length and the eye-to-tip ratio of the conical model while having a more typical centrifugal pump geometry. A third rotor and stator were made to model the leakage path of the Space Shuttle Main Engine High Pressure Oxidizer Turbopump Impeller as closely as possible. This has a much shorter axial length and a much larger eye-to-tip ratio.

The geometry of the contoured rotors are such that their profiles are parallel to

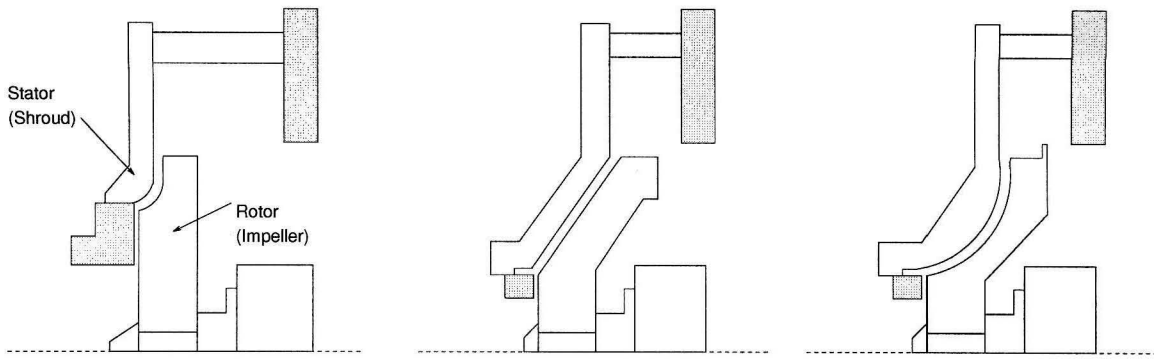

	Short Contoured Rotor	Conical Rotor	Contoured Rotor
Path	3rd order polynomial	45 degree straight	3rd order polynomial
Eye/tip diameter	.700	.474	.474
Axial length/ tip diameter	.088	.268	.229

Figure 2.4: Test matrix of rotor geometries

the centerline at the eye and perpendicular to the centerline at the tip. The stators were constructed to maintain a constant nominal normal clearance of 0.30 cm. The tip or outer radii of all the dummy impellers are the same.

The low pressure side of the leakage path corresponds to the inlet or suction side of a normal centrifugal pump. The high pressure side corresponds to the discharge of a typical pump. Seals can be installed on both ends of the leakage path. Their effects on rotordynamic forces were examined by Uy (1998). In the current tests, only a low pressure seal is present. An axial clearance device that models a typical face seal on a centrifugal pump is used, as shown figure 2.4. The distance from the inner radius of the axial clearance seal to the impeller eye radius is $1.14cm$; its clearance was set to $0.05cm$ for all the tests, but could be varied if necessary.

2.3 Inlet Guide Vanes

The bulk flow model (Childs, 1983b) predicts significant effects of the inlet swirl rate on the magnitude of rotordynamic forces. Experimentally the effect of inlet swirl

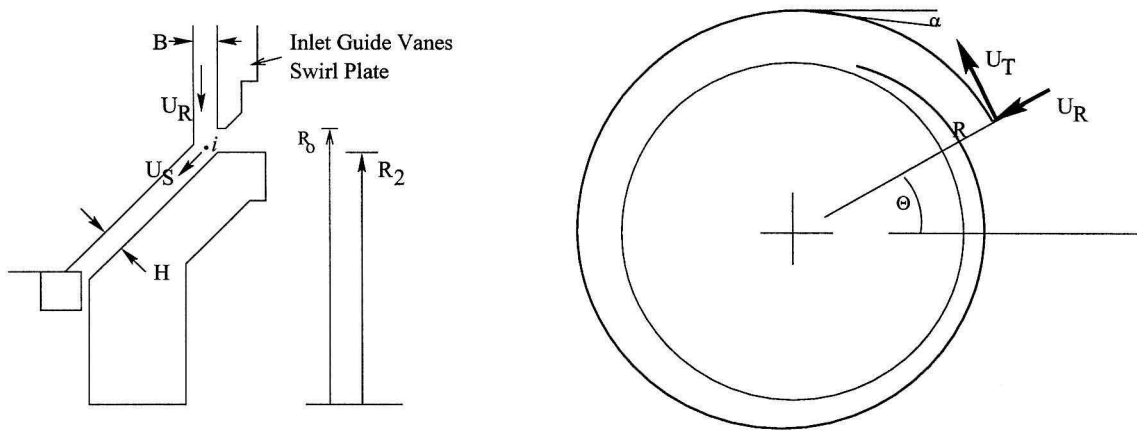

Figure 2.5: Swirl plate geometry

was examined by installing a swirl plate at the leakage inlet to induce pre-rotation. Figure 2.3 shows a standard vane with a logarithmic spiral channel of a constant turning angle, and its installation relative to the rotor and stator. Three inlet swirl plates with vanes of different turning angles were built to vary the rate of inlet swirl as the fluid enters the leakage path. The desired inlet swirl ratio, Λ (ratio of the leakage flow circumferential velocity to the impeller tip velocity) is calculated as follows.

Assume the fluid will be constrained to flow parallel to the inlet guide vanes, then the relationship between the vane angle, α (figure 2.3), and the fluid velocities, U_R and U_T, will be

$$tan\ \alpha = U_R/U_T \tag{2.1}$$

where U_R and U_T are defined to be the velocity components at the discharge from the inlet guide vanes. Equation 2.1 assumes the fluid flow exits the inlet passage parallel to the inlet guide vanes. We note that the solidities of the inlet guide vane geometry range from 5 to 10, well above the value of 2 which is normally required to constrain the flow to follow the vanes. However, the present passages are very thin axially and viscous effects on the end walls could change the flow substantially. This issue will be discussed further in later sections.

The continuity equation yields the following:

$$R_o B U_R = R_2 H U_S \tag{2.2}$$

where R_2 is the tip radius of the impeller, R_o is the radius of the swirl plate on flow discharge side, H is the leakage path clearance, B is the breadth of the inlet swirl passage, and U_S is the meridional velocity at inlet to the leakage path (see figure 2.5).

From the conservation of angular momentum,

$$R_o U_T \dot{m} = R_2 U_\Theta \dot{m} \tag{2.3}$$

where U_Θ is the tangential velocity at the leakage path inlet and $\dot{m}$ is the mass flow rate. Equation 2.3 assumes there are no frictional effects; the validity of this is not at all certain. As shown in figure 2.5, there exists a gap between the discharge from the inlet guide vanes and the beginning of the leakage path, leading to a small chamber behind the impeller. The effect that has on the fluid flow is unknown.

If all of the above equations hold, then at inlet to the leakage path

$$\frac{U_\Theta}{U_S} = \frac{U_T}{BU_R/H} \tag{2.4}$$

$$= \frac{U_T}{U_R}\frac{H}{B} \tag{2.5}$$

$$= \frac{H}{B tan\ \alpha} \tag{2.6}$$

Since both inlet velocities are non-dimensionalized by the impeller tip velocity, equation (2.6) becomes

$$\frac{\Lambda}{\phi} = \frac{H}{B tan\ \alpha} \tag{2.7}$$

where ϕ and Λ are the flow coefficient and the inlet swirl ratio, respectively. The flow coefficient is the nondimensionalized flow rate, $U_{Si}/\Omega R_2$, and the inlet swirl ratio is the nondimensionlized inlet velocity the circumferencial direction, $U_{\Theta i}/\Omega R_2$, where i denotes inlet to the leakage path. Therefore, for the same inlet guide vane, increasing the flow rate will also increase the inlet swirl. Vanes with 1^o, 2^o, 6^o turning angles were constructed to allow variations of α or ϕ while maintaining the same inlet swirl rate. Uy (1998) conducted extensive tests examining the effects of inlet swirl for the contoured impeller geometry.

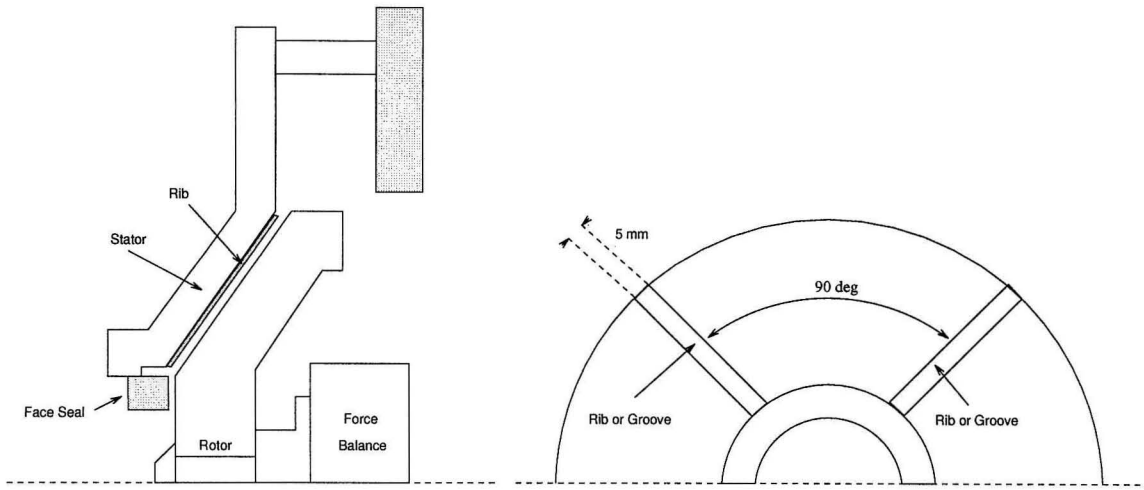

Figure 2.6: Swirl reduction devices

The above was the theory behind the design and installation of the guide vanes. As will seen in section 3.5, the vanes failed to act in the anticipated fashion. This was discovered only after the publication of early experimental results (Uy *et al.* , 1998).

2.4 Swirl Reduction Devices

We now turn attention from inlet swirl to swirl reduction in the leakage path by vanes installed within the passage. Previous investigations (Sivo *et al.* , 1994a) demonstrated some benefits from fitting anti-swirl ribs to the surface of the stator, as it decreased destabilizing forces. The inner surface of the conical stationary shroud is designed to accept meridional ribs or swirl brakes along the length of the leakage path. As shown in figure 2.6, four equally spaced ribs, $0.5cm$ wide and $0.16cm$ high, were installed for these tests. The effectiveness of cutting grooves on the stator surface was also examined. For these tests, the grooves cut duplicated the height and width of the brakes.

2.5 Force Measurements

Various main shaft speeds were used for the experiments, although most were conducted with a speed of $1000rpm$. For each set of measurements, a series of sub-synchronous whirl frequency tests were conducted, ranging from a whirl frequency ratio of -0.7 to +0.7. This was done by changing the output of the frequency divider box (Jery, 1986). The phase of the main and whirl motors, important in assuring correct force measurements, was checked using a strobe lamp.

The force measurement are obtained using a data acquisition system connected to strain gage amplifiers. A clock signal from the frequency divider box is also sent to the data acquisition system to ensure accurate timing. Samples of 128 points per cycle are taken for all strain gages and averaged over 256 cycles, where each cycle is an integral number of revolutions of the whirl motor. Data is then processed and reduced to the normal and tangential rotordynamic forces for each frequency ratio, normalized by $\rho\pi\Omega^2R^2L\epsilon$, which involves the tip speed, ΩR, and the axial length of the impeller, L, as well as the eccentricity, ϵ. The internal force balance is calibrated using a system of weights and pulleys, applying static loads for all six components of force. The calibration is then checked by running the dynamometer with the mounted rotor and recording the steady force component, which should equal the weight of the rotor.

Two runs are conducted for each test, a "dry run" where the working fluid is air, and a "wet run" when the rotor is submerged in water. Isolation of the fluid forces is done by subtracting the "dry run" results from the "wet run" data. The buoyancy force of the impeller is also subtracted from the data.

For the conical impeller, static pressures in the leakage flow along the stator surface were measured by attaching tubes to the various pressure taps and connecting them to inverted water manometers located outside of the test section. Pressure data could then be hand recorded. Tests using pitot tubes to measure the inlet swirl velocities were also conducted, and the stagnation pressures of the pitot tube were recorded using the same set of manometers.

2.5.1 Pitot Tube Installation

Questions arose during the investigations about the flow field at inlet to the leakage path, see section 5.2 for details. Pitot tubes were therefore installed to measure the flow velocities at the inlet. Considerations were given to the measurement of the flow angle, using five-hole pitot tubes for example. This was not done, however, for several reasons. The flow velocities are likely to vary as a function of distance away from the wall. This would mean that several measurements at different distances away from the wall would be needed to accurately access the flow, a difficult feat considering the tight confining spaces in the apparatus. In addition the flow is unsteady and highly disturbed, making the accuracy of flow angle measurements a concern. Because of this, it was decided that a cruder measurement of only the velocity in the tangential direction would suffice for the purposes of ascertaining the inlet flow conditions to the leakage path.

The stator had two holes drilled through for the insertion of pitot tubes, as shown in figure 2.7. The pitot tubes were placed immediately after the exit of the inlet guide vanes and before entrance into the leakage path, a gap of approximately $0.8cm$ normal to the axis of rotation. Normally one would have the diameter of the pitot tube be less than one quarter of the gap. Because of the tight space in the apparatus, we were unable to meet this condition. The diameter of the pitot tube is $0.3cm$ and is roughly equal to clearance of the leakage path and the width of the inlet guide vanes. The tubes are connected to the set of water manometer mentioned earlier for stagnation pressure readings. Existing pressure taps next to the pitot tubes were used for static pressure measurements. The difference between the readings would be the velocity head of the flow in the direction facing the pitot tube.

The pitot tubes were held in place such that their orientations are fixed and can only be changed during the installation, not during the experiments. Most of the tests were done to measure only the swirl velocity, thus the pitot tubes were set tangent to the circumference. Changing their orientation to face the flow directly did not change the measurements, as the difference were within the error limits.

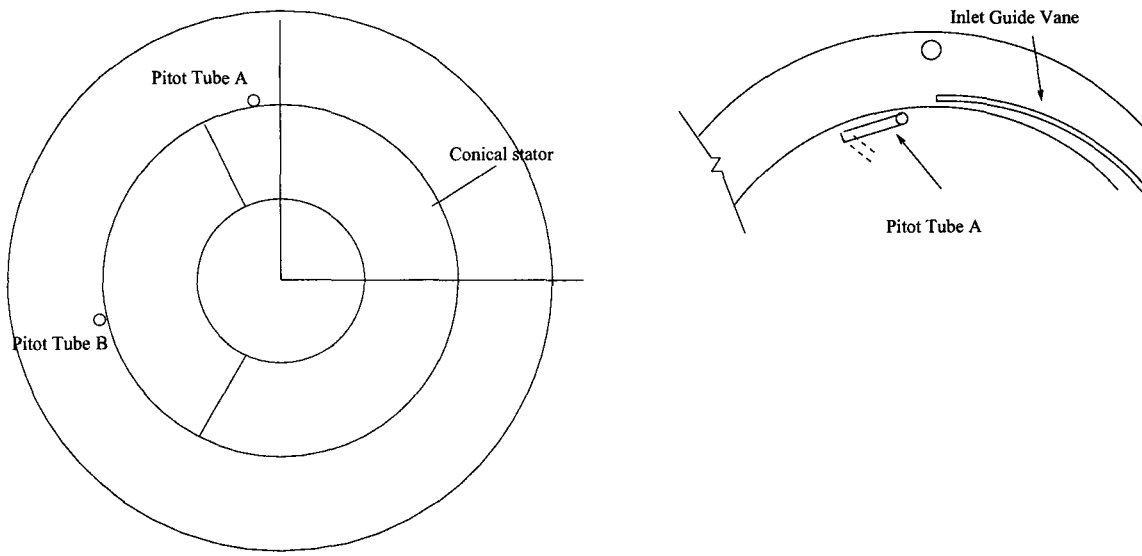

Figure 2.7: Pitot tube setup

Because of the large diameter of the pitot tubes compared to the gap width, the measured velocities are likely to be some type of averaged value for the velocity in the circumferential direction near the inlet to the leakage path. The results for the measurements of the swirl velocities will be presented in section 3.5.

2.6 Experimental Error

Errors in the measurements of the unsteady rotordynamic forces could arise from several sources. Uy (1998) placed Bentley displacement transducers during a typical experiment to measure the errors in eccentricity as well as to verify the rotational and whirl frequencies. The uncertainty in eccentricity was found to be less than 5%.

Another source of error could arise in the force measurements due to temperature drift in the strain gauges in the force balance. Uy reported that the standard deviation for various tests was under 5% for all rotordynamic coefficients with the exception of direct stiffness, which had an 8% deviation.

Water manometers were used for measuring static pressure in the leakage path at the stator surface. The uncertainty in pressure was found to be about $0.3cm$ of water; while the uncertainty for the stagnation pressure of the pitot tube measurements was

roughly $1.0cm$ of water. This is less than 5% for all of the pressure data presented in the thesis as well as the velocity measurements.

Chapter 3 Experimental Results

3.1 Introduction

A number of effects of the leakage path have been experimentally studied previously. The reader may refer to work of Guinzburg (1993), Sivo (1995), and Uy (1998) for details of tests conducted at Caltech. Comparing experimental results from using no inlet swirl devices and using the inlet swirl vanes to provide inlet swirl velocities which were as much as twice the tip velocity, Guinzburg's test showed that inlet swirl increased the the normal and tangential rotordynamic forces though nowhere near as much as those predicted by the Childs' perturbation solution to the bulk flow equations. Further tests conducted by Uy for different inlet swirl rates showed that for non-zero inlet swirl, the inlet swirl had no effect on the rotordynamic forces. This chapter presents data that disputes this claim. The pressure distributions for flows with various inlet swirl vanes installed showed no variation for the different inlet swirl devices, which could only be explained by assuming the same inlet swirl velocity existed for almost all flows. This motivated the construction of pitot tubes to measure the flow velocities at inlet to the leakage path. And those experiments confirmed the suspicion that the inlet swirl vanes did not work as Guinzburg and Uy assumed.

3.2 Curve Fitting of Forces

Rotordynamic force coefficients provide a convenient way to compactly present the rotordynamic forces and thus ease comparison. As discussed in the introduction, the normal and tangential forces are fitted, respectively, to second order and first order polynomials of the whirl frequency ratio. The validity of such curve fits is a subject of concern. Figure 3.2 shows a typical example. While the fit looks decent using this

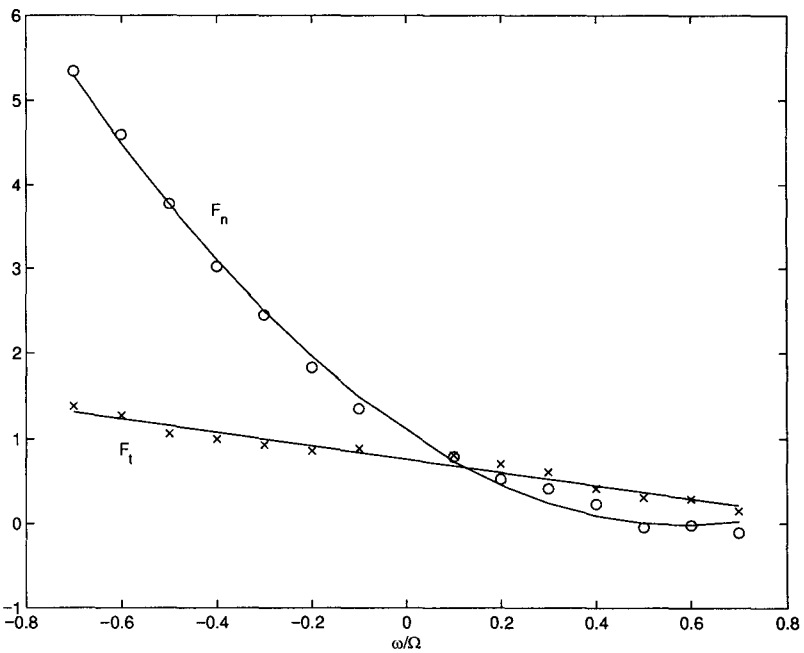

Figure 3.1: Curve fit of the rotordynamic forces

scale, it is a bit deceiving. Table 3.1 shows the difference between using all whirl frequency ratios and only the positive whirl frequency ratios for the curve fit. The discrepancy can be significant, especially for the added mass term. The coefficients for the tangential forces differ by some twenty percent.

	M	c	K	C	k
positive and negative whirls	3.22	3.76	-1.08	0.78	-0.76
positive whirls only	1.64	2.83	-1.06	1.11	-0.91

Table 3.1: curve fitting of forces using sets of different whirl frequencies

While the rotordynamic coefficients obviously do not capture all the information of the rotordynamic forces, almost all current rotordynamic analyses are done using only coefficients. This leaves researchers to always report the coefficients, no matter their inadequacies.

3.3 Effect of Anti-swirl Devices

With a rotating impeller, fluid swirl is obviously generated in the leakage path, and the question arises as to how reducing this swirl will affect rotordynamic forces. Therefore, the effects of anti-swirl ribs and grooves in the leakage path were investigated. Work by Sivo (1995) identified some benefits to having anti-swirl ribs in the leakage path, but only for very small flow coefficients.

Figure 3.2 shows the rotordynamic force coefficients as a function of the flow coefficient for the conical impeller and shroud. The tests were conducted with a 2 degree inlet swirl vane and compare the effects of anti-swirl ribs and grooves.

The direct stiffness K and the cross-coupled damping c are largest for tests with no anti-swirl devices. The two coefficients improve stability-wise with grooves and even with anti-swirl ribs. The added mass remains about the same for all three cases.

The direct damping of the tangential forces is the same magnitude for the three cases, while the cross-coupled stiffness exhibits different trends. It decreases with flow coefficient with no swirl reduction devices, and increases in the presence of anti-swirl ribs. With grooves, the cross-coupled stiffness first increases and then decreases with flow coefficient. This leads to improvements in the whirl ratio for anti-swirl devices at low flow coefficients, but to a detrimental effect at higher flow rates. The whirl ratio for the case with anti-swirl ribs is increasing with flow coefficient, in marked contrast to the decreasing trend when no anti-swirl devices are present.

Thus it seems that anti-swirl devices provide some benefit in reducing the destabilizing region in the tangential forces only for very small flow rates. They do, however, contribute to an increase in direct stiffness, helping in the stability of normal forces.

3.4 Meridional Pressure Distribution

The numerical predictions of the rotordynamic force integrate the pressure distributions within the leakage path to find the total force acting on the impeller. Therefore experimental data on the pressure distribution is useful for comparison with the nu-

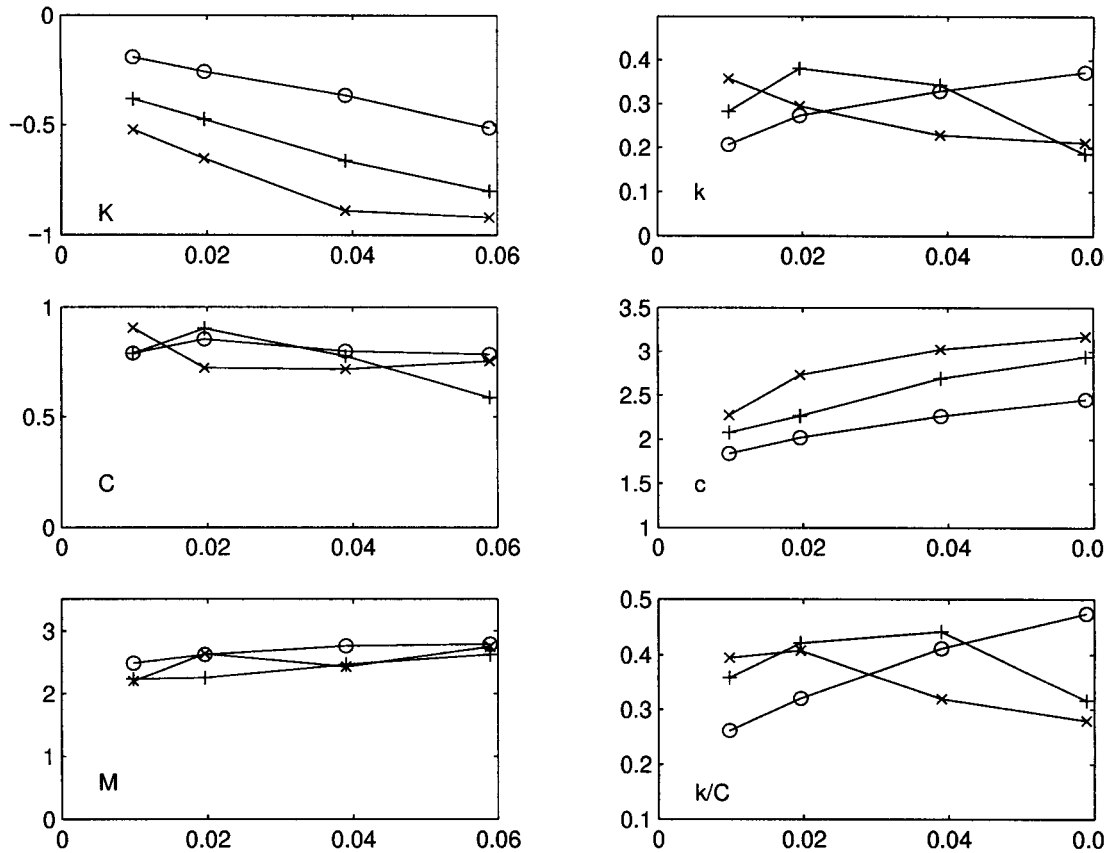

Figure 3.2: Rotordynamic coefficients plotted against flow coefficient for experiments with inlet swirl. No anti-swirl devices (×), 4 full length anti-swirl ribs (o), 4 full length anti-swirl grooves (+)

merical results and could aid in matching coefficients in turbulence models. Experiments were conducted to measure the pressure distributions along the leakage path of the conical impeller. The test apparatus included swirl vanes attached to stator to provide inlet swirl (figure 2.3). A leakage path with a clearance of 0.28 cm and an exit seal clearance of 0.05 cm was chosen for these experiments. In the setup there is an eccentricity between the rotor and the stator. Figure 3.3 shows the pressure distribution curves at different circumferential locations, from the meridian with the smallest clearance to the meridian with the largest clearance and the two 90^o locations in between.

The pressure data presented has been non-dimensionalized by the fluid density

times the square of the tip velocity, ΩR_2 (corresponding to velocity on the discharge side of the pump). It is presented as the difference between the pressure at each location and the pressure at inlet to the leakage path. The presence of the swirl vanes causes a large pressure drop from the upstream gauge pressure to the inlet pressure that is difficult to quantify. Thus the difference between the inlet pressure and the upstream pressure varies somewhat unpredictably from one experiment to the next. Hence the choice of the inlet pressure as the reference in figure 3.3.

From figure 3.4, it is seen that the pressure profiles do not differ much for different flow coefficients and are essentially identical for the first several points in the leakage path. Note that the pressures in figure 3.4 are from a circumferential location where the clearance is equal to the average clearance. Figure 3.5 shows that changes in the rotational speed of the impeller also do not affect the dimensionless pressure profile. Comparisons with calculated pressure profiles will be presented in section 5.2. The comparisons demonstrated that the best explanation for the lack of dependence of experimental pressure profiles on the flow coefficient is that the different leakage flows had the same inlet swirl, something that is contrary to the original intent of the inlet swirl vane design. This motivated the measurements of the inlet swirl for various flows with several different inlet swirl vanes. Details of these experiments are presented in the next section.

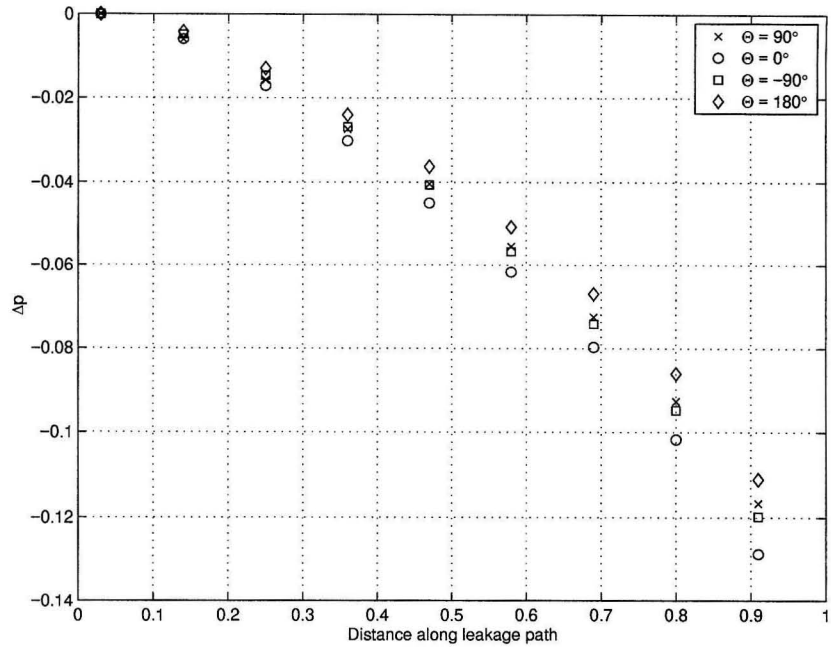

Figure 3.3: Non-dimensionalized pressure distribution along the leakage path (on the horizontal scale 0 is the leakage path inlet and 1 is the exit) for different circumferential locations, 90^o from narrowest clearance ($\times$), $180^o(\diamond)$, $-90^o(\square)$, $0^o(\circ)$

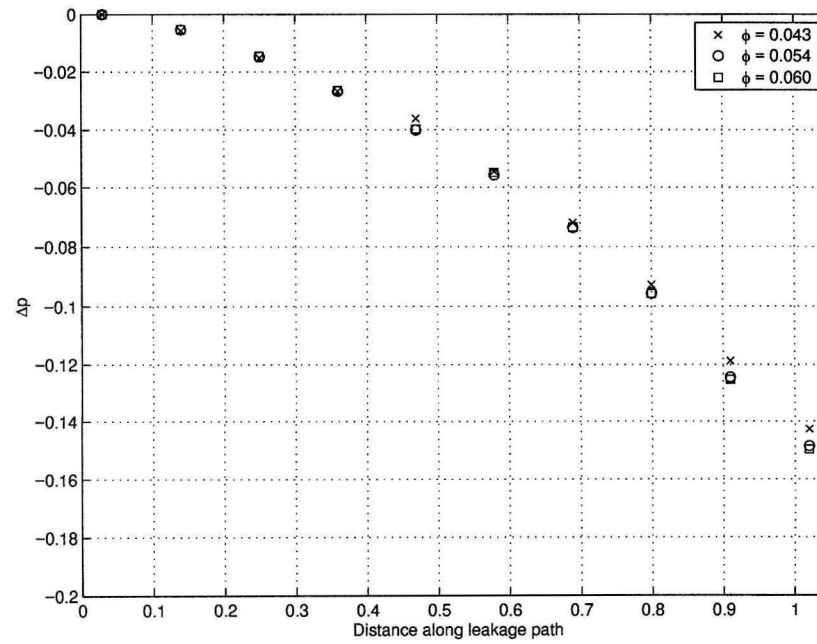

Figure 3.4: Non-dimensionalized pressure profile for different flow coefficients, $0.043(\times)$, $0.054(\circ)$, $0.060(\square)$, zeroed about the first data point

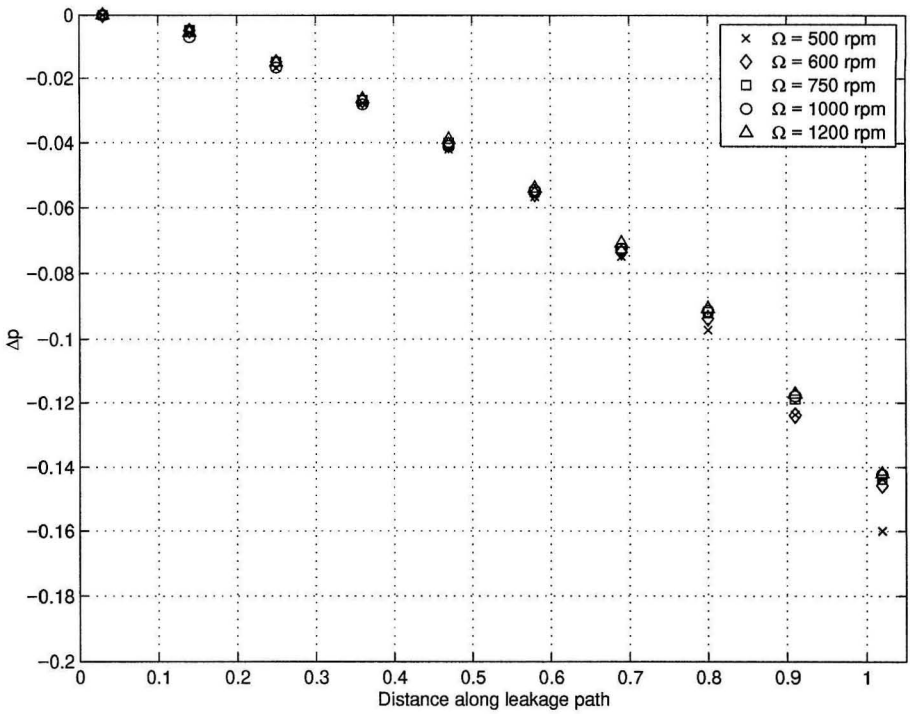

Figure 3.5: Non-dimensionalized pressure profile for different impeller rotation speeds when $\phi = 0.043$, 500 rpm ($\times$), 600 rpm($\diamond$), 750($\square$),1000 rpm($\circ$), 1200($\wedge$)

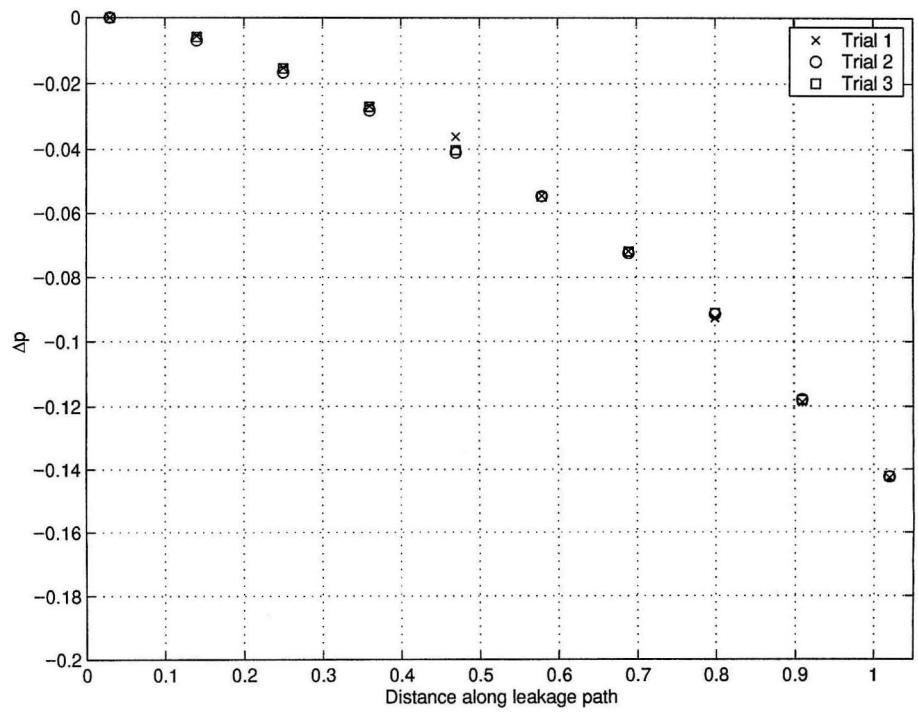

Figure 3.6: Repeated non-dimensional pressure profile for trials 1, 2, and 3

3.5 Inlet Swirl

Analysis of the pressure profiles necessitated the measurement of the swirl at inlet to the leakage path. The inlet swirl was measured by inserting a pitot tube in the gap between the exit of the inlet swirl vane and the entrance to the leakage path as described in section 2.5.1. Measurements were made over a wide range of flow coefficients and with different inlet swirl vanes, an inlet swirl vane with a 6 degree turning angle, another with a 2 degree turning angle, as well as an inlet swirl device with a set of 24 radial vanes designed to eliminate inlet swirl.

As figure 3.7 shows, with the exception of the radial vanes, the inlet swirl ratios are within a narrow range between 0.24 to 0.28, with an uncertainty of about 0.02. The data is from the pitot tube B; data from pitot tube A gave slightly larger results, by approximately 0.03. As equation 2.6 shows, the theoretical, or the intended, inlet swirl ratio, Λ, for these flows vary from 0 to 1.8. It therefore seems that the inlet swirl vanes are not creating the expected swirl at inlet to the leakage flow. Some possible causes are discussed in the next section.

The radial vanes, however, do seem to affect the flow at higher flow rates. For low flow rates, the inlet swirl ratio is around 0.18, slightly lower than flows with inlet swirl vanes. Once the flow coefficients are greater than 0.03, the inlet swirl ratio drops to around 0.05, decreasing further to zero after flow coefficient becomes larger than 0.05.

The experimental inlet swirl ratios seem to be consistent with the rotordynamic force measurements as seen in figure 3.8 (Uy 1997). For the various flows with inlet swirl, there is no effect of the inlet swirl ratio. That can be easily explained by the observation that the measured inlet swirl ratios are nearly constant for all these flows. As for the flows with radial vanes, at low flow coefficients the inlet swirl ratio is quite close to those with inlet swirl, and the rotordynamic forces reflect this. The forces are indeed fairly similar, with the normal forces being nearly identical. Above a flow coefficient of 0.03, the forces start to diverge, which is consistent with measurement of much lower inlet swirl ratios.

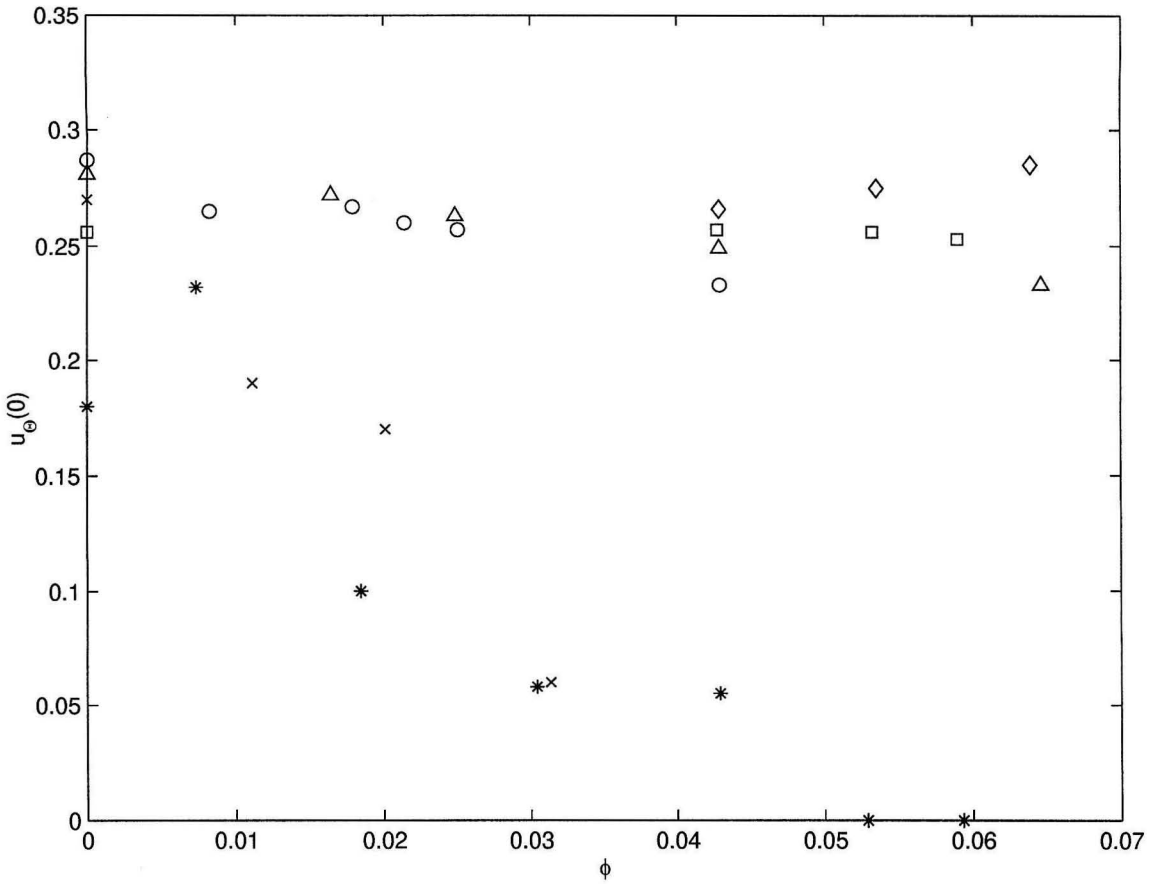

Figure 3.7: Experimental inlet swirl ratio versus flow coefficient ϕ, with 6 degree inlet swirl vane at 500 rpm($\diamond$), 1000 rpm($\square$), with 2 degree swirl vane at 500 rpm($\triangle$), 1000 rpm($\circ$), and with radial vane at 1400 rpm($\times$), 1000 rpm($*$)

The rotordynamic forces were measured for a contoured geometry. However the entrance regions are very similar for the contoured and the conical impellers and there is no reason to expect the inlet swirl velocities to the leakage paths would be different.

It therefore appears that the various inlet swirl vanes with different turning angles are not guiding the flow as intended, and the resulting leakage flows all have the same inlet swirl ratios. The exception occurs with the radial vanes, which seem to result in low swirl ratios at higher flow rates.

The pressure differences between the reservoir upstream of the vanes and the inlet to the leakage path also reflect this new interpretation. Figure 3.5 shows the pressure drop of the fluid as it passes through the inlet guide vane structure. The pressure drops for flows with the radial vanes are significantly lower than those for flows with

inlet guide vanes. Thus figure 3.5 further strengthens the evidence that the radial vanes do something significantly different than the inlet swirl vanes.

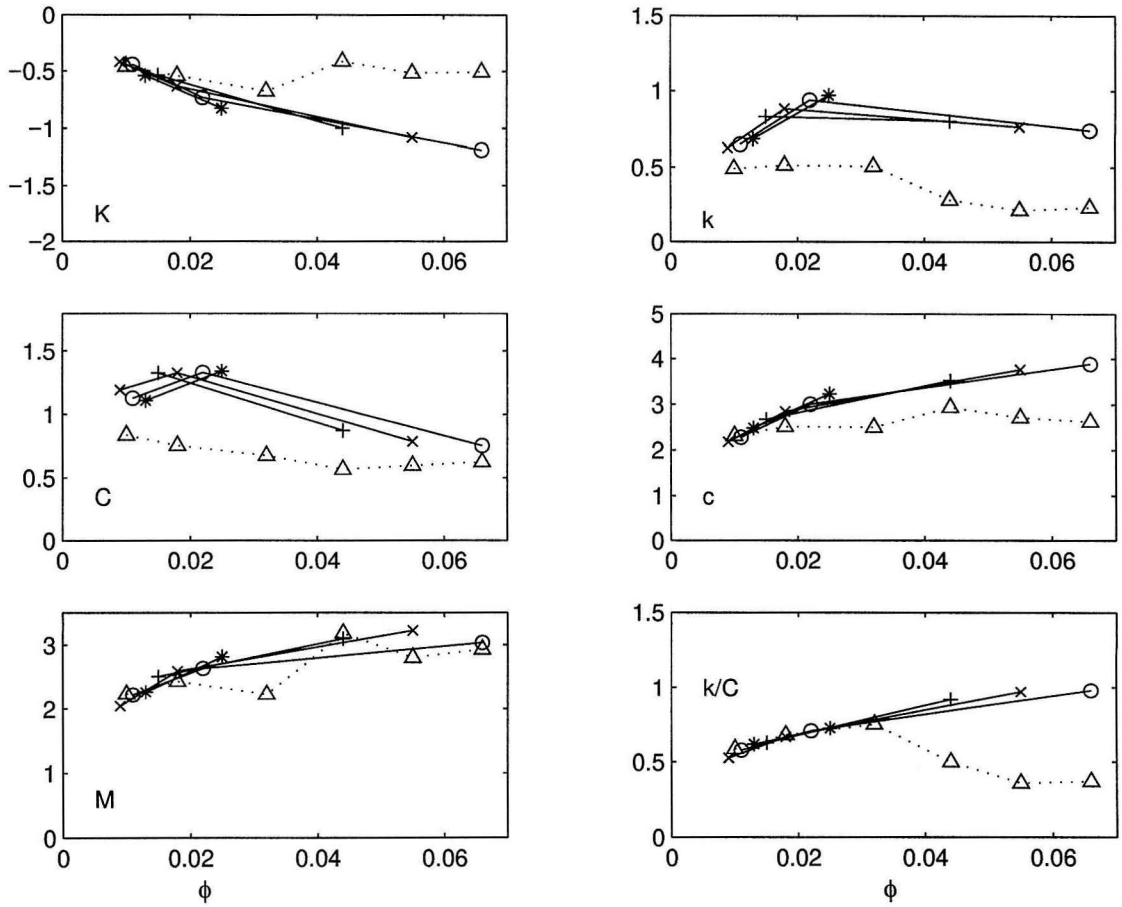

Figure 3.8: Experimental rotordynamic coefficients plotted against flow coefficient ϕ for tests with inlet swirl, $\Lambda = 0.0$ ($\triangle$), 0.4 (+), 0.5 ($\times$), 0.6 ($\circ$), and 0.7 ($*$) (Uy, 1997)

3.6 Discussion

The experimental data from the current research shows that the inlet swirl vanes are not providing the designed inlet swirl to the leakage path. For ranges of the experimental parameters used during previous rotordynamic force measurements, the measured inlet swirl velocity to the leakage path is nearly constant, between 0.24 to 0.28 of the tip velocity of the impeller. It is postulated that because of the small

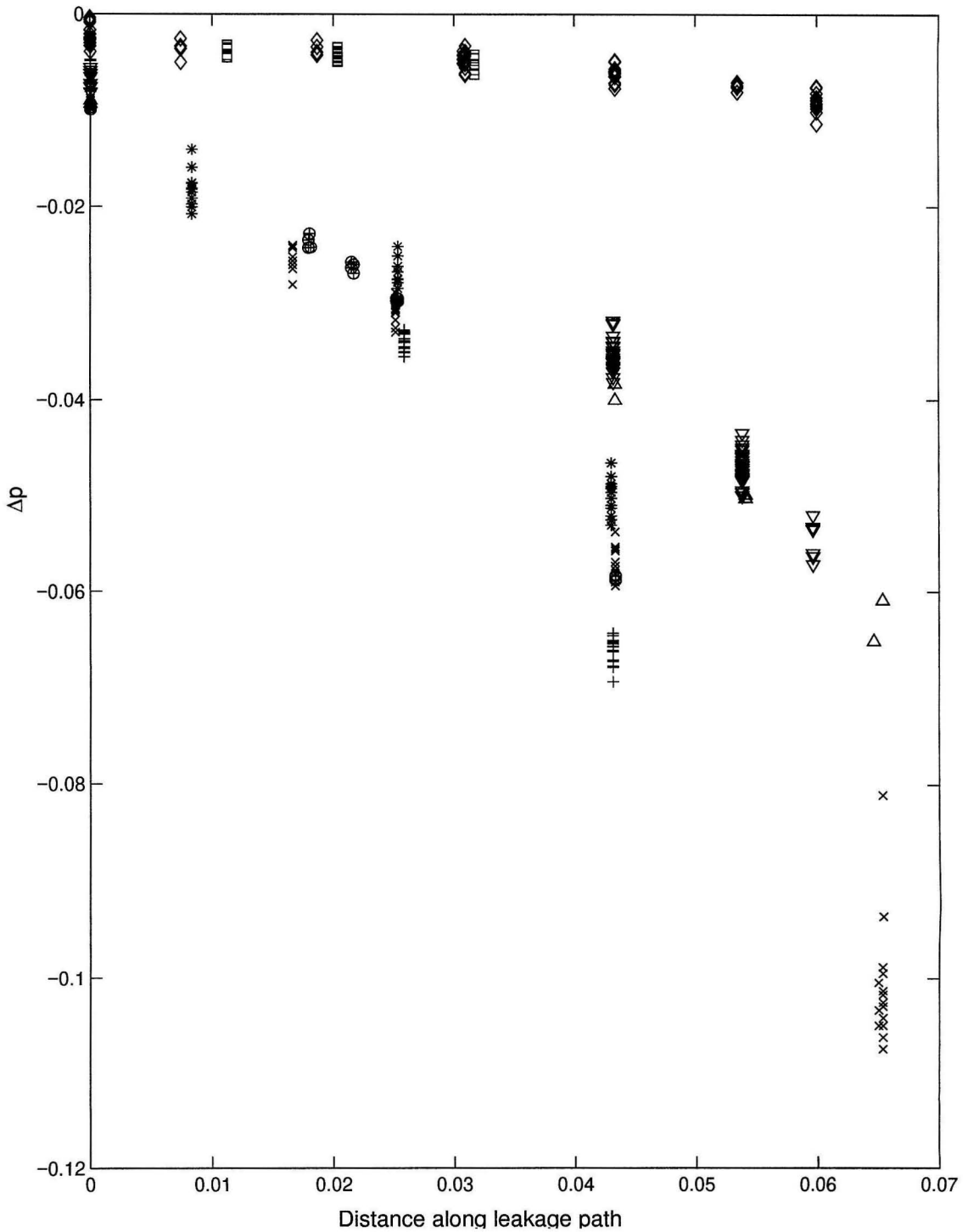

Figure 3.9: Experimental pressure drop across the inlet guide vane structure plotted versus flow coefficient, with 2 degree inlet swirl vane at 500 rpm ($\times$), 1000 rpm ($\circ$ for trial 1, $*$ for trial 2, $+$ for trial 3), 6 degree inlet vane at 500 rpm ($\triangle$), 1000 rpm (∇), and radial vanes at 1400 rpm ($\square$), 1000 rpm ($\diamond$)

clearance in the guide vane structure, viscous forces dominate thus negating the guiding effects of the swirl vanes. The viscous forces will act to slow down the fluid flow in the circumferential direction and push the fluid inward in a more radial manner at the exit from the guide vanes. Another possible reason may be the gap that exists between end of the inlet guide vanes and the beginning of the leakage path. The gap is connected to a fluid-filled chamber; mixing may occur in this region and thus reduce the effects of the inlet guide vanes.

The radial vanes, on the other hand, do prevent inlet swirl at higher flow rates. For zero throughflow or very low flow rates, the inlet swirl velocities are similar to those with no inlet guide vane structure. One may speculate that at low flows, the space between the radial vanes are too wide to force the flow to go completely radially. The measured rotordynamic forces are consistent with these experimental measurements of inlet swirl velocities to the leakage path.

Chapter 4 Theory of Bulk Flow Equations

The bulk-flow model developed by Childs (1989) is widely used in rotordynamic analysis for relatively simple computational domains, and is particularly valuable in its simplicity and ease of computations. Essentially the fluid flow is modelled as uniform across the gap thereby reducing the computational domain to two dimensions. In addition shear stresses at fluid-fluid interfaces are ignored and only the shear stresses at solid-fluid contacts are considered. The resulting equations are the Euler's equations in an annular coordinate system plus four shear stresses terms, two of them from rotor-fluid contact, two from stator-fluid interface. Based on Hirs (1973) lubrication equations, the bulk flow model uses simple correlations for shear stresses based on gap-averaged velocities. As presented by Childs, the model assumes that the three-dimensional, unsteady, turbulent flow in an annular region can be accurately approximated by reducing the dimension of the flow from three to two by using a simple correlation between the shear stresses and the gap averaged velocities and by treating the rotordynamic flow as a linear perturbation flow on the mean flow. Each assumption should be carefully examined when applying the model to a more complex computational domain such as a centrifugal pump leakage path.

The assumption that the dimensions of the flow can be reduced from three to two is common and leads to the Reynolds lubrication equations. This implies that the velocity profiles within the annular region are self-similar and, therefore, the equations of the flow can be averaged over the gap without excessive error. Limitations may occur under certain conditions noted in experiments in which flow reversals and recirculation zones occur in the leakage path. For example, changes in flow direction could lead to frictional stresses acting in direction opposite of those predicted by the gap averaged velocity. Certain 3-D computational analyses (Baskharone and Hensel,

1993) have observed these flow reversals. With recirculation regions occurring in different parts of the gap and changing with different flow rates and impeller speeds, a serious limitation may be placed on the assumption of a two-dimensional domain.

The Reynolds number for most leakage flows is very high (of order 10^4 based on the tip speed of the impeller and the gap clearance for experiments at Caltech), and this mean the bulk flow model requires expressions relating the turbulent shear stresses to the gap-averaged velocities. The turbulent shear stress relationships used are correlations for steady turbulent flows based, primarily, on experimental observations of steady flows. In contrast, the rotordynamic flows of concern here are fundamentally unsteady. The problem is that very little is known about turbulent flows which are unsteady in the sense that the flow is being externally excited in an unsteady way. Therefore, correlations such as those used here are used only because there are no alternatives. It must be recognized that the unsteady flows of the present context may lead to substantial deviations from these correlations. At present, this issue can only be resolved by careful comparison of the experimental and model results.

One peculiar aspect of the Childs' perturbation model is the prediction of resonances in the rotordynamic forces for particular subsynchronous whirl frequencies. The work of Guinzburg showed no such resonances in the experimental data and demonstrated that the resonances mostly arise from reducing the problem to where the flow variables are sinusoidal in the circumferential direction and harmonic in time. To eliminate this problem and to allow for circumferentially varying geometries, a new method of solving the bulk flow equations without resorting to linearization in eccentricity or assuming harmonic forms is proposed. By changing the coordinate system to one rotating with the whirl and assuming the flow in the rotating coordinate system is independent of time, the resulting equation in two dimensions can be solved. In this new formulation, evolutionary equations for a vorticity and total pressure will shed some insight into the physical properties of these rotordynamic flows.

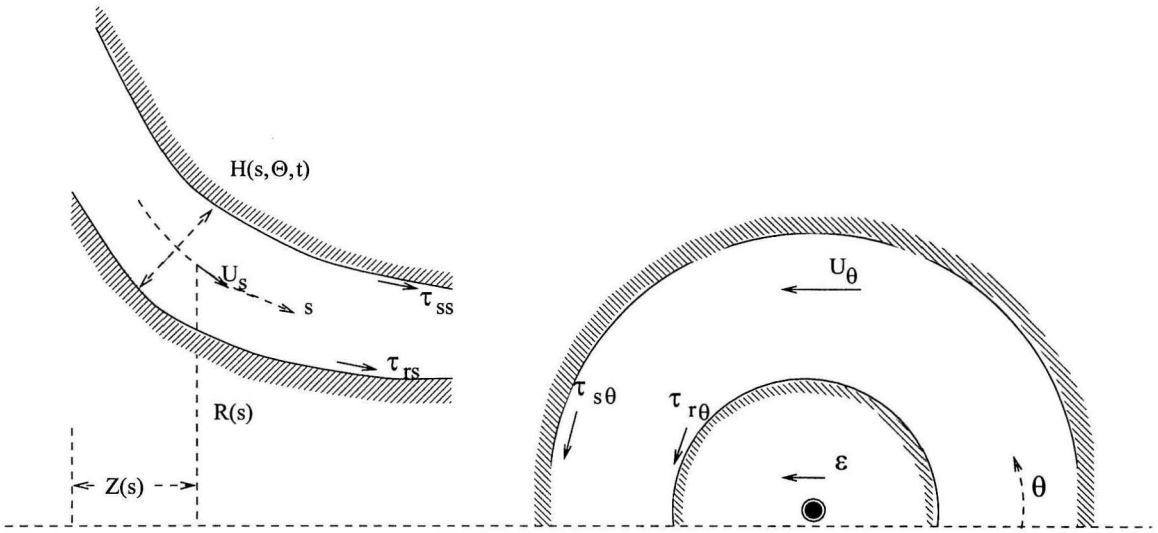

Figure 4.1: Geometry of fluid filled annulus between a rotor and a stator for turbulent lubrication analysis

4.1 The Bulk Flow Model Equations

The geometry is sketched in figure 4.1, and is described by the meridian of the gap as given by $Z(s)$ and $R(s)$, $0 < s < L$, where the coordinate, s, is measured along the meridian.

The equations governing the bulk flow are averaged over the gap. This leads to a continuity equation of the form

$$\frac{\partial H}{\partial t} + \frac{\partial}{\partial s}\left(H u_s\right) + \frac{1}{R}\,\frac{\partial}{\partial \Theta}\left(H u_\Theta\right) + \frac{H u_s}{R}\,\frac{dR}{ds} = 0 \tag{4.1}$$

where u_s and u_Θ are gap-averaged velocities in the s and Θ directions. The meridional and circumferential momentum equations are

$$-\frac{1}{\rho}\,\frac{\partial p}{\partial s} = \frac{\tau_{Ss}}{\rho H} + \frac{\tau_{Rs}}{\rho H} - \frac{u_\Theta^2}{R}\,\frac{dR}{ds} + \frac{\partial u_s}{\partial t} + \frac{u_\Theta}{R}\,\frac{\partial u_s}{\partial \Theta} + u_s\frac{\partial u_s}{\partial s} \tag{4.2}$$

$$-\frac{1}{\rho R}\,\frac{\partial p}{\partial \Theta} = \frac{\tau_{S\Theta}}{\rho H} + \frac{\tau_{R\Theta}}{\rho H} + \frac{\partial u_\Theta}{\partial t} + \frac{u_\Theta}{R}\,\frac{\partial u_\Theta}{\partial \Theta} + u_s\frac{\partial u_\Theta}{\partial s} + \frac{u_\Theta u_s}{R}\,\frac{\partial R}{\partial s} \tag{4.3}$$

We note that the equations not only include the viscous terms commonly included in lubrication analyses (see for example Pinkus and Sternlicht 1961) but also the inertial

terms (see Fritz 1970) which are necessary for the evaluation of the rotordynamic coefficients.

To determine the turbulent shear stresses, Childs employed the approach used by Hirs (1973). The turbulent shear stresses, τ_{Ss} and $\tau_{S\Theta}$, applied to the stator by the fluid in the s and Θ directions are given by

$$\frac{\tau_{Ss}}{\rho u_s} = \frac{\tau_{S\Theta}}{\rho u_\Theta} = \frac{n_s}{2}\left[u_s^2 + u_\Theta^2\right]^{\frac{m_s+1}{2}} (H/\nu)^{m_s} \tag{4.4}$$

and the stresses, τ_{Rs} and $\tau_{R\Theta}$, applied to the rotor by the fluid in the same directions:

$$\frac{\tau_{Rs}}{\rho u_s} = \frac{\tau_{R\Theta}}{\rho(u_\Theta - \Omega R)} = \frac{n_r}{2}\left[u_s^2 + (u_\Theta - \Omega R)^2\right]^{\frac{m_\Theta+1}{2}} (H/\nu)^{m_\Theta} \tag{4.5}$$

where the constants n_s, n_r, m_s and m_r are chosen to fit the available data on turbulent shear stresses. Childs (1983a) uses typical values of these constants from simple pipe flow correlations:

$$n_s = n_r = 0.079 \quad ; \quad m_s = m_r = -0.25 \tag{4.6}$$

We will focus on steady whirl with a constant eccentricity, ϵ, rotating at the whirl frequency, ω, which is superimposed on the shaft rotation with radian frequency, Ω. Consequently, the fluid flow in a frame of reference rotating at ω is steady and it is clearly appropriate to rewrite the equations and to solve them in this rotating frame. Defining, therefore, a new angular variable, θ, and a new angular velocity, u_θ, in this rotating frame such that

$$\theta = \Theta - \omega t \quad ; \quad u_\theta = u_\Theta - \omega R \tag{4.7}$$

it follows that the continuity equation can be written as

$$\frac{\partial}{\partial \theta}\{H u_\theta\} + \frac{\partial}{\partial s}\{R H u_s\} = 0 \tag{4.8}$$

and this is most easily satisfied by defining a stream function, $\psi(s,\theta)$, such that

$$u_s = \frac{1}{RH}\frac{\partial\psi}{\partial\theta} \quad ; \quad u_\theta = -\frac{1}{H}\frac{\partial\psi}{\partial s} \tag{4.9}$$

It follows that the total volume flow rate, Q, at any meridional location, s, is given by

$$Q = \psi(s,2\pi) - \psi(s,0) \tag{4.10}$$

and this provides a periodic boundary condition on ψ in the θ direction.

In the rotating frame of reference, the equations of motion are usefully written using the total pressure, P, instead of the pressure, p, where

$$\frac{P}{\rho} = \frac{p}{\rho} + \frac{1}{2}(u_s^2 + u_\theta^2 - R^2\omega^2) \tag{4.11}$$

and the equations of motion, equations (4.2) and (4.3), then become

$$\frac{\partial}{\partial s}\left(\frac{P}{\rho}\right) = -Hu_\theta\Gamma - u_s(g_S + g_R) \tag{4.12}$$

$$\frac{1}{R}\frac{\partial}{\partial\theta}\left(\frac{P}{\rho}\right) = Hu_s\Gamma - (u_\theta + \omega R)(g_S + g_R) + \Omega R g_R \tag{4.13}$$

where the important quantity, Γ, given by

$$\Gamma = \frac{1}{H}\left[-\frac{1}{R}\frac{\partial}{\partial s}(Ru_\theta + \omega R^2) + \frac{1}{R^2}\frac{\partial}{\partial\theta}(Ru_s)\right] \tag{4.14}$$

plays a crucial role both in understanding the fluid mechanics of these flows and in the solution methodology. Also, in equations (4.12) and (4.13), the functions, g_S and g_R, are the shear stress terms for the stator and rotor respectively and are given by

$$g_S = \frac{n_s}{2H}\left(\frac{H}{\nu}\right)^{m_s}\left\{u_s^2 + (u_\theta + \omega R)^2\right\}^{\frac{m_s+1}{2}} \tag{4.15}$$

$$g_R = \frac{n_r}{2H}\left(\frac{H}{\nu}\right)^{m_r}\left\{u_s^2 + (u_\theta + \omega R - \Omega R)^2\right\}^{\frac{m_r+1}{2}} \tag{4.16}$$

The quantity, Γ, is the effective vorticity for this flow and a fundamental property can be discerned by eliminating P from equations (4.12) and (4.13) to obtain the basic convection equation for Γ:

$$u_s \frac{\partial \Gamma}{\partial s} + u_\theta \frac{1}{R} \frac{\partial \Gamma}{\partial \theta} = \frac{1}{RH} \left[\frac{\partial}{\partial s} \left\{ R(u_\theta + \omega R)(g_S + g_R) - \Omega R^2 g_R \right\} - \frac{\partial}{\partial \theta} \left\{ u_s (g_S + g_R) \right\} \right] \tag{4.17}$$

which demonstrates that, in the absence of viscous effects ($g_S = g_R = 0$), the vorticity is invariant along any streamline. Conversely, the shear stresses are alone responsible for any change in Γ along a streamline. If ξ is a coordinate measured along a streamline, then equation (4.17) clearly implies that

$$\frac{\partial \Gamma}{\partial \xi} = \frac{1}{RH(u_s^2 + u_\theta^2)^{\frac{1}{2}}} \left[\frac{\partial}{\partial s} \left\{ R(u_\theta + \omega R)(g_S + g_R) - \Omega R^2 g_R \right\} - \frac{\partial}{\partial \theta} \left\{ u_s (g_S + g_R) \right\} \right] \tag{4.18}$$

Furthermore, when written in this way, the governing equations clearly indicate a physically reasonable approach to their numerical solution by iterative means.

4.2 The Limit of Zero Eccentricity

For clarification we examine the special case of zero eccentricity. The purpose is twofold. First to resolve an apparent inconsistency which could be perceived in the above system of equations and, second, to develop a zero eccentricity model which will be used to derive the meridional pressure distributions for comparison with experimentally measured pressure distributions.

Since the flow becomes axisymmetric at zero eccentricity, it must follow that $\frac{\partial}{\partial \theta} = 0$. Using equation (4.13) and $\frac{\partial}{\partial \theta} \left(\frac{P}{\rho} \right) = 0$, the equation for Γ then becomes

$$H\Gamma = \frac{1}{u_s} \left[(u_\theta + \omega R)(g_s + g_r) - \Omega R g_r \right] \tag{4.19}$$

or, in terms of the stresses,

$$H u_s \Gamma = \frac{\tau_{s\Theta}}{\rho H} + \frac{\tau_{r\Theta}}{\rho H} \tag{4.20}$$

From equation (4.14), the definition of Γ, it follows that

$$H\Gamma = -\frac{1}{R}\frac{\partial}{\partial s}\left(Ru_\theta + \omega R^2\right) = -\frac{1}{R}\frac{\partial}{\partial s}\left(Ru_\Theta\right) \tag{4.21}$$

and combining this with equation (4.19) gives a first order differential equation for u_Θ:

$$\frac{\partial}{\partial s}\left(Ru_\Theta\right) = -\frac{R}{u_s}\left[u_\Theta\left(g_s + g_r\right) - \Omega R g_r\right] \tag{4.22}$$

Notice that all the terms in this equation are independent of the whirl frequency, ω. This means that given the inlet conditions in absolute coordinates, u_Θ will be the same for any whirl frequency. This result, of course, is expected since, with no eccentricity, the whirling motion is non-existent.

Since there is no eccentricity, the pressure drop should also be independent of whirl. However, from equation (4.12)

$$\frac{\partial}{\partial s}\left(\frac{P}{\rho}\right) = -Hu_\theta\Gamma - \frac{\tau_{Ss}}{\rho H} - \frac{\tau_{Rs}}{\rho H} \tag{4.23}$$

$$= -\frac{u_\theta}{u_s}\left[\frac{\tau_{S\Theta}}{\rho H} + \frac{\tau_{S\Theta}}{\rho H}\right] - \frac{\tau_{Ss}}{\rho H} - \frac{\tau_{Rs}}{\rho H} \tag{4.24}$$

$$= -\frac{1}{\rho H u_s}\left[u_\theta\left(\tau_{S\Theta} + \tau_{R\Theta}\right) + u_s\left(\tau_{Ss} + \tau_{Rs}\right)\right] \tag{4.25}$$

For different whirl frequencies, the stresses are the same since the flow field remains unchanged. A superficial inspection of equation (4.25) suggests an inconsistency arising from the term u_θ. Since the relative velocity $u_\theta = u_\Theta - \omega R$, where u_Θ is the flow in absolute coordinates, the term ωR which thus appears in equation (4.25) suggests that the pressure drop will differ for different whirl frequencies. This inconsistency is resolved as follows.

The total pressure in absolute coordinates, $\tilde{P}$, is defined as

$$\frac{\tilde{P}}{\rho} = \frac{p}{\rho} + \frac{1}{2}\left(u_s^2 + u_\Theta^2\right) \tag{4.26}$$

or rewritten in terms of u_θ,

$$\frac{\tilde{P}}{\rho} = \frac{p}{\rho} + \frac{1}{2}\left(u_s^2 + u_\theta^2 + 2\omega R u_\theta + \omega^2 R^2\right) \tag{4.27}$$

Subtracting equation (4.11) from the above equation, we see that the relationship between the two total heads, P in the rotating coordinate system and $\tilde{P}$ in the absolute frame, is

$$\frac{\tilde{P}}{\rho} - \frac{P}{\rho} = \omega R u_\theta + \omega^2 R^2 \tag{4.28}$$

$$= \omega R u_\Theta \tag{4.29}$$

From equations (4.2) and (4.3), we can derive an equation for $\frac{\partial}{\partial s}\left(\frac{\tilde{P}}{\rho}\right)$ similar to that of equation (4.25),

$$\frac{\partial}{\partial s}\left(\frac{\tilde{P}}{\rho}\right) = -\frac{1}{\rho H u_s}\left[u_\Theta\left(\tau_{S\Theta} + \tau_{R\Theta}\right) + u_s\left(\tau_{Ss} + \tau_{Rs}\right)\right] \tag{4.30}$$

Using the above equation and equations (4.29), (4.22), we can derive an expression for $\frac{\partial}{\partial s}\left(\frac{P}{\rho}\right)$ by a different route and obtain equation (4.25). This proves that the equation (4.25) is correct, and that the pressure drop, as defined in *rotating* coordinates, is in fact a function of the whirl frequency ratio. Thus, in presenting pressure distribution, we must be careful to compare experimental measurements with the calculation of the total pressure in the absolute coordinate system.

4.3 Numerical Method of Solution

It follows from section 4.1 that one method for the solution of the equations for a rotordynamic flow proceeds as follows:

(1) First, for given or guessed values of the vorticity, $\Gamma(s,\theta)$, we solve the Poisson-like equation (4.14) for the stream function, $\psi(s,\theta)$:

$$\frac{\partial}{\partial s}\left\{\frac{R}{H}\frac{\partial \psi}{\partial s} - \omega R^2\right\} + \frac{1}{R}\frac{\partial}{\partial \theta}\left\{\frac{1}{H}\frac{\partial \psi}{\partial \theta}\right\} = RH\Gamma \tag{4.31}$$

and thereby obtain new values for $\psi(s,\theta)$, $u_s(s,\theta)$ and $u_\theta(s,\theta)$. For this purpose we deploy boundary conditions on ψ as follows:

(i) Along $s = 0$, we specify an inlet swirl velocity, $u_\theta(0,\theta)$, which, in order to satisfy conservation of angular momentum, should normally be put equal to the swirl velocity in the reservoir upstream of the inlet. However, usually an initial u_θ is put in even for cases of no inlet swirl.

(ii) An appropriate boundary condition at discharge, $s = S$, would be that the pressure in the flow exiting the annulus should be uniform for all θ or

$$\left(\frac{\partial p}{\partial \theta}\right)_{s=S} = 0 \tag{4.32}$$

This will be discussed in more detail in the next section.

(iii) The periodic conditions on boundaries at $\theta = 0$ and $\theta = 2\pi$ such that

$$\psi(s,2\pi) - \psi(s,0) = Q \tag{4.33}$$

(2) Second, given the new values of $\psi(s,\theta)$, $u_s(s,\theta)$ and $u_\theta(s,\theta)$, we can proceed to integrate from inlet to exit to find new values for $\Gamma(s,\theta)$ using equation (4.17). For this purpose we must evaluate the shear stress functions, g_R and g_S, in equations (4.15) and (4.16). We also need the values of Γ at the points where the streamlines enter the computational domain. Clearly this becomes more complicated when there is reverse flow either at inlet or at discharge. We delay discussion of this complication until later. If all the streamlines begin at inlet, then the boundary condition on that inlet boundary, $s = 0$, should be that the total pressure is uniform along that boundary. Assuming that the inlet flow has

not experienced significant viscous stresses, the total head is constant at inlet, and equation (4.13) provides an initial value of Γ,

$$\Gamma(0,\theta) = \frac{1}{Hu_s}[(u_\theta + \omega R)(g_S + g_R) + \Omega R g_R] \tag{4.34}$$

given the results from step 1.

We then repeat these two steps until the solution converges.

4.4 Head, Pressure and Rotordynamic Forces

Having obtained convergence, we then calculate the total pressure, P, the pressure, p, and the rotordynamic forces as follows. The total pressure is obtained in a procedure similar to that for the vorticity, Γ. From equations (4.12) and (4.13) it follows that

$$u_s \frac{\partial}{\partial s}\left(\frac{P}{\rho}\right) + \frac{u_\theta}{R}\frac{\partial}{\partial \theta}\left(\frac{P}{\rho}\right) = \left[\Omega R u_\theta g_R - \left\{u_s^2 + u_\theta(u_\theta + \omega R)\right\}(g_R + g_S)\right] \tag{4.35}$$

If one chooses to neglect entrance losses between the upstream reservoir at the inlet plane ($s = 0$), then this integration begins with a uniform value of $P(0,\theta)$ equal to the total pressure in the reservoir, P_{res}, and this can conveniently be chosen to be zero without loss of generality. On the other hand if entrance losses are to be included, then $P(0,\theta)$ can be set to a value smaller than P_{res} by an amount equal to the entrance loss at that particular θ position. Having obtained $P(s,\theta)$ throughout the flow field, the pressure, $p(s,\theta)$, follows simply from the definition (4.11).

From the case of zero eccentricity, we found that the absolute total pressure, $\tilde{P}$, should be used as P_{res}. From equation (4.29), however, we see that the difference between P and $\tilde{P}$ is uniform at inlet since $u_\theta(0,\theta)$ is prescribed to be uniform. Hence we can choose $P(0,\theta)$ to be zero when there are no inlet losses; with inlet losses we can use a fraction of u_s, namely,

$$P(0,\theta) = -k u_s^2(0,\theta) \tag{4.36}$$

where k is some constant. k is normally assumed to be 0, since the precise value has minimal contribution to the pressure distribution and the rotordynamic forces.

For the discharge boundary condition on the streamline calculations, an exit pressure loss term is added to simulate an exit seal.

$$\frac{\partial}{\partial\theta}\left(p - \zeta u_s^2(\theta)\right)_{s=S} = 0 \tag{4.37}$$

Having obtained the pressure (and the viscous shear stresses) it only remains to integrate these to obtain the normal and tangential forces acting on the rotor. With the sign convention as defined in figure 1.3, it follows that

$$F_n = \int_0^S \left\{1 - \left(\frac{dR}{ds}\right)^2\right\}^{\frac{1}{2}} \int_0^{2\pi} \left(p\cos\theta + \tau_{R\theta}\sin\theta\right) d\theta \quad ds \tag{4.38}$$

$$F_t = \int_0^S \left\{1 - \left(\frac{dR}{ds}\right)^2\right\}^{\frac{1}{2}} \int_0^{2\pi} \left(p\sin\theta - \tau_{R\theta}\cos\theta\right) d\theta \quad ds \tag{4.39}$$

In most of the results quoted in this paper, the contributions from the $\tau_{R\theta}$ parts of these integrals are very small and can usually be neglected.

4.5 Some Notes on the Computations

As outlined in section 4.3, the computational procedure is a two-step process. With an initial velocity profile, the total head, P, and Γ are integrated using a forward integration method second order accurate in both dimensions. The method then proceeds to solve the stream function to determine the velocities u_θ and u_s for the new Γ values and the new downstream pressure condition. The downstream boundary condition for the stream function solution is achieved by changing u_θ at the exit to satisfy the boundary condition. For example, if the constant pressure condition is deployed, then this is implemented by first calculating an average pressure $\bar{p}$ using

$$\bar{p} = Average(P - \frac{1}{2}\left(u_s^2 + u_\theta^2 - R^2\omega^2\right)) \tag{4.40}$$

and then adjusting the existing u_θ value using

$$(u_\theta)_j^2 = -2\bar{p} + (2P - u_s^2 + R^2\omega^2)_j \tag{4.41}$$

Some of the numerical instability experienced appears to arise from this procedure. For example, sometimes the right-hand side of equation (4.41) will become negative at some point during the iterative procedure. No matter how this is treated, the resulting u_θ at that point will be significantly differently than the rest. At times this leads to divergence as the iterative procedure is not able to filter out these inappropriate values.

To counter this, the first several iterations are done with a constant u_θ exit condition. The constant u_θ condition can be considered as a first order approximation to the constant pressure boundary condition. This makes convergence of the code much smoother, and it also negates the necessity of choosing a good initial profile.

Chapter 5 Numerical Results

The computation model was exhaustively tested on two sets of geometries for which reliable experimental data is available. One comparison was with the seal tests conducted by Marquette and Childs (1991). Seal geometry is very similar to leakage path geometry. The particular seal of Marquette and Childs had an axially uniform radius, with a length to radius ratio of 0.914 and an average clearance of 0.0029 of the radius. Rotor speed varied from 10400 rpm to 41600 rpm and pressure drops from 4 MPa to 12 MPa. The other comparison is with the conical impeller in the RTFT at Caltech. In those tests the ratio of the average clearance to inlet radius is 0.03. One difference between the two flows is the presence of the exit seal for the conical impeller tests. About half of the total pressure drop in the leakage path for the conical impeller occurs in the exit seal. Another difference is that the clearance is about an order of magnitude smaller for the seal experiments than for the impeller experiments. This might affect the acceleration of u_θ. In the calculations there are several tunable parameters: the four coefficients in the stress, the inlet and exit loss coefficients, and the initial velocity in the circumferential direction. We investigated each of the two cases in the sections which follow and examine appropriate values of the tunable parameters.

5.1 The Seal of Marquette and Childs

Using the parameter values recommended by Marquette and Childs, $n_s = n_r = 0.079$ and an exit loss of 1, the rotordynamic force for the seal in the tangential direction is predicted very well by the current model as shown by the solid line in figure 5.1. The normal force, however, exhibits a large offset from the experimental data. The calculated nondimensionalized pressure drop is 2.35, slightly below the experimental measurement of 2.5.

Now examine the effects of the adjustable parameters. As seen in figure 5.1 increasing n_s increases the magnitude of normal forces by a small amount for all whirl ratios. It also changes the slope of the tangential forces. The pressure drop increases linearly in the small range of n_s that is used. Figure 5.3 shows that increasing n_r and n_s together had effects similar to increasing n_s alone. The pressure drop varies linearly with the coefficients; the increase is about twice as large as those from increasing n_s alone. The increase in the magnitude of the normal forces is also larger, but still deviates from the experimental results by a significant offset. The change in the coefficients also changes the slope of calculated tangential forces to the whirl ratio more than that caused by changing n_s alone. The coefficient values of $n_s = n_r = 0.079$ still seem to give the best results on the tangential forces.

Varying n_r alone, however, shows a different behavior as seen in figure 5.2. The effect on the pressure drop is almost exactly the same as that for n_s, but the forces are affected differently. The normal forces exhibit almost no effects from the varying of n_r. The slope of the tangential forces, the direct damping coefficient, shows a very small effect. The main effect is the intercept of the tangential forces. So far, by varying only the coefficients, the discrepancy of the normal forces from the experimental data remain unexplained.

Introducing an entrance loss helps to reduce some of the discrepancy in the normal forces as shown in figure 5.6. With a reasonable value of 0.1, the discrepancy in the normal force is reduced by half. The change in entrance loss has only a slight effect on the tangential forces and the pressure drop. Figure 5.6 also shows that increasing the entrance loss coefficient to an unreasonable value like 0.3 produces unreasonable results, so only an entrance loss value of less than 0.1 seems to be warranted.

Reducing the exit loss shows the most promise in reducing the discrepancy in the normal forces (figure 5.4). A lowering of the exit loss coefficient increases the magnitude of the normal forces significantly. Indeed the forces seem very sensitive to small changes in the exit condition. The magnitude of change in the direct damping coefficient is also not small; it is similar to that of varying the two shear stress coefficients together.

The last tunable parameter is the value of the inlet swirl $u_\theta(0)$. As seen in figure 5.5, it has no effect on the normal forces and the slope of the tangential forces, but it does shift the tangential force curve up or down by a uniform offset. The effects seem to be similar to that of n_r, though there is not an obvious answer as to why. In addition to the parameters mentioned, the exponents on the turbulent shear stress could also be varied. Their effects, however, are very similar to that from the coefficients, and changing them would not contribute to the understanding of the problem.

In conclusion, by adjusting the various parameters, we can fit the numerical results to the experimental data. First the exit loss coefficient is lowered to eliminate the offset discrepancy in the normal forces. Then n_s adjusted to fine tune the normal forces to the experimental data, and n_r is tuned to achieve the correct slope on the tangential forces. Finally, the inlet swirl velocity is adjusted to match the tangential forces. The values which best fit the data are $n_s = 0.05$, $n_r = 0.20$, an exit loss coefficient of 0.4, and zero inlet swirl velocity. Notice that no inlet loss is used because the introduction of an inlet loss causes the added mass to become too small to be recovered through varying other parameters. The forces for the best parameters are plotted in figure 5.7. The pressure drop, however, is 3.14, significantly higher than experimental value of 2.51.

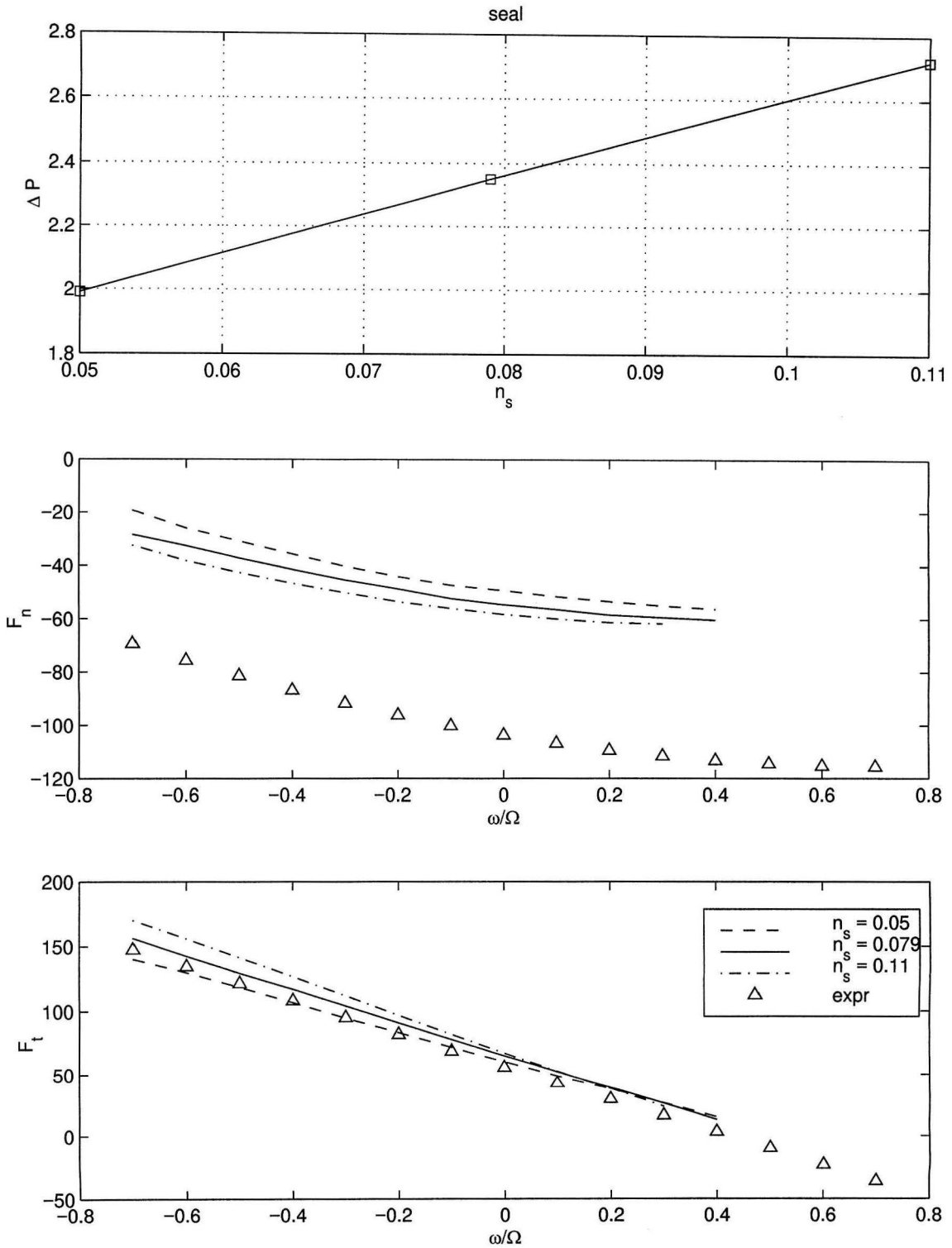

Figure 5.1: Calculated rotordynamic forces on the seal versus turbulent shear stress coefficient n_s, with no inlet losses and an exit loss coefficient of 1. Pressure drops are 1.99, 2.35, and 2.72, resp.

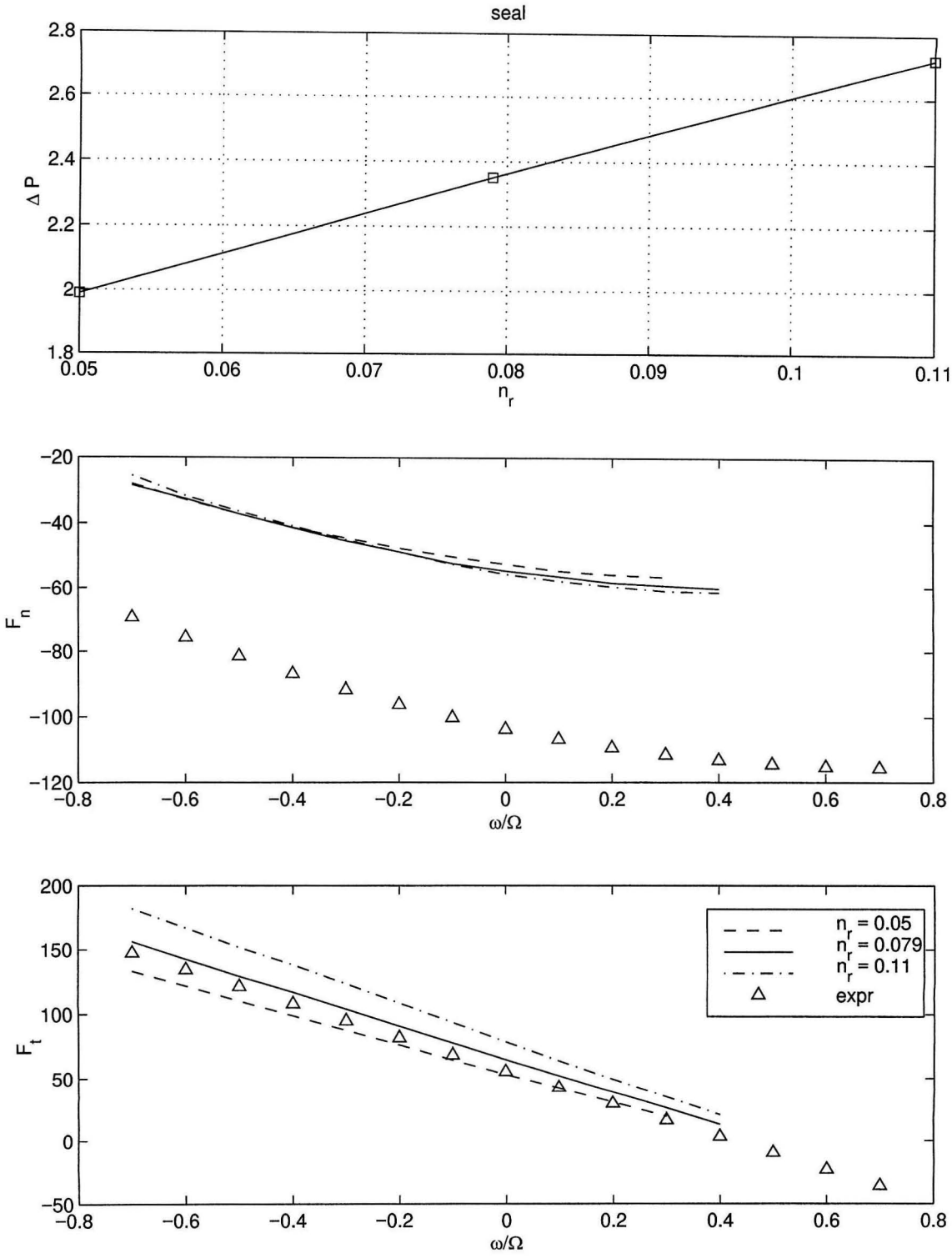

Figure 5.2: Calculated rotordynamic forces on the seal versus the turbulent shear stress coefficient n_r, with no inlet losses and an exit loss coefficient of 1. Pressure drops are 1.99, 2.35, and 2.72, resp.

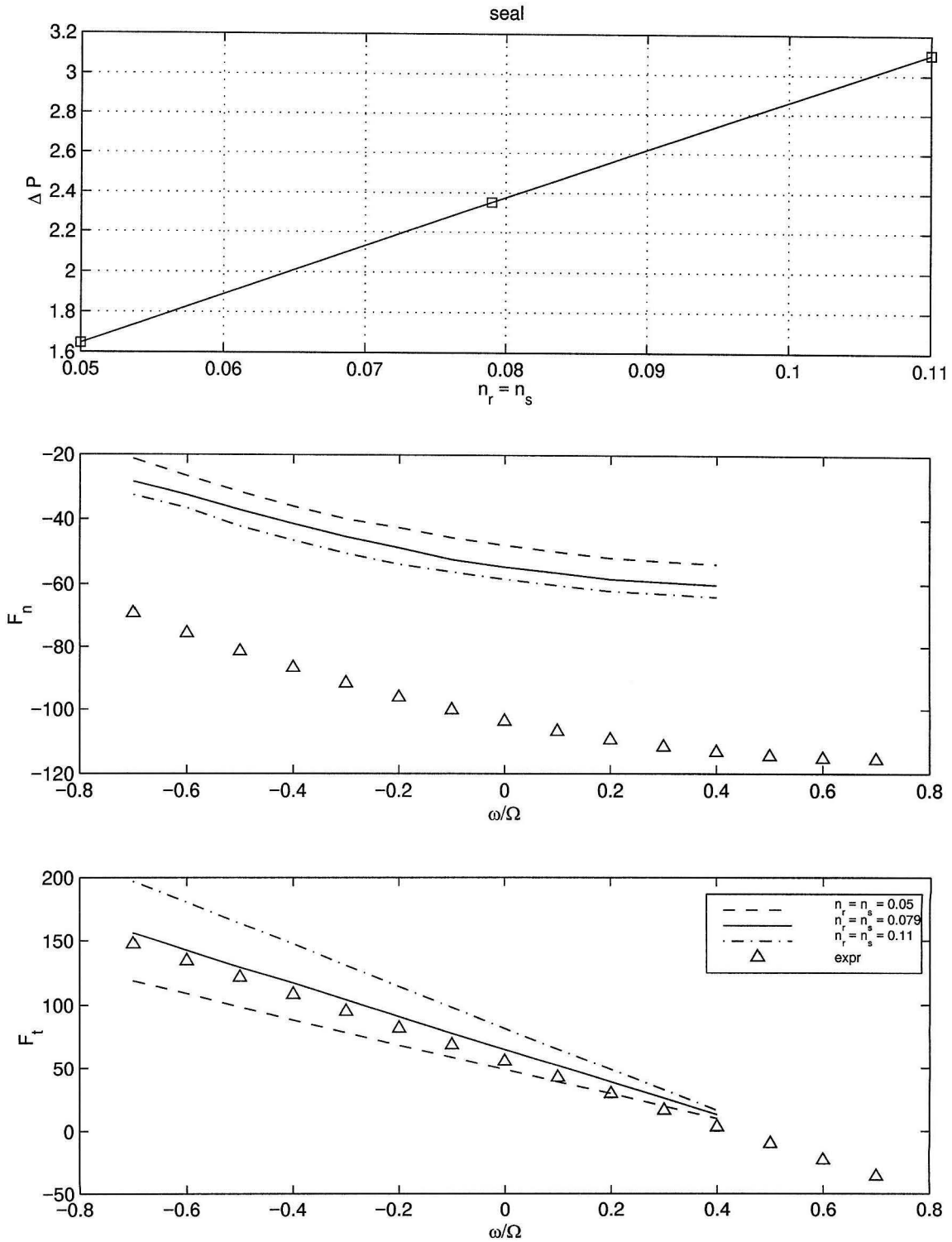

Figure 5.3: Calculated rotordynamic forces on the seal, with no inlet losses and an exit loss coefficient of 1. Pressure drops are 1.65, 2.35, and 3.10, resp.

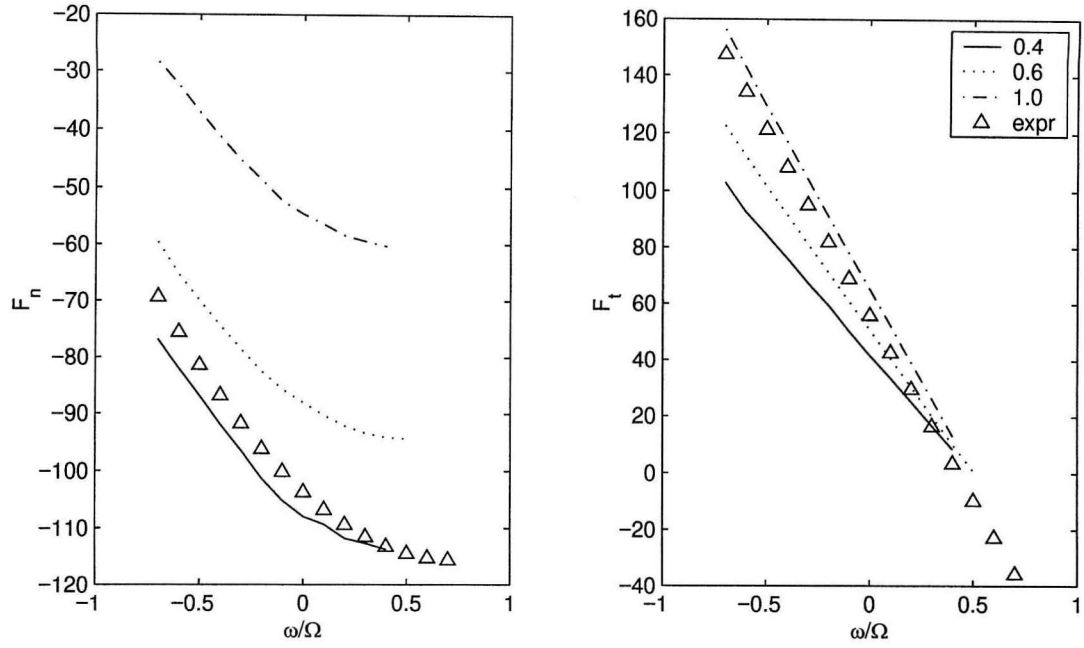

Figure 5.4: Calculated rotordynamic forces on the seal versus the exit loss coefficient, with no inlet losses and shear stress coefficients of 0.79. Pressure drops are 2.17, 2.29, and 2.35, resp.

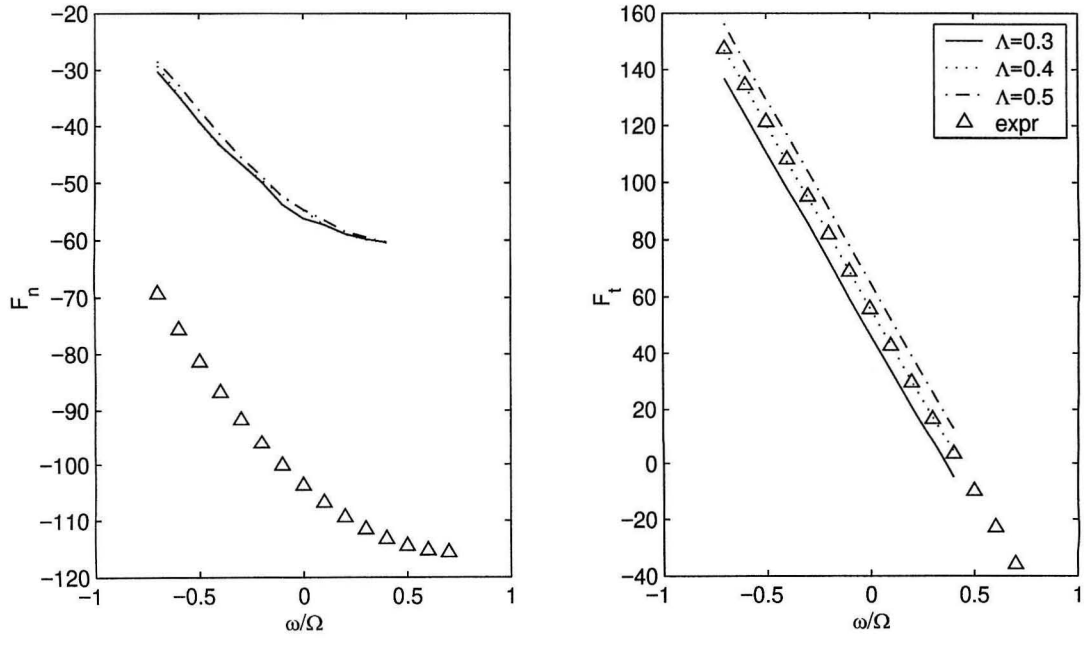

Figure 5.5: Calculated rotordynamic forces on the seal versus the inlet swirl velocity, with no inlet losses and an exit loss coefficient of 1. Pressure drops are 2.28, 2.31, and 2.35, resp.

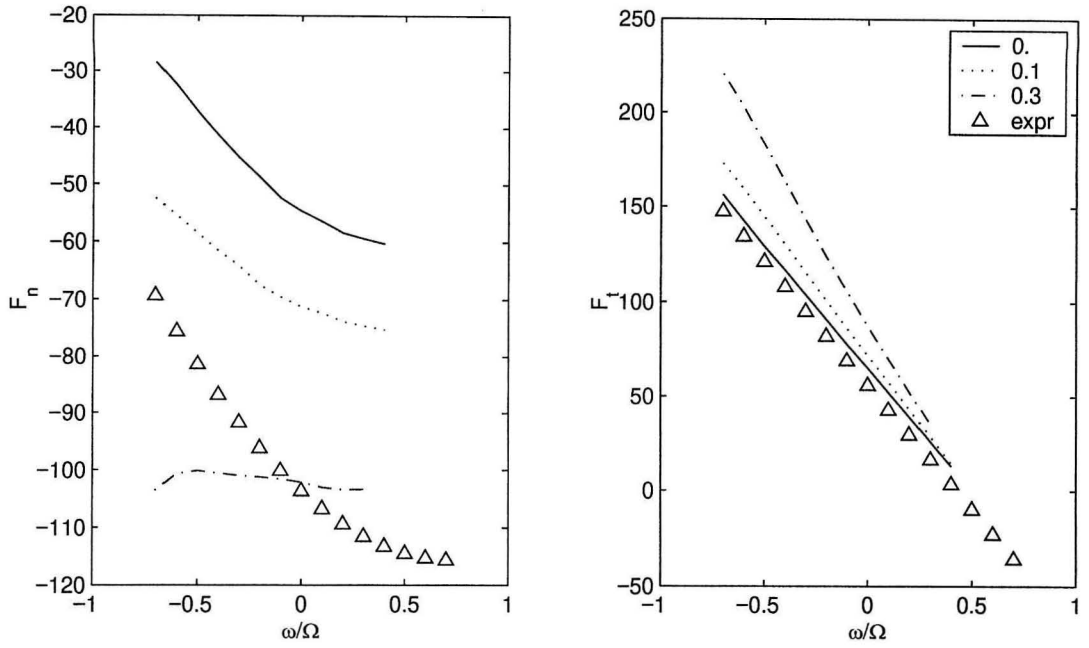

Figure 5.6: Calculated rotordynamic forces on the seal versus the inlet loss coefficient, with an exit loss coefficient of 1. Pressure drops are 2.35, 2.41, and 2.53, resp.

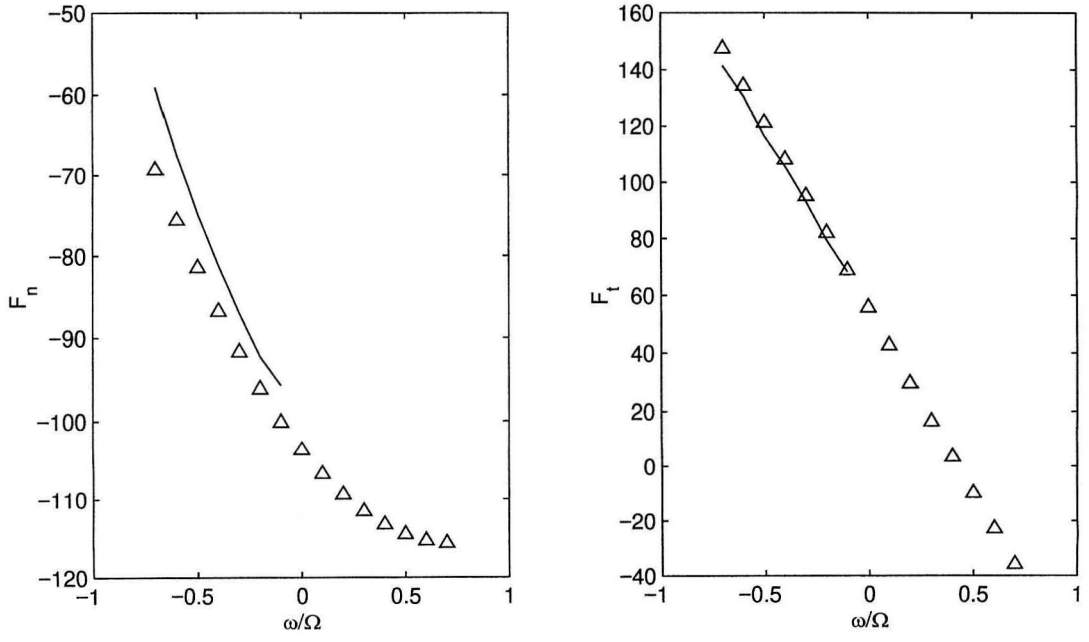

Figure 5.7: Calculated rotordynamic forces on the seal with $n_r = 0.20$, $n_s = 0.05$, no inlet loss, exit loss coefficient is 0.4, and an inlet swirl velocity of zero. Pressure drop is 3.14

5.2 Meridional Pressure Distribution For the Conical Impeller

In this section, we compare the measured meridional pressure distributions to the predictions from theory. Some of the experimental data were already presented in section 3.4. The data used for comparison is that from the circumferential location where clearance is equal to the average clearance. It happens that the shear stress coefficients do not affect the initial slope of the pressure profile, neither do the inlet or exit loss coefficients. The inlet swirl velocity, however, has a significant impact on the initial stages of the profile. This allows predictions of the inlet swirl rates that occurred in the experiments.

Figures 5.9 and 5.10 shows the pressure profiles as a function of the inlet swirl rate. The pressure measurements are best matched by setting the inlet swirl velocity equal to 0.23 times the rotor tip velocity for all three flow rates.

The finding was the motivation behind the inlet swirl measurements presented in section 3.5. Those measurements do confirm the suspicion that in the experiments the inlet swirl to the leakage path is roughly constant for different flow rates. One peculiarity that does arise in the model is that for different flow rates, the pressure at the exit is the same (figure 5.12). This does not appear to be the case experimentally, though the difference is small.

Because the leakage flow geometry is non-axisymmetric, the pressures profiles vary when measured at different circumferential locations. Figure 5.11 compares the calculations to the experimental pressure profile at several different circumferential positions (the numbers under eccentricity represent degrees from points of maximum clearance in the direction of the swirl). The graph shows very good agreement between the theory and measurements, again by using the measured swirl velocity.

Unlike the swirl vanes, the radial vanes worked as intended for larger flow coefficients. Figure 5.13 compares the calculated pressure profiles using zero inlet swirl to the experimental data obtained with the anti-swirl vanes guiding the leakage flow. The results match up reasonably well. The experimental pressure profiles, however,

do not vary with flow rate, while the calculated results show decreasing pressure profiles for increasing flow coefficients. With good agreements between the experimental and numerical pressure profiles, we can express confidence in the theory and move on the the more difficult task of predicting rotordynamic forces.

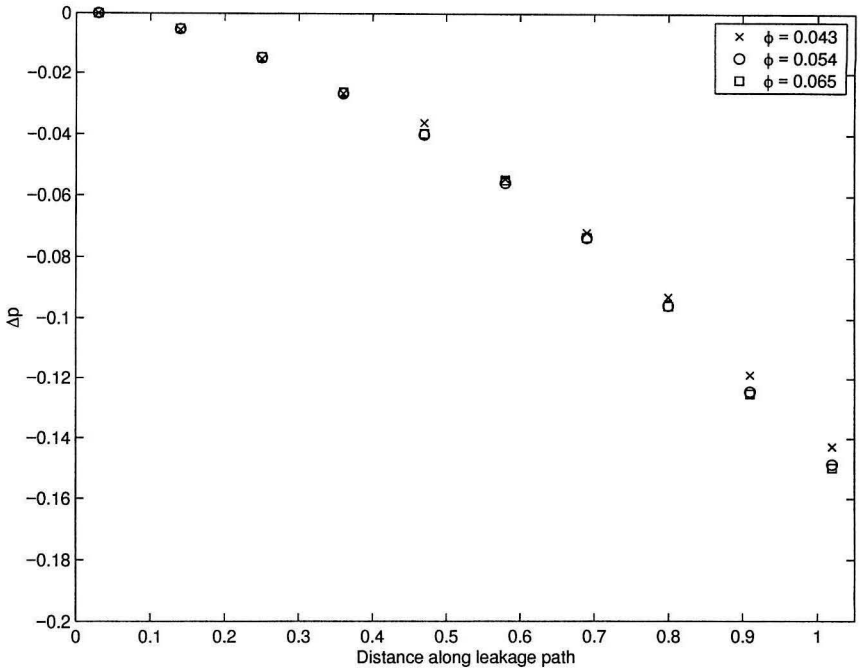

Figure 5.8: Experimental non-dimensionalized pressure profile for different flow coefficients using the 6 degree inlet swirl vane, zeroed about the first data point versus non-dimensionalized length, 0 is leakage path inlet and 1 exit

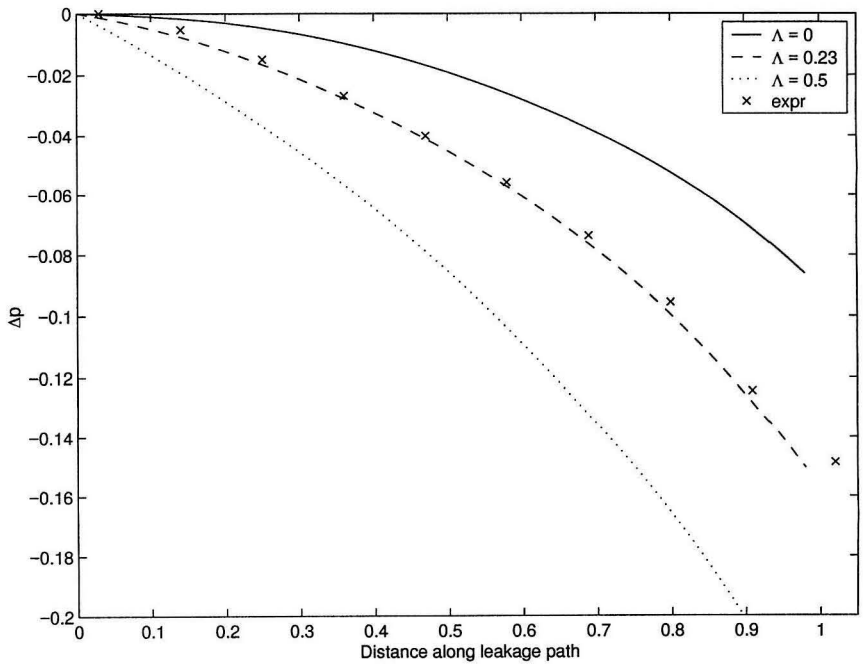

Figure 5.9: Comparison of experimental data (6 degree swirl vane used) with calculated pressure profile for different inlet swirls, $\phi = 0.054$

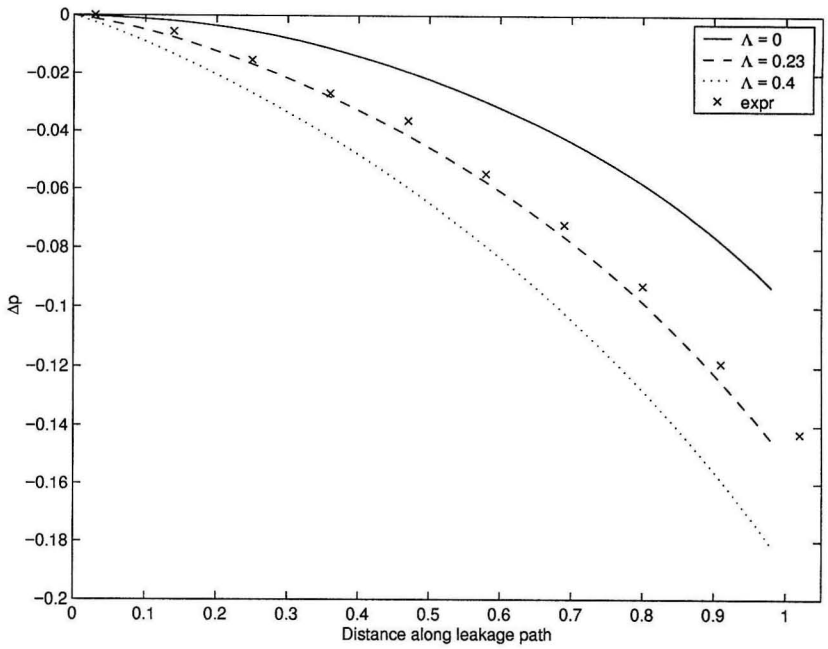

Figure 5.10: Comparison of experimental data (6 degree swirl vane used) with calculated pressure profile for different inlet swirls, $\phi = 0.04$

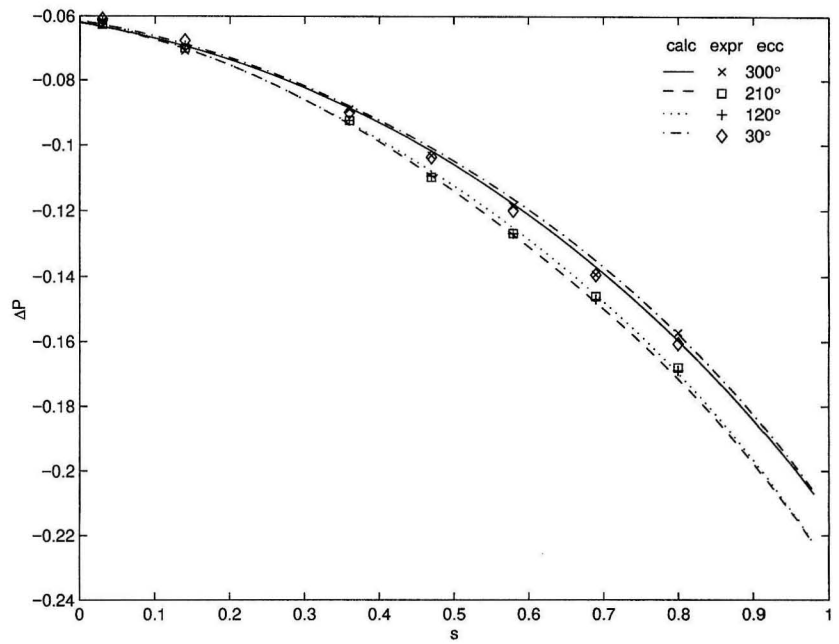

Figure 5.11: Comparison of the experimental data (2 degree swirl vane) with calculated pressure profile for a flow coefficient of 0.54, and an inlet swirl rate of 0.26. The calculated pressure was re-zeroed to match the data from the experimental pressure at the first pressure tap, which represents the pressure difference to the fluid pressure before entering the inlet swirl vanes

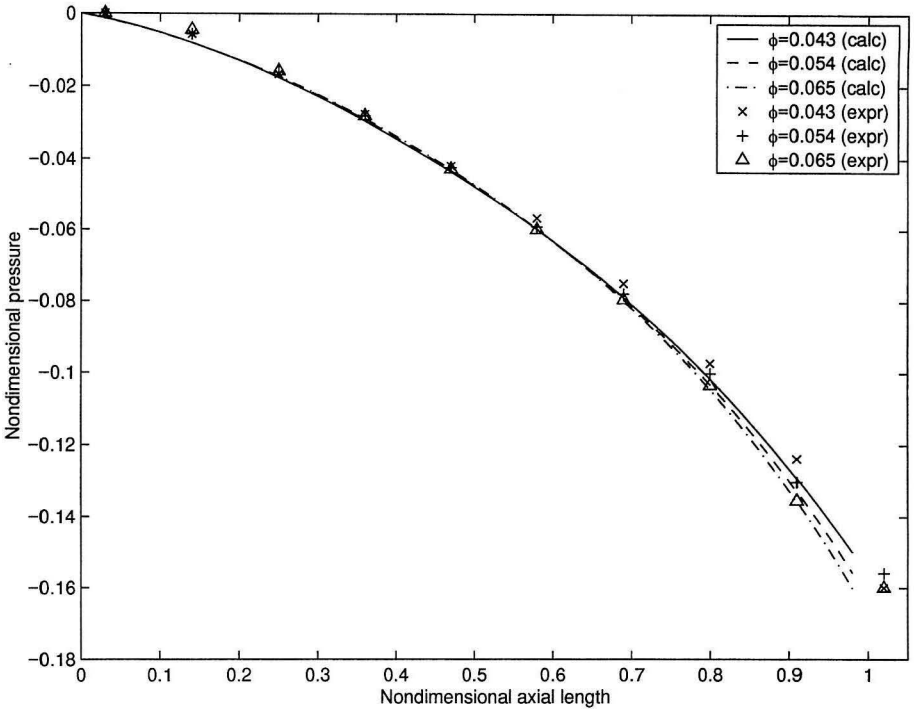

Figure 5.12: Comparison of experimental data with calculated pressure profile

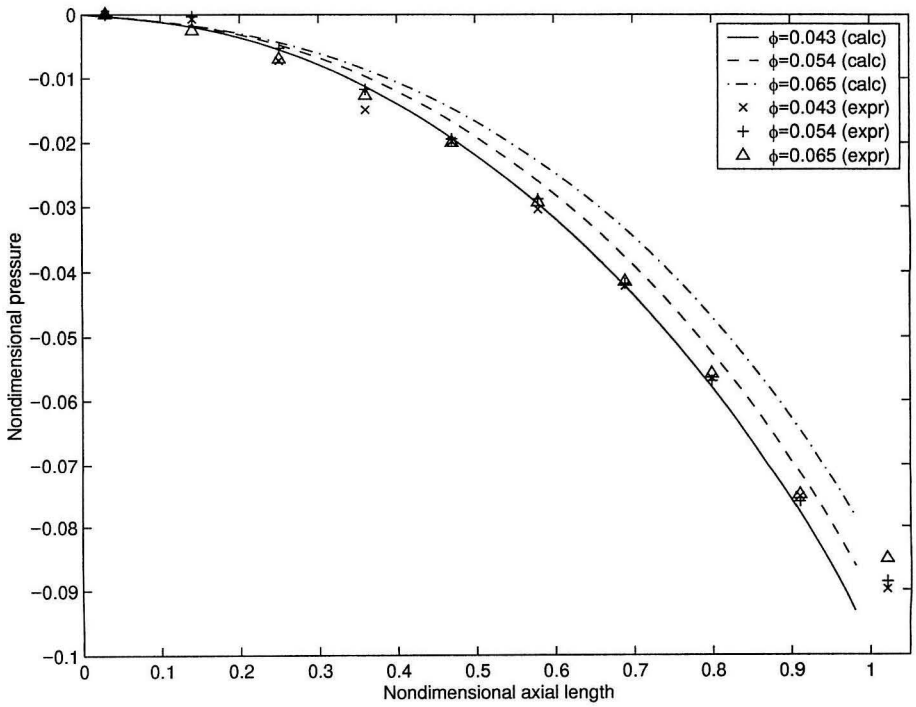

Figure 5.13: Comparison of experimental pressure profiles (radial anti-swirl vanes) with calculated profiles for a rotor speed of 500 rpm

5.3 Conical Impeller

In this section, we examine the accuracy of the calculated results from the bulk flow model by comparing the rotordynamic forces for the conical impeller to that of the experimental data. As a result of the inlet swirl measurements, an inlet swirl ratio of 0.26 was used for calculations of rotordynamic forces with the conical impeller geometry. Numerical results for flow coefficients of 0.04 and 0.053 are compared with experimental measurements in figure 5.14. Had the fluid flow followed the guide vanes, the inlet swirl ratios would be 1.1 and 1.5 respectively. This data uses $n_s = n_r = 0.079$ for the shear stress coefficients and an exit loss coefficient of 1. The tangential forces agree reasonably with the experimental data. The normal forces, however, predict the added mass and the cross-coupled damping coefficients that are much smaller than the experimental results. The direct stiffness agrees well with the experiments.

The experimental data show very similar forces for the two different coefficients of 0.04 and 0.053. This is consistent with the calculated forces using the same inlet swirl rate for both coefficients. Results presented in section 3.5 indicate that the inlet swirl ratio is about 0.26 for all flow coefficients, and the rotordynamic forces corroborate this.

Figure 5.14 also shows the calculated rotordynamic coefficients using Childs' perturbation model. Compared with the Childs' model, the current model gives better predictions for the direct stiffness and cross-coupled stiffness coefficients as well as the whirl ratio. The direct damping coefficient is well predicted by both, while both underpredict the added mass term significantly. Childs' model gives more accurate results for the cross-coupled damping coefficient.

Looking at the rotordynamic force plots in figures 5.15 and 5.16, there are several places where the forces exhibit erratic behavior with whirl frequency which is reminiscent of the "resonances" in the data of Childs (1989). These are not supported by experimental results, and appear to arise from the bulk flow equations themselves. The current model does seem to be less plagued with them than the Childs' perturbation method results.

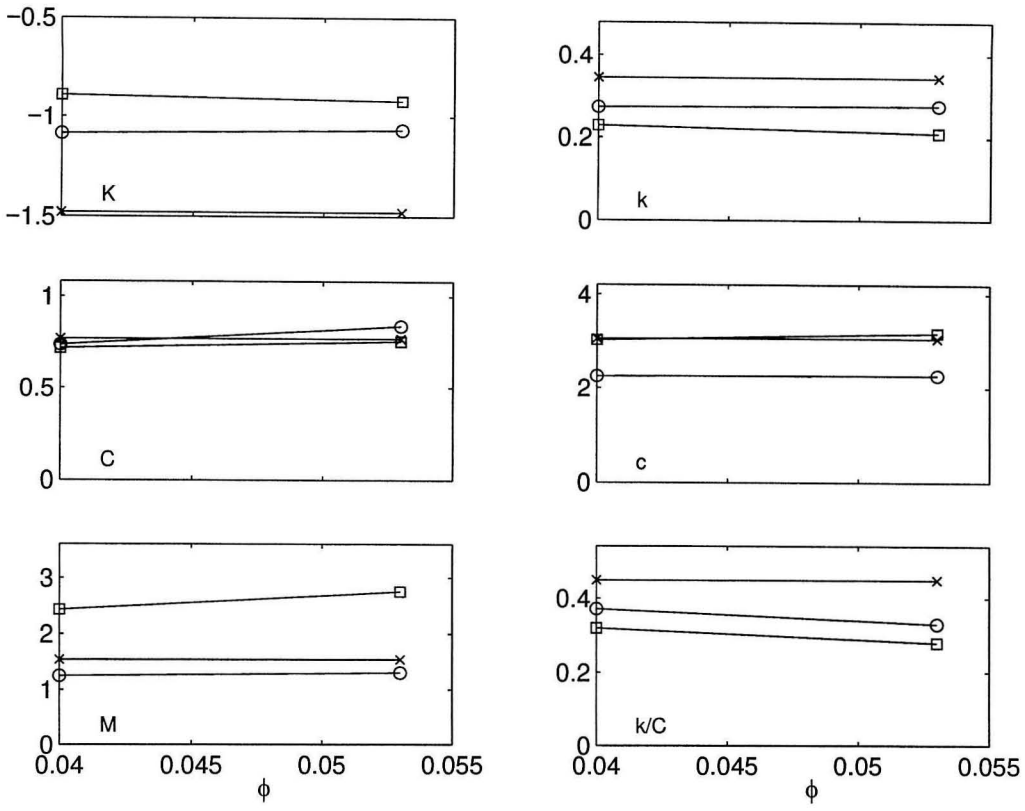

Figure 5.14: Comparison of rotordynamic coefficients versus flow coefficient ϕ between experiment ($\square$), and current model ($\circ$), and Childs' perturbation model ($\times$) for the conical impeller

5.4 Contoured Impellers

The calculations for the contoured impeller are similar to the results for the conical impeller. Figure 5.17 shows that the added mass and the cross-coupled damping coefficients for the contoured impeller are significantly smaller than the experimental data, while the direct stiffness matches up well. As for the tangential forces, the direct damping and cross coupled stiffness agree reasonably with the measured values. Just by looking at the coefficients in figure 5.17, it may appear that some calculated coefficients exhibit a different trend than the experiments. Looking at the plot of experimental rotordynamic forces for different flow rates in figure 5.20, however, shows that looking at such trends is of dubious merit at best. The forces for the three different flow rates are almost exactly the same. This is consistent with the measurements

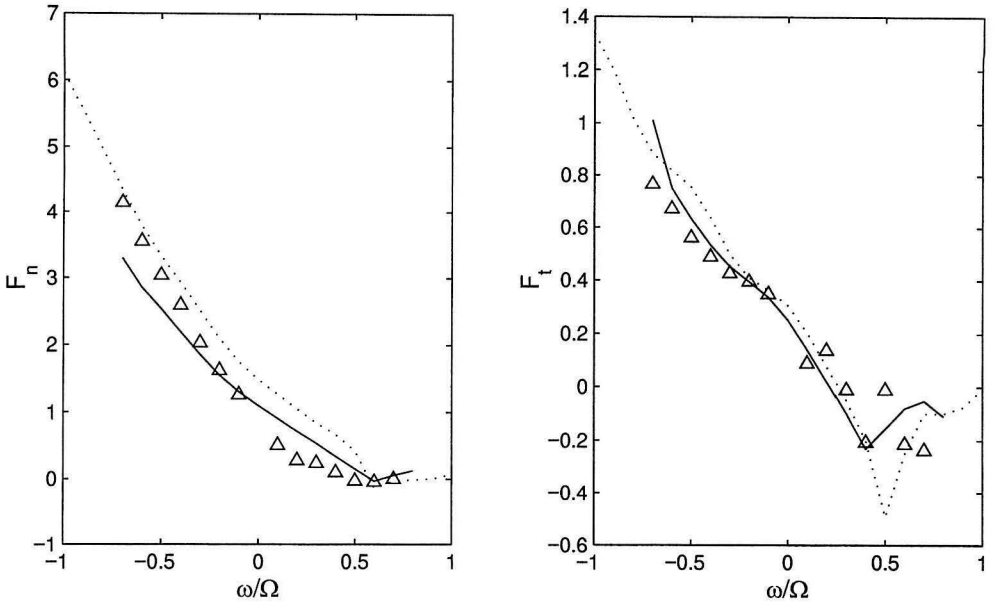

Figure 5.15: Comparison of rotordynamic forces versus whirl frequency ratio between experiment and calculations for the conical impeller at a flow coefficient of 0.04; current model (–), Childs' perturbation model (· · ·), both using an inlet swirl velocity of 0.27

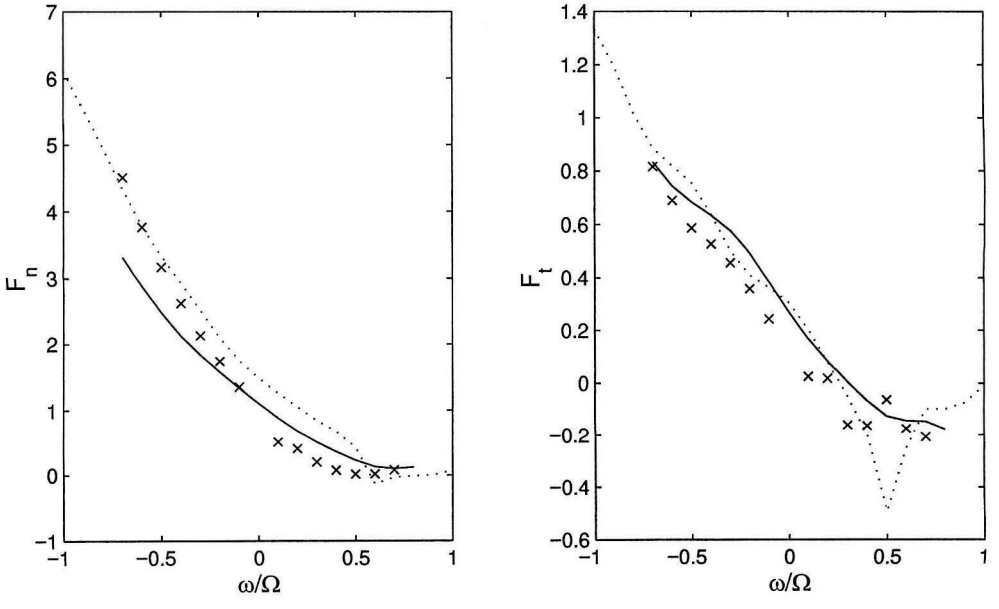

Figure 5.16: Comparison of rotordynamic forces versus whirl frequency ratio between experiment and calculations for the conical impeller at a flow coefficient of 0.053; current model (–), Childs' perturbation model (· · ·), both using an inlet swirl velocity of 0.27

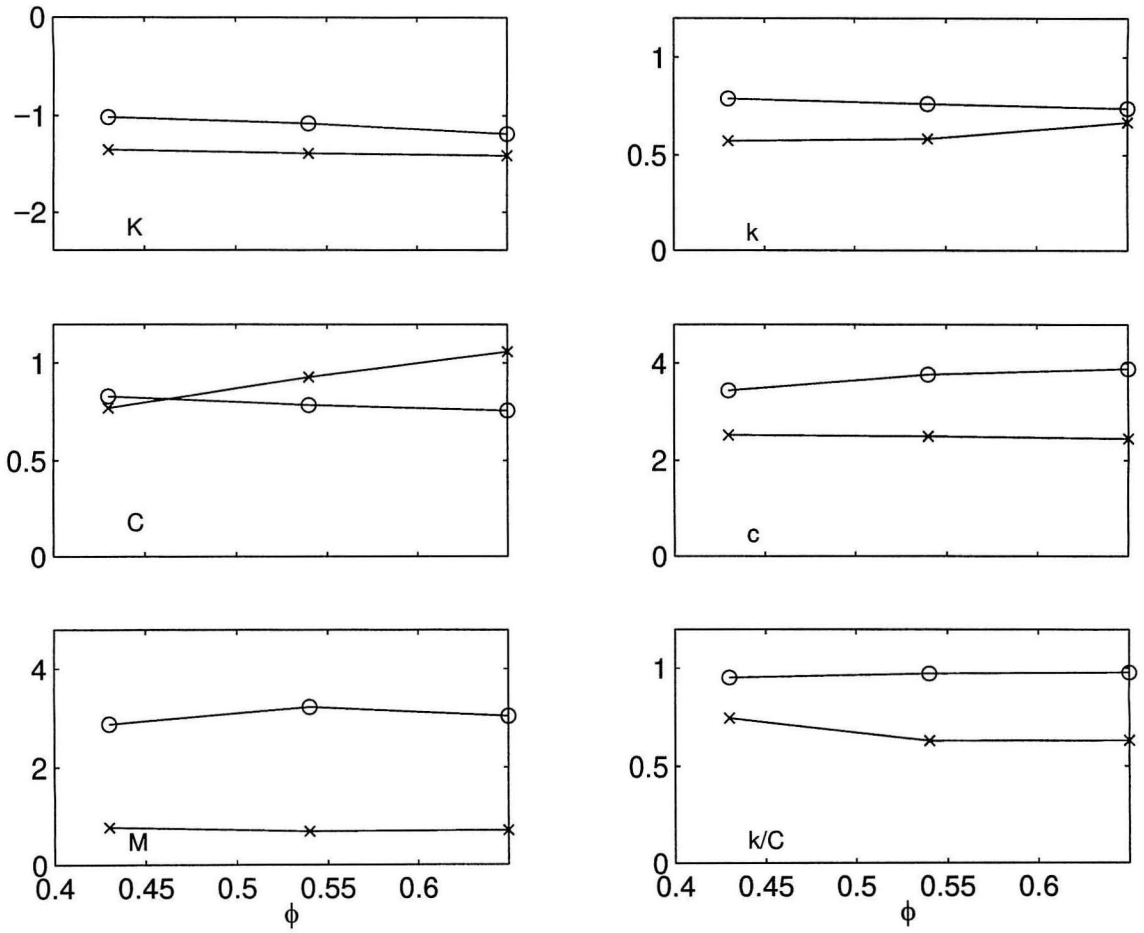

Figure 5.17: Comparison of rotordynamic coefficients versus flow coefficient ϕ between experiment ($\circ$) and calculations ($\times$) for the contoured impeller using an inlet swirl coefficient of 0.26

that the flows have the same inlet swirl rates.

Figure 5.18 shows the rotordynamic force coefficients which result from curve fitting at the positive whirl frequency ratios only. For most applications, this is the range that most interests rotordynamists. The predicted direct stiffness coefficients become slightly worse, but the predictions for the added mass and cross-coupled damping coefficients are significantly improved. The coefficients from the tangential forces are both underpredicted.

The effect of small changes in the inlet swirl rates on the forces can be seen in figure 5.22. The inlet swirl does little to the normal forces, but causes destabilization in the tangential forces. However, whether the tangential forces will show the behavior seen

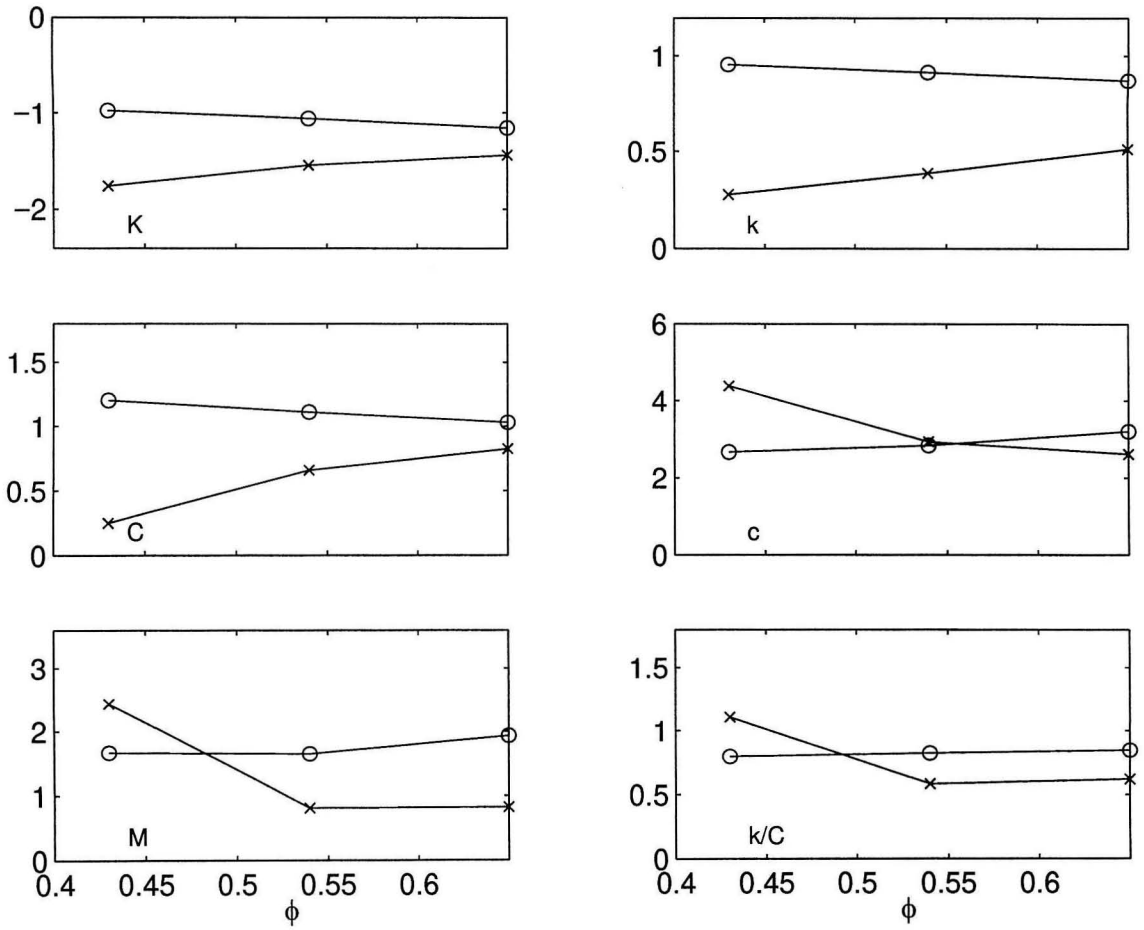

Figure 5.18: Comparison of rotordynamic coefficients versus flow coefficient ϕ between experiment ($\circ$) and calculations ($\times$) for the contoured impeller using an inlet swirl coefficient of 0.26 for positive whirl only

in figure 5.21 at high inlet swirl velocity remains unclear.

A comparison of the coefficients for the flows with no inlet swirl is shown in figure 5.19. The model shows good results for the tangential force coefficients. The coefficients for the normal forces, however, were all underpredicted, though they do show the right trends.

5.5 Short Contoured Impeller

The final impeller that was tested is referred to as the short contoured impeller. It has a much larger eye-to-tip diameter ratio and much smaller axial length compared

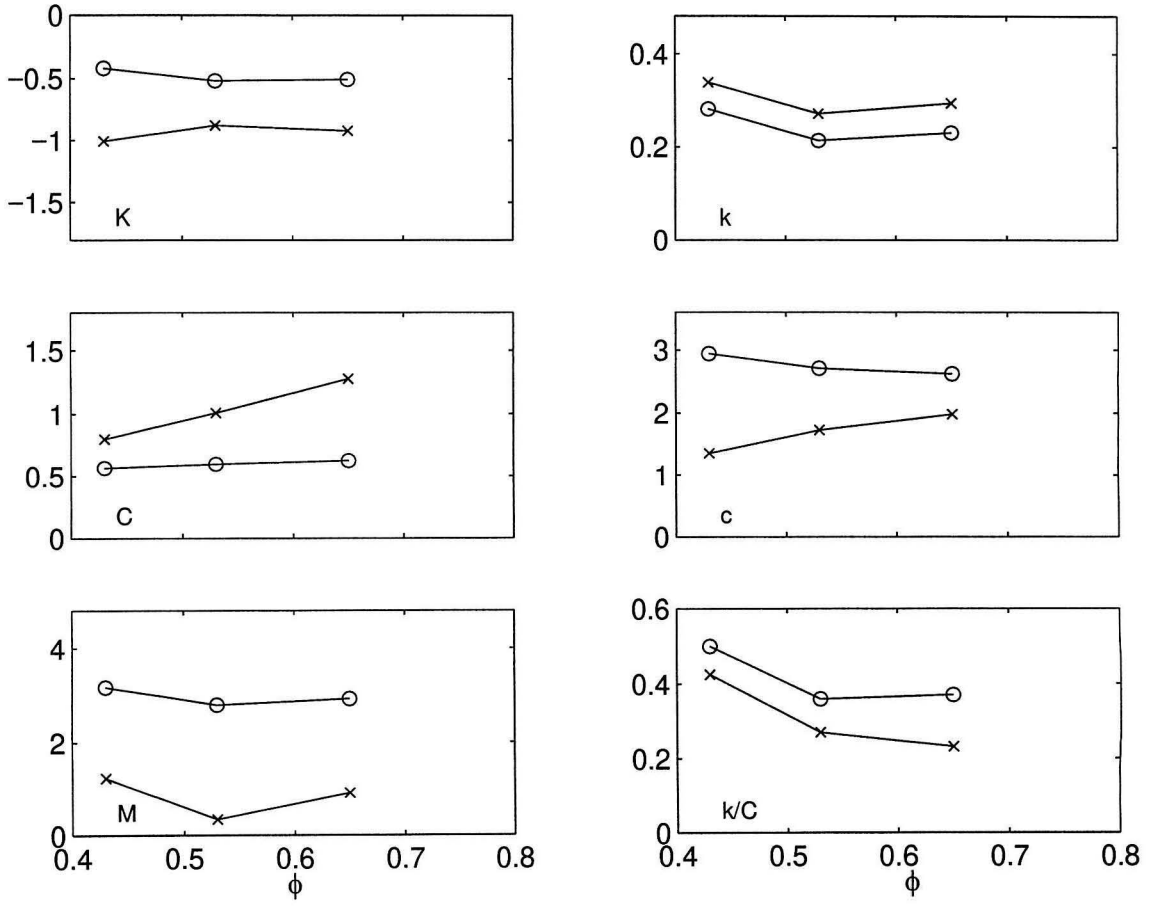

Figure 5.19: Rotordynamic coefficients for experiment (○) and calculation (×) on the contoured impeller with no inlet swirl

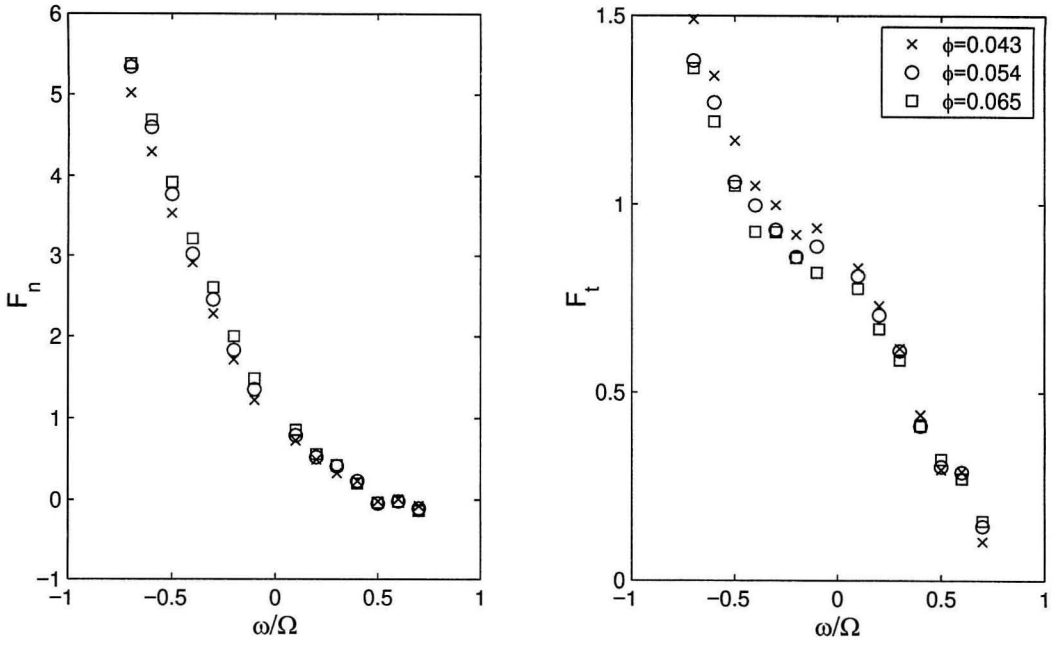

Figure 5.20: Experimental results for the contoured impeller with inlet swirl

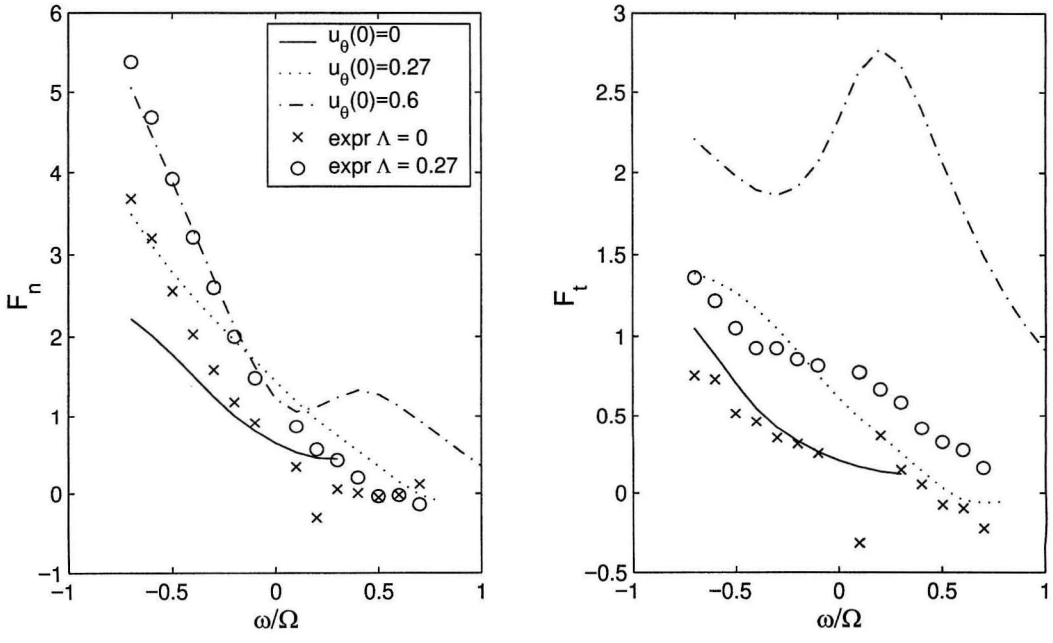

Figure 5.21: Comparison of rotordynamic forces versus whirl frequency ratio between experiment and calculation for the contoured impeller at a flow coefficient of 0.065

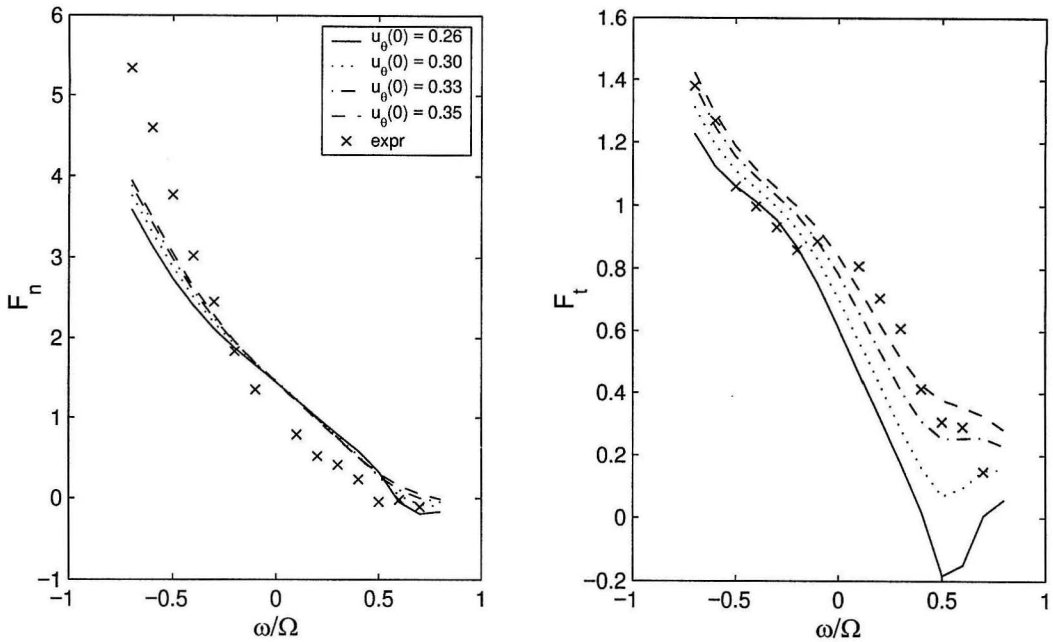

Figure 5.22: Rotordynamic forces versus whirl frequency ratio for experiment and calculation on the contoured impeller at a flow coefficient of 0.054 using various inlet swirl coefficients.

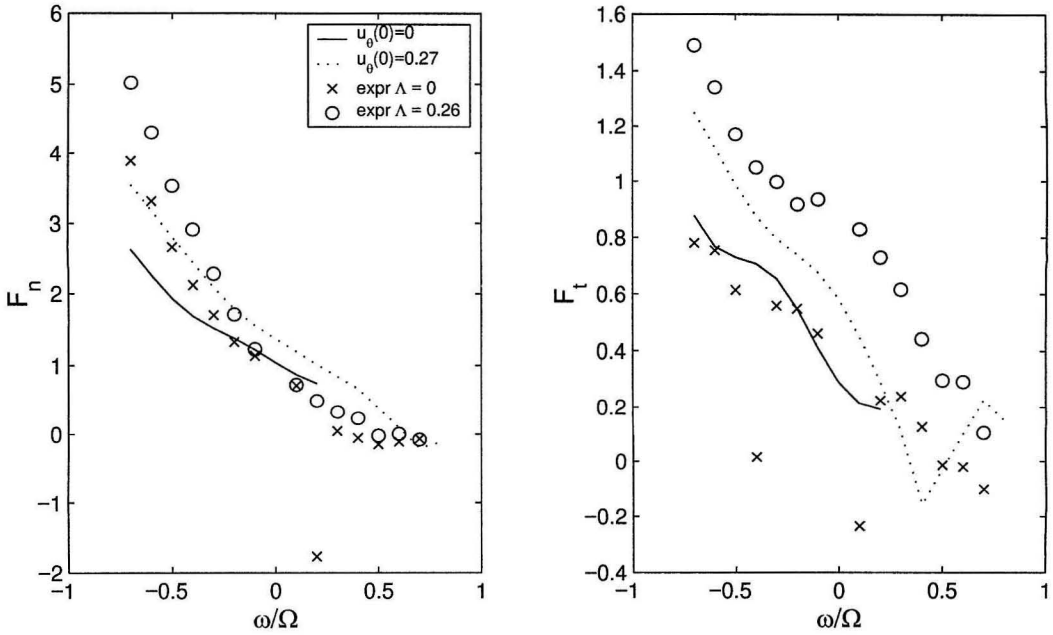

Figure 5.23: Rotordynamic forces versus whirl frequency ratio for experiment and calculation on the contoured impeller at a flow coefficient of 0.043

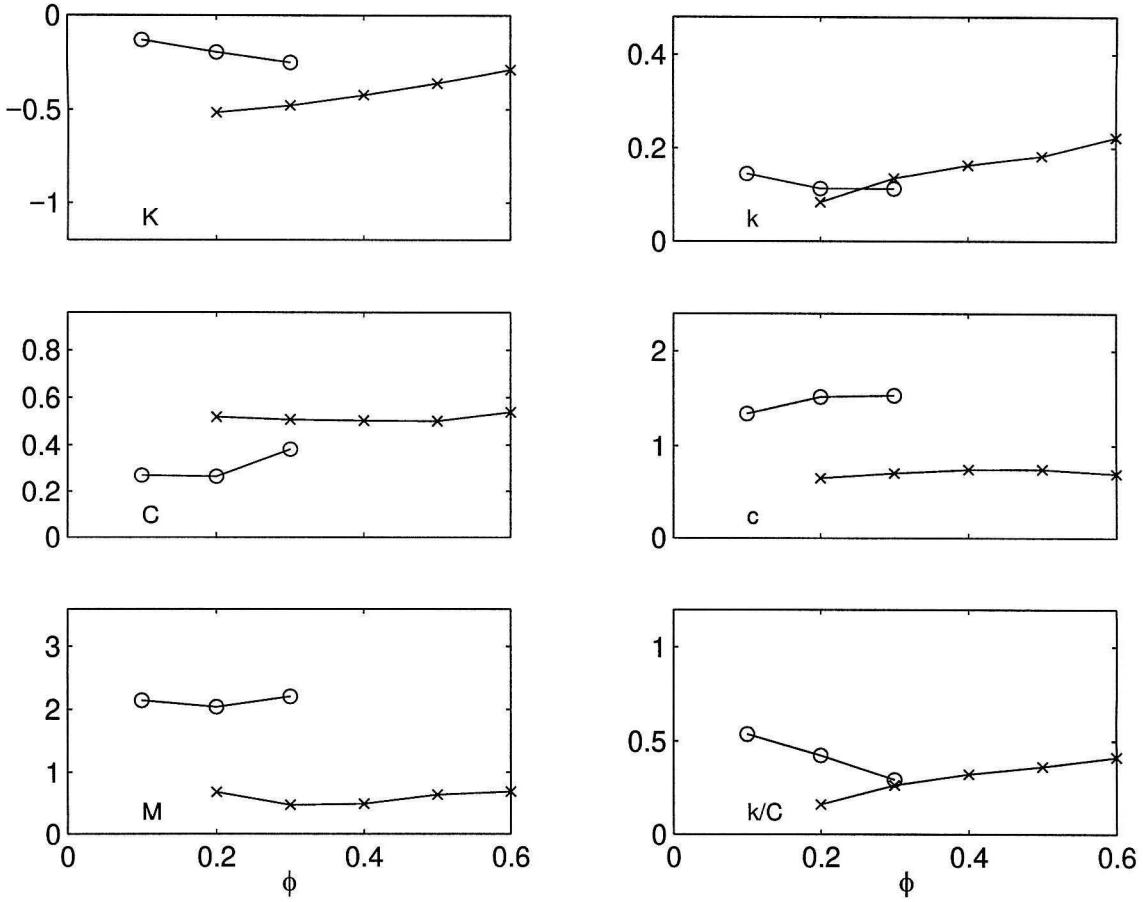

Figure 5.24: Comparison of rotordynamic coefficients on the short contoured impeller between experiments (○) and calculations (×)

to the conical and the contoured impellers discussed in the previous sections (see figure 2.4). The experimental measurements were conducted without the presence of any inlet guide structure. Pitot tube measurements indicated that the inlet swirl coefficient under such conditions is slightly smaller than that tested with an inlet swirl passage, namely an inlet swirl coefficient of 0.2 rather than 0.26.

The calculations show similar results to those for the contoured impeller. Figure 5.24 shows that the added mass and the cross-coupled damping coefficients for the impeller are significantly smaller than the experimental data, as was the case for the other two impellers. The direct stiffness matches up well. The trend seem to be off for some of the rotordynamic coefficients. However an examination of figure 5.25 reveals that these trends are merely a result of the curve fitting of noisy data and should

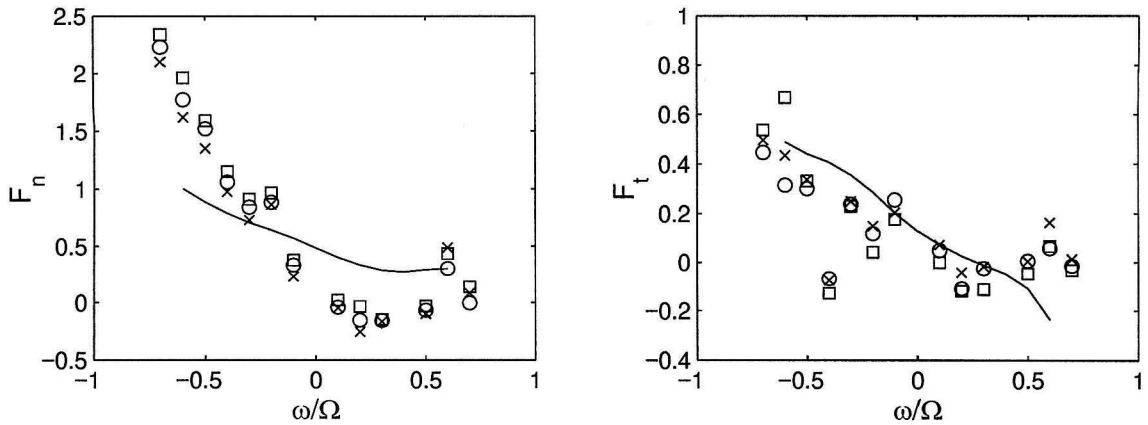

Figure 5.25: Comparison of rotordynamic forces on the short contoured impeller between experiments, $\phi = 0.01(\times), \phi = 0.02(\circ), \phi = 0.03(\square)$, and calculations for $\phi = 0.03$ (solid line)

not be considered to be important. As for the tangential forces, the direct damping and cross coupled stiffness agree reasonably with the measured values. Figure 5.25 shows that the measured values for the tangential forces are highly nonlinear, but the calculations match the data very well. When experiments were conducted on the short contoured impeller, the eccentric drive could not lock in at a whirl frequency ratio of 0.4, perhaps due to effects of its natural frequency. This may account for the fact that the tangential forces for a whirl frequency ratio of -0.4 are much lower than those at neighboring whirl frequencies.

5.6 Effects of Input Parameters

The bulk flow model has several tunable parameters that affect the normal and tangential rotordynamic forces. This section explores their effects on the calculated forces for the conical impeller.

Changes in the turbulent shear stress coefficient n_s cause a linear change in the overall pressure drop (figure 5.27). Increasing n_s, however, lowers the pressure drop and the normal forces. The normal force decreases by a fixed constant across the negative whirl ratios when n_s is increased. Lowering the value of n_s also reduces the resonance in the tangential forces. With $n_s = 0.05$ and $n_r = 0.079$, the resonance is

almost completely eliminated for an inlet swirl of 0.5.

Figure 5.26 shows increasing n_r increases the pressure drop and the normal forces, unlike the effect of increasing n_s. The pressure drop change is smaller than that from changing n_s. The normal forces increase by a small constant amount for all whirl ratios; the constant is also smaller than that for n_s. Increasing the value of n_r seems to reduce the resonance behavior. Judging by the negative whirl ratio range of -0.7 to -0.2, the tangential forces also increase with n_r. It appears that an increase in pressure drop reduces the resonance in the calculations.

Increasing the two shear stress coefficients together lowers the pressure drop and the normal forces. This result could have been anticipated since the effects of the n_r on these are smaller than the effects of n_s. The same logic would lead to the conclusion that the tangential forces would increase, as is indeed the case (see figure 5.28). Larger values of n_r and smaller values of n_s seem to dampen the resonance in the tangential forces.

The exit loss coefficient does not have an effect on the rotordynamic normal forces. Judging by figure 5.30, it has some slight effect on the tangential forces in the negative whirl region. An increase in inlet swirl velocity, $u_\theta(0)$, increases the tangential forces, and also enhances the resonance. The effect of inlet swirl on the calculated normal forces is unclear from figure 5.29, although it does appear to change the added mass.

Using a low value for n_s does seem to remove the resonance-like behavior. Increasing n_r then lowers the normal forces and increases the direct damping in the tangential forces.

The above calculations were all perturbations upon an inlet swirl coefficient of 0.5 for the conical impeller. The contoured impeller exhibits some different trends perturbed about an inlet swirl coefficient of 0.26 and a flow coefficient of 0.53. Figure 5.31 shows the effect of increasing the two shear coefficients together on the calculations for the contoured impeller. The normal rotordynamic force is unchanged, while there is a slight increase in the tangential force when the coefficients are increased.

As show in figure 5.32, when only n_r is increased, both the normal and tangential forces increase slightly. The resonance seems to be reduced with a lower value of

n_r. The normal forces decrease when only n_s is increased, while the tangential forces remain largely unchanged (figure 5.33). None of the changes in the rotordynamic forces caused by adjusting the shear stress coefficients appear to be significant.

For both the conical and contoured impeller, tuning of parameters fail to increase the curvature of the normal forces versus the whirl frequency ratio. This leaves a somewhat unsatisfactory prediction for the rotordynamic coefficients arising from the normal forces.

5.7 Limitations of the Numerical Algorithm

The implementation of the numerical algorithm described in the previous chapter can not be applied as universally as one would wish. Currently the inputs to the program are the tunable parameters mentioned in the preceding section, the shear stress coefficients, the inlet and exit loss coefficients, and the inlet swirl coefficient. Additional inputs are the flow coefficient and the rotational speed of the impeller plus the leakage path geometry, which include the average clearance and eccentricity. Currently the computational grid of the leakage path is equally spaced, though modifications can be easily made to accommodate variable spacing.

Because one component of the algorithm is a forward integration procedure, the program will not work for flows when backflow occurs. As mentioned in the introduction, backflow in leakage path typically occurs near inlet close to the impeller. Since the bulk flow equations only calculate the velocity averaged across the clearance, we do not need to worry about backflow unless at some location the mean flow, gap averaged, is going backwards. As seen from figure 5.34, this type of backflow does not occur until the eccentricity becomes large relative to the leakage path clearance. For smaller flow coefficients, this can occur more readily. The easy remedy for these situations is to reduce the eccentricity, as the rotordynamic forces varies linearly with respect to eccentricity for almost all calculations that were performed. There are instances, however, where reducing the eccentricity will not help. Those situations are believed to be cases where resonance occurs from the bulk flow equations. This

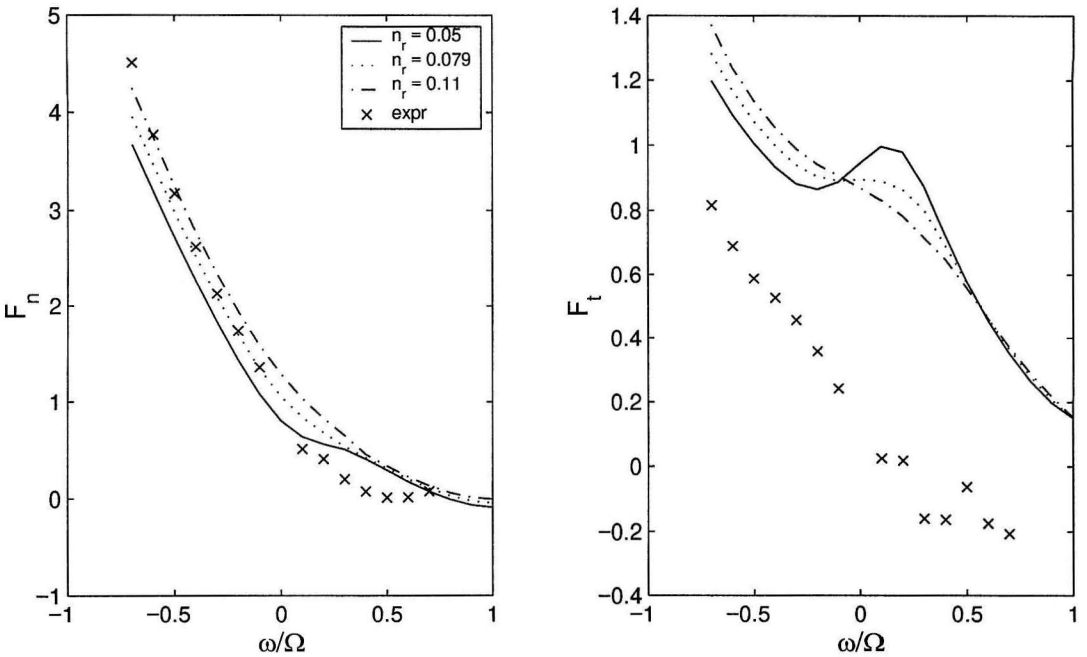

Figure 5.26: Calculated rotordynamic forces on the conical impeller with flow coefficient of 0.06, $n_s = 0.079$, no inlet loss, exit jet loses all dynamic head, and an inlet swirl of 0.5. Pressure drops are 0.77, 0.79, 0.81

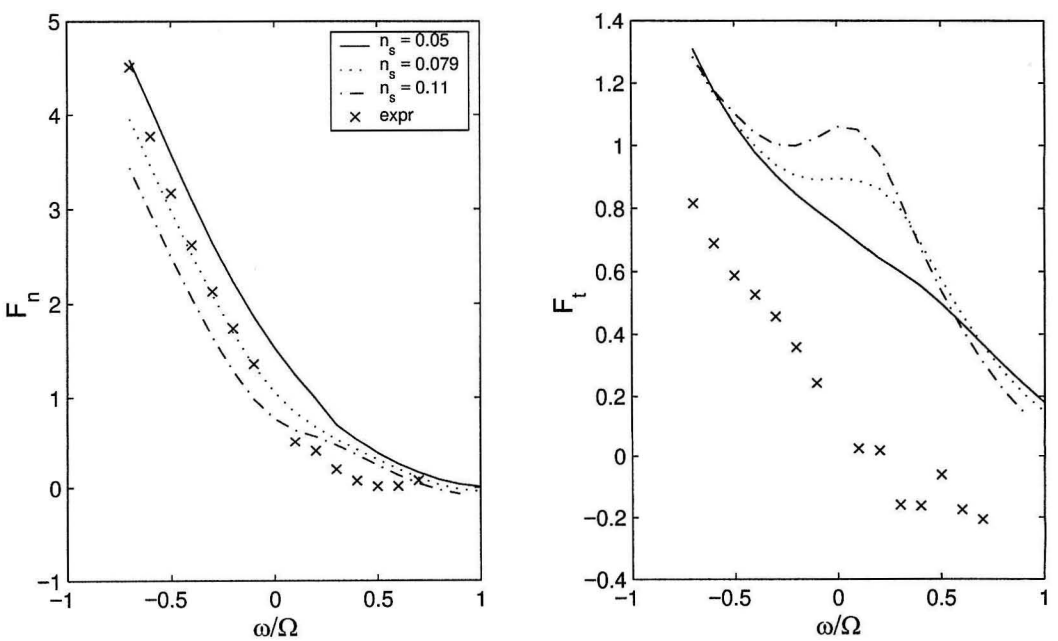

Figure 5.27: Calculated rotordynamic forces on the conical impeller with flow coefficient of 0.053, $n_r = 0.079$, no inlet loss, exit jet loses all dynamic head, and an inlet swirl of 0.5. Pressure drops are 0.85, 0.79, 0.75

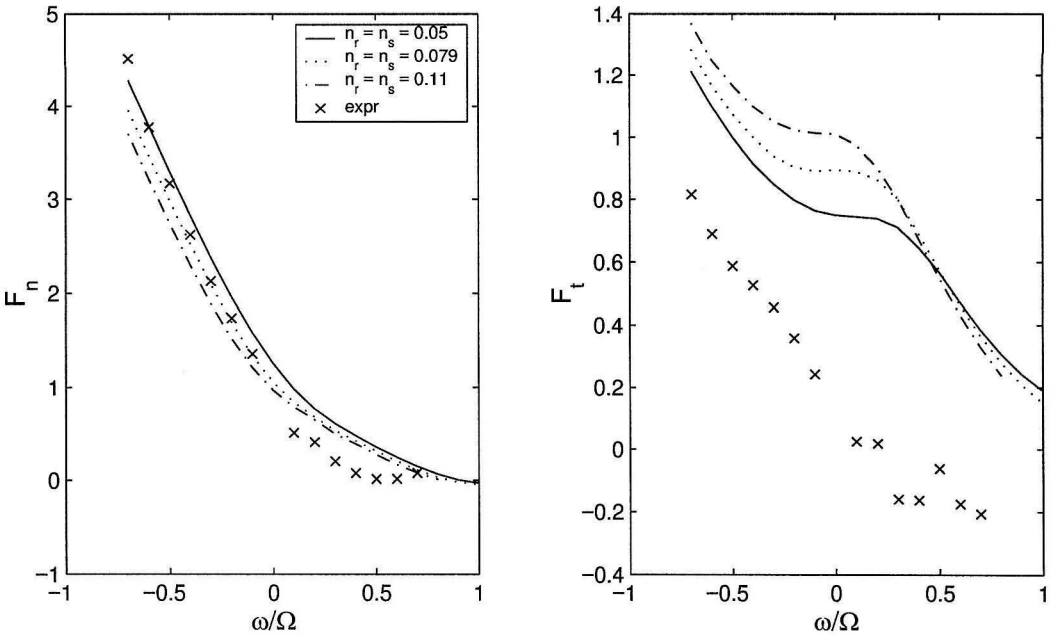

Figure 5.28: Calculated rotordynamic forces on the conical impeller with flow coefficient of 0.053, no inlet loss, exit jet loses all dynamic head, and an inlet swirl of 0.5. Pressure drops are 0.88, 0.79, 0.76

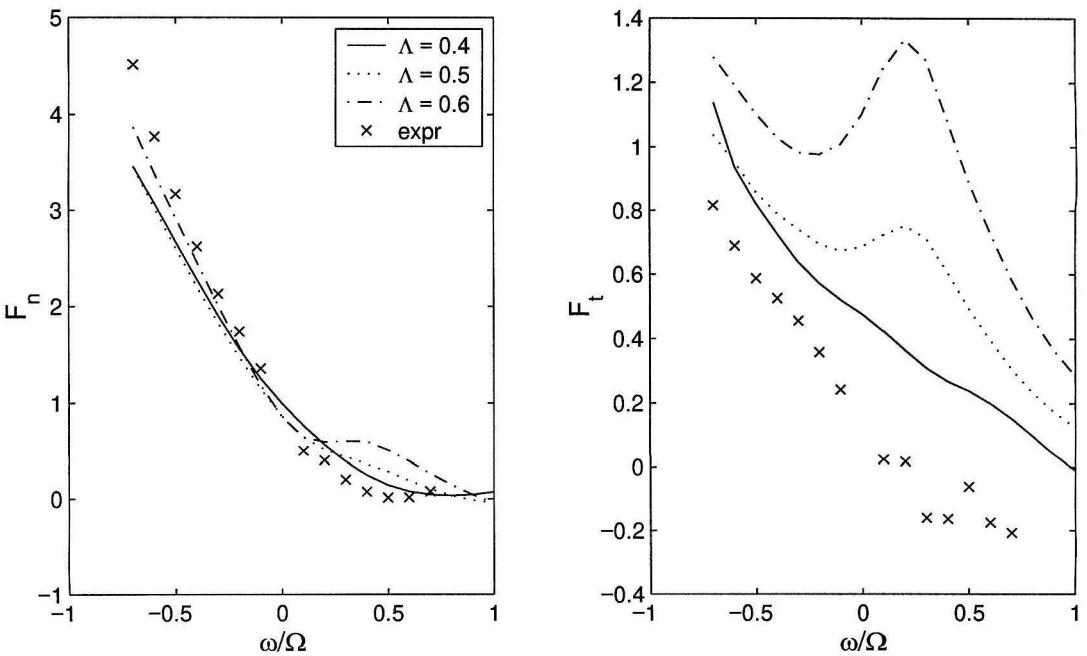

Figure 5.29: Calculated rotordynamic forces on the conical impeller with flow coefficient of 0.053, no inlet loss, exit jet loses all dynamic head. Pressure drops are 0.70, 0.79, 0.89

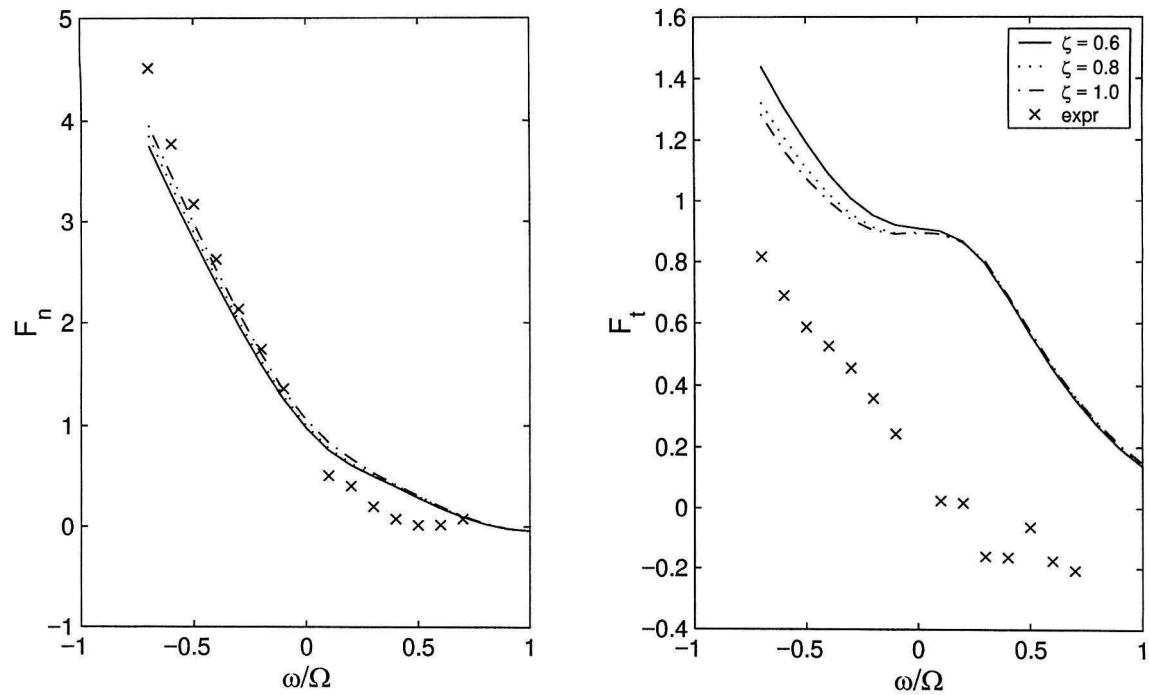

Figure 5.30: Calculated rotordynamic forces on the conical impeller with flow coefficient of 0.053 for different exit loss coefficients

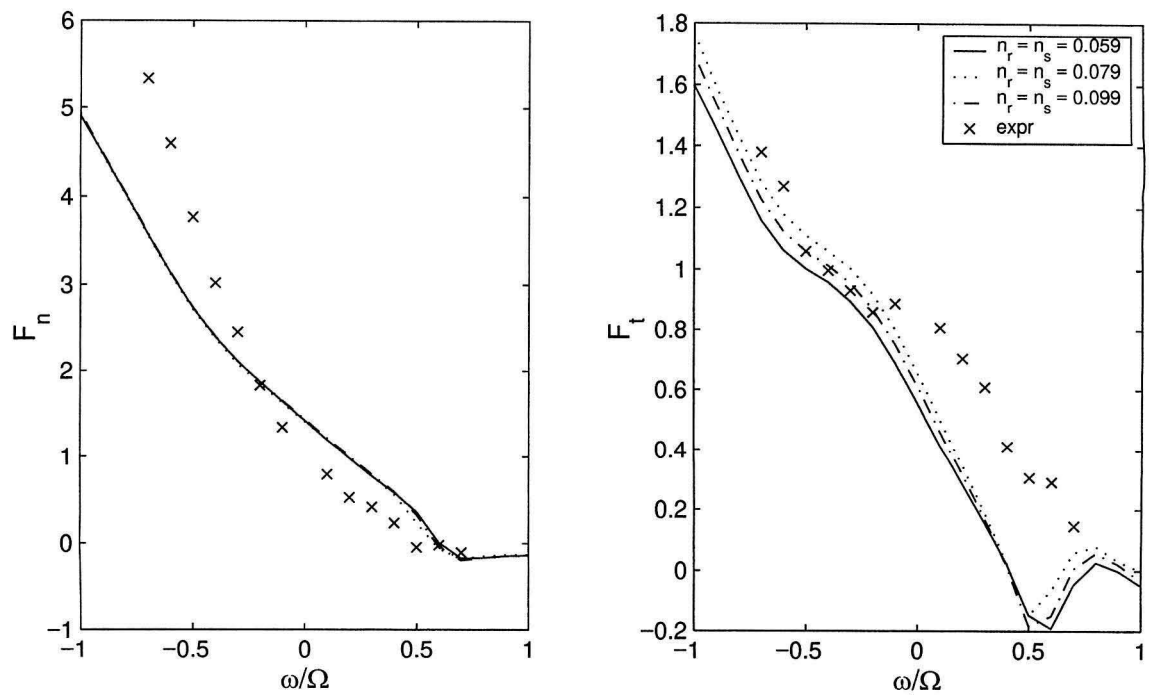

Figure 5.31: Calculated rotordynamic forces on the contoured impeller with flow coefficient of 0.053 for different shear stresses coefficients

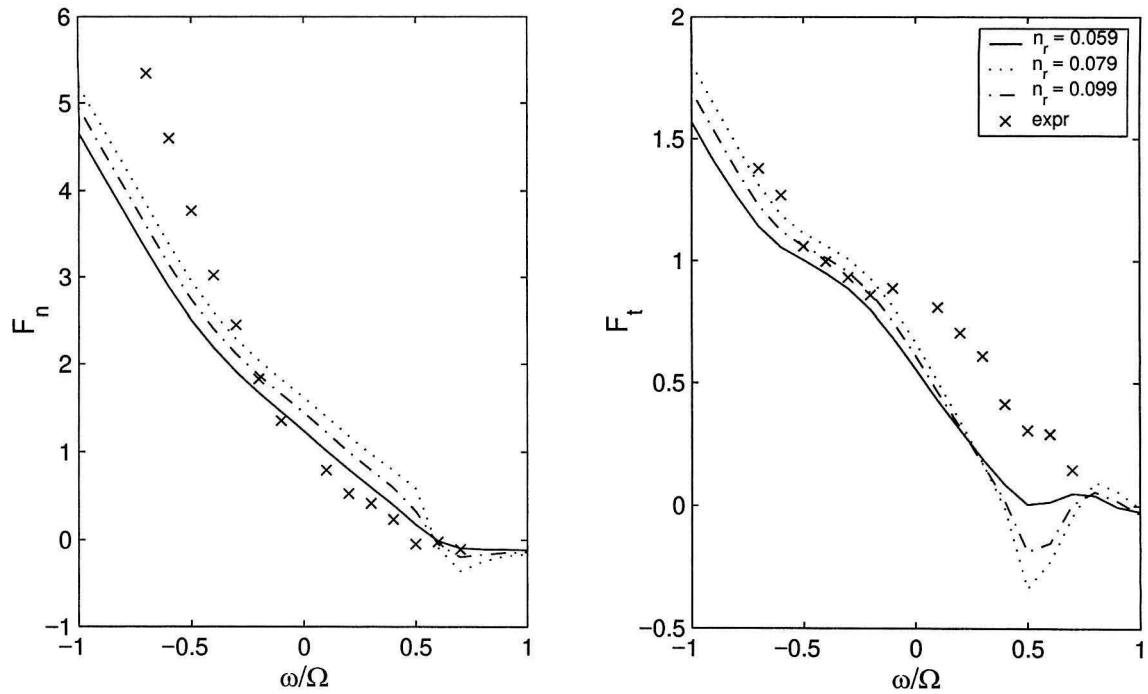

Figure 5.32: Calculated rotordynamic forces on the contoured impeller with flow coefficient of 0.053 for different shear stress coefficients

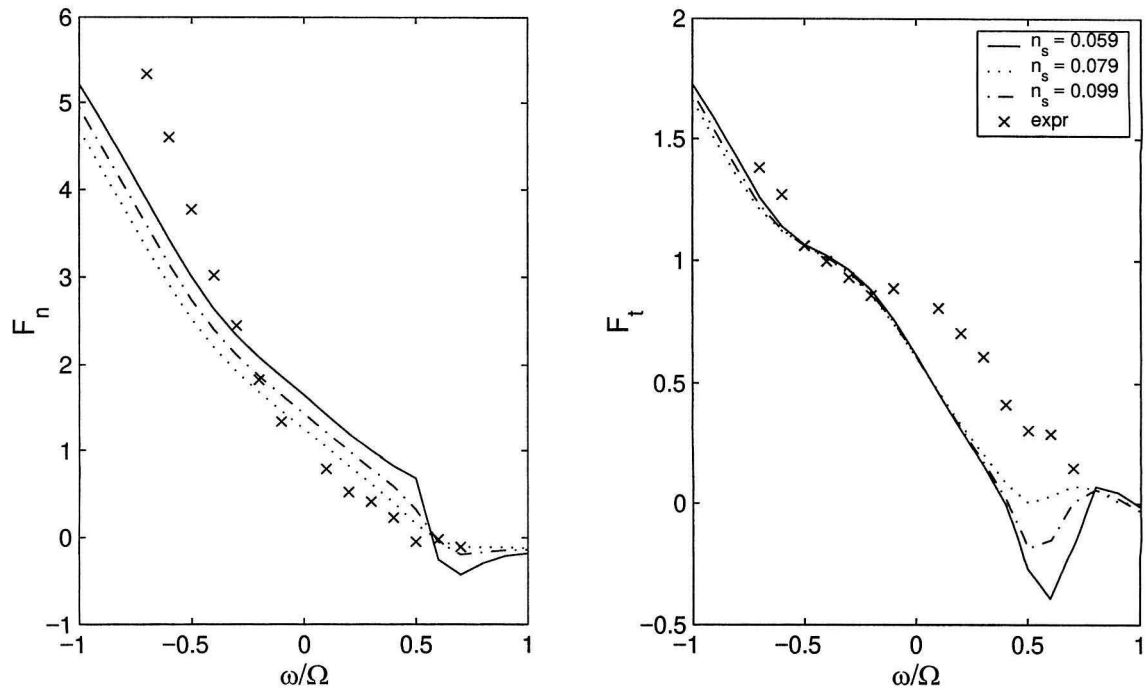

Figure 5.33: Calculated rotordynamic forces on the contoured impeller with flow coefficient of 0.053 for different shear stress coefficients

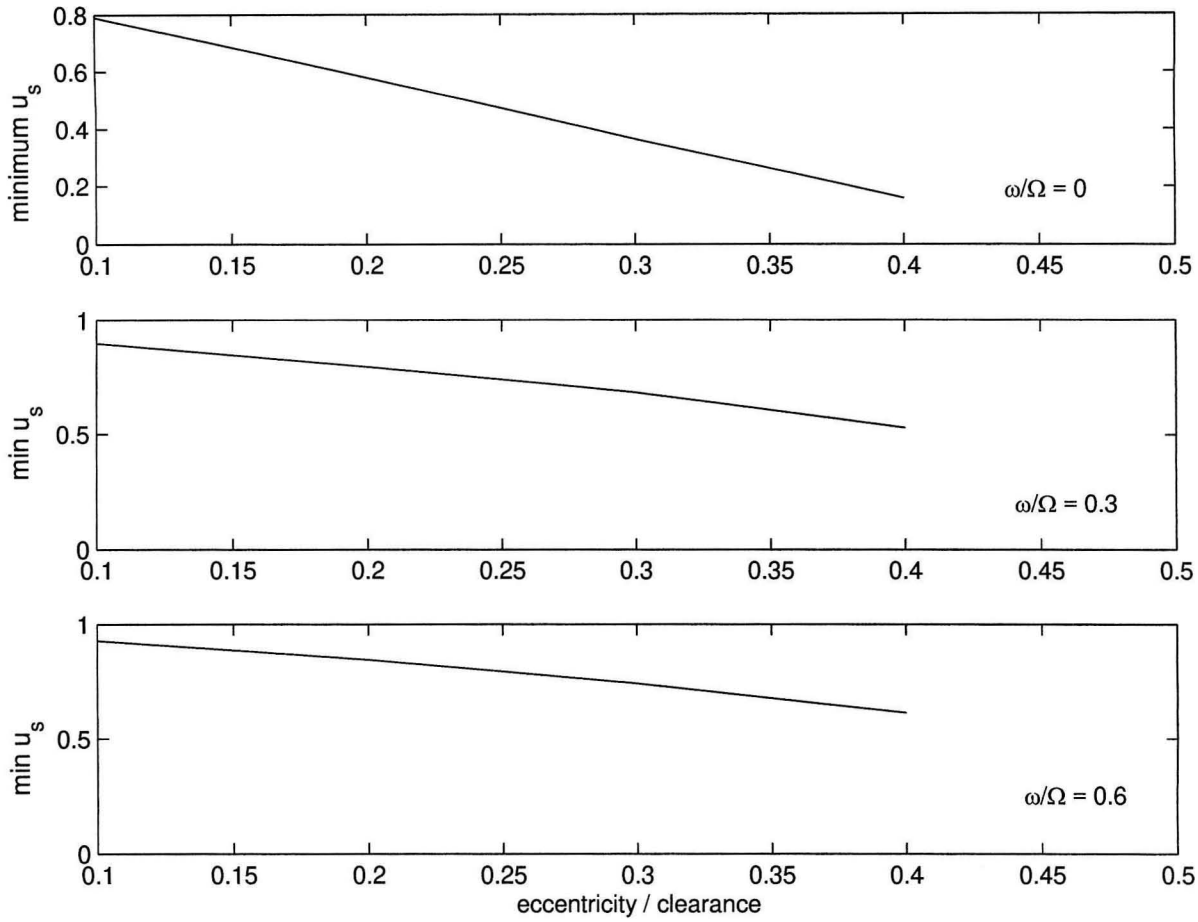

Figure 5.34: Plot of the smallest meridional velocity relative to average velocity against eccentricity for $\phi = 0.065$ at three different whirl frequency ratios

will be described in detail in the subsection that follows.

5.7.1 Prediction of Resonance in Rotordynamic Forces

The existence of resonance in the rotordynamic forces generated by the discharge to inlet leakage flow of a centrifugal pump has been a point of contention. The fact that the Childs' bulk flow equations predict these resonances for an inlet swirl of greater than 0.5 times the tip velocity has been widely reported (Childs, 1987). That, however, was only based upon calculating the rotordynamic forces at whirl frequency ratios in multiples of 0.1. From figure 5.35 it is obvious that the resonance shows up for the calculated leakage flow with an inlet swirl of 0.27 between a whirl frequency ratio of 0.3 and 0.5. The current method, which uses the same bulk flow

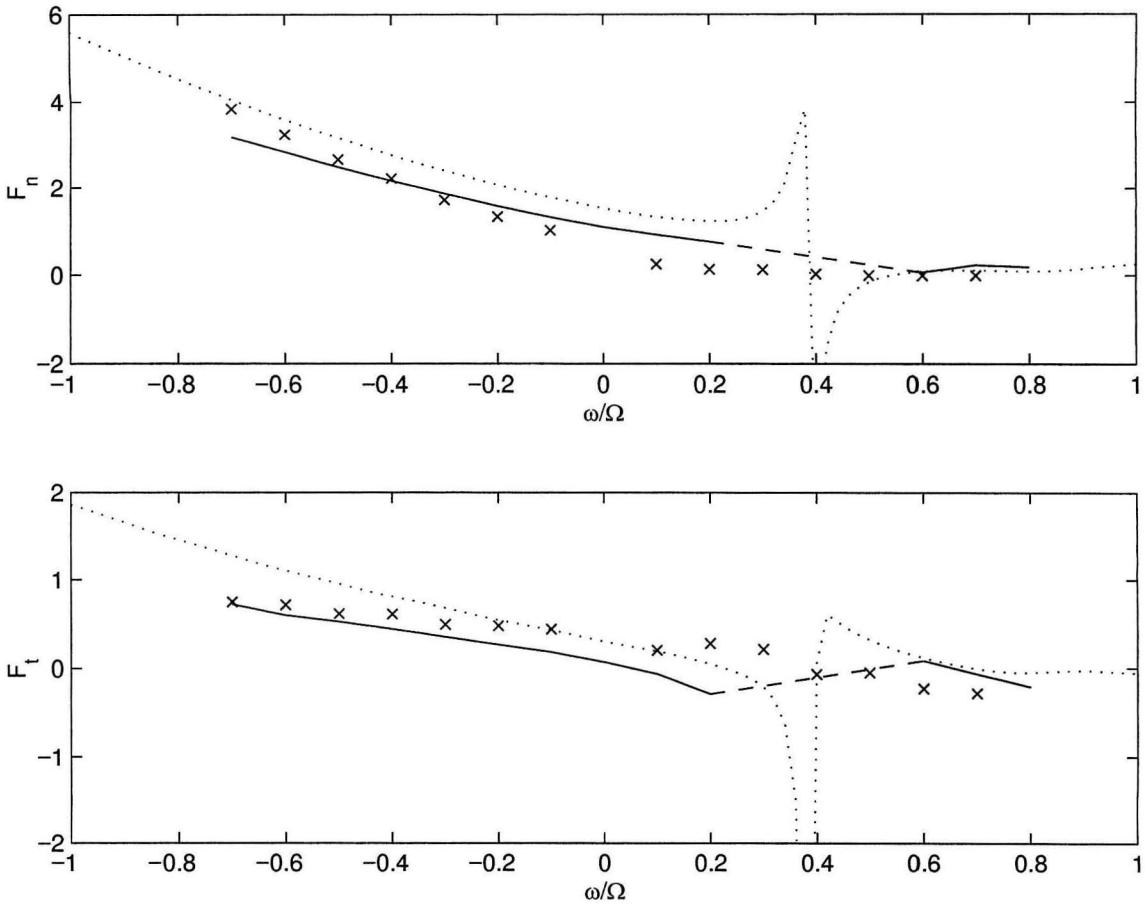

Figure 5.35: Rotordynamic forces for $\phi = 0.18$ and an inlet swirl of 0.27

equations, also behaves strangely in the same range of whirl frequencies: it did not converge. The calculations produce backflow at inlet to the leakage path, and the solutions do not then converge. Outside the troublesome range of whirl frequencies the two methods predict similar forces.

5.7.2 Courant Condition

As mentioned in the previous section, equations 4.17 and 4.35 was solved using forward integration in the meridional direction. An inspection of the two equations yields a characteristic velocity of $u_\theta/(Ru_s)$. Convergence for forward integration schemes depend on satisfying the Courant condition. In this case the Courant constant need

to be less than 1.

$$\frac{\Delta s}{\Delta \theta} \frac{u_\theta}{R u_s} < 1 \tag{5.1}$$

The constant is generally largest at inlet to the leakage path, and is larger for more negative whirl frequencies. In most of the calculations, a ten to one ratio of the number of grids in the meridional direction to that in the circumferential direction provided an adequate stability margin, with the exception of those cases mentioned in the preceding subsection.

5.8 Discussion

The current stream function vorticity method shows promise in predicting rotordynamic forces in both leakage paths and seals. In particular, the tangential forces are accurately predicted using the measured inlet swirl rate. The direct stiffness also matches the experimental results, while the direct added mass is significantly underpredicted. However, it might be expected that the curvature of the normal force curve would be difficult to predict accurately.

The calculations for the seal show similar trends to those for the conical impeller, with good matches for the tangential forces and the direct stiffness and poor predictions for the added mass. Calculations for the contoured impeller still require more study as the agreement between numerical and experimental results are not as good.

We should summarize the errors of predictions of rotordynamic force coefficients induced by fluid flows in the leakage path. The added mass term is always underpredicted and calculation results are not reliable; the experimental values are generally two to three times the numerical ones. The predictions of direct stiffness and the direct damping coefficients are fair, usually within twenty percent of the experimental results, sometimes even better. The cross-coupled stiffness and the cross-coupled damping coefficients are generally not as good; they usually experience about fifty percent deviation from the experimental results.

Chapter 6 Conclusion

For a rotating system such as the turbopump, rotordynamic forces will be generated by the movements of the impeller in its fluid environment. These fluid-induced forces generated in the annular flows surrounding the rotor are important because they can affect the dynamics of the entire rotating system, such as reducing the critical speed or the stability margins of the system. With some simplifications, the rotordynamic forces can be decomposed into the direct stiffness, cross-coupled stiffness, and the direct damping components. A negative direct stiffness is destabilizing and decreases the critical speed of the impeller. For low Reynolds flows, the rotordynamic force resulting from a positive direct stiffness has a centering effect, while for high Reynolds flows, the Bernoulli effect results in a negative direct stiffness and a destabilizing radial force. The cross-coupled stiffness and the direct damping coefficients are almost always destabilizing for rotordynamic forces and reduce the region of stability for the operating speed of the system.

Rotordynamic forces from the tip-to-eye leakage flow along the front shroud of the impeller have not been examined extensively. This thesis has studied these forces both experimentally and computationally. The experimental investigation consisted of measuring the effects of anti-swirl devices such as grooves and brakes in the leakage path of a centrifugal impeller on reducing the destabilizing fluid induced forces. Pressure profiles within the leakage flows were also measured as a diagnostic to indicate the nature of this flow. These experimental pressure profiles raised questions as to the validity of some assumptions concerning the inlet swirl velocities to the leakage path in earlier tests conducted at Caltech.

Inlet swirl is known to affect the tangential rotordynamic forces significantly in the case of annular seals. Various tests were conducted by previous students (Guinzburg, 1992; Uy *et al.* , 1997) to study the effects of inlet swirl on forces from leakage flows using inlet swirl vanes to prescribe pre-rotation for fluid entering the leakage path.

Several inlet swirl vanes were designed with varying turning angles as well as a set of radial anti-swirl vanes intended to prevent any inlet swirl by the fluid. Experiments described in this thesis showed that the inlet swirl vanes did not work as originally intended. Present tests showed that at lower flow rates the tangential velocity at inlet to the leakage path is nearly constant for all inlet swirl vanes. This explains why earlier measured rotordynamic forces did not show any effect for different nonzero inlet swirls. The anti-swirl vanes, however, worked as designed for higher flow rates, producing zero inlet swirl for larger flow coefficients. An examination of the experimental data of the effects of these two inlet swirl velocities on the rotordynamic forces show good qualitative match with those predicted by the bulk flow computations. They both agree that an increase in inlet swirl is destabilizing for both the normal and the tangential forces.

Since the effect of inlet swirl is destabilizing, reducing the swirl inside the leakage path also seems advisable. Tests conducted with swirl reduction devices inside the leakage path showed that their presence indeed offered some benefits at low flow coefficients. The results were mixed, however, at higher flow rates. The devices contributed to reduce unstable normal forces but greater destabilizing tangential forces. More experiments on different types of swirl reduction devices may be done. Examinations of the effects of circumferentially directed or helically shaped brakes and grooves could be done. Since the inlet swirl vanes did not work, a more thorough examination of the effects of inlet swirl ratio on rotordynamic forces for much higher inlet swirl ratios seems difficult to achieve. However, for experiments with swirl reduction devices, an impeller with blades can be tested to examine the effects of swirl reduction devices on an impeller with more typical inlet swirl velocities into the leakage path.

Because of the variety of different geometries for the leakage path, pump designers can not simply look up the values of the fluid induced forces. Experimental measurements can be time-consuming and expensive; therefore, numerical predictions for rotordynamic forces are useful. Computationally, the basic equations for the bulk flow model, which has traditionally been used in rotordynamic analysis, were recast into evolutionary equations for vorticity and total pressure. The bulk flow

characterizes the flow inside an annular region by velocities averaged over the gap. Therefore it will have only two velocity components, one in the meridional direction; the other tangential. The only shear stress contributions in the model will be from the solid-fluid interfaces. The shear stresses are modelled empirically using correlations from steady turbulent pipe flows. By restricting the analysis to axisymmetric rotors and stators, a coordinate transformation eliminated the time dependence and a solution method was developed without the assumption of harmonic forms of the flow variables. The numerical solutions are compared to experimental results for a seal geometry in addition to discharge-to-inlet leakage geometries. Results for the seal show very good agreement for the tangential forces. Predictions for the normal forces, however, exhibited a large offset to the experimental results, which can be reduced by changing the exit loss coefficient. Questions remain as to the reason for this discrepancy.

For leakage path geometries, good agreement with experimental results for the conical impeller was found with the exception of the added mass term. Predictions for the two contoured impeller geometries were not quite as good but are qualitatively similar. Compared to the Childs' perturbation solution method, the current method is more computationally intensive, though still relatively fast, and has more convergence problems. It also provided better predictions for most of the rotordynamic coefficients with the exception of cross-coupled damping term. At present, it does not treat backflow, a consideration for future work. Designers of turbomachinery may use the algorithm to find the magnitude of the expected fluid forces and incorporate them into the design process. Though many questions may persist regarding scaling effects on the shear stress coefficients, there are no currently better choices for those coefficients than those developed during the present investigation. Thus only the Reynolds number effects on the shear stress stress terms need to be adjusted in applying the present methodology. Larger scale problems would have increased Reynolds numbers, which would affect the shear stresses in the bulk flow model. Possible future work on computations include extending the work to compressible flow to model forces acting on compressors. Better understanding of the resonance behavior in the calculations

for certain flow parameter would also be beneficial.

This thesis has shown that the bulk flow model can predict many of the behaviors of rotordynamic forces induced by annular flows. The dependence of these forces on the inlet swirl velocities to leakage path was confirmed. Good predictions for most rotordynamic coefficients are obtainable from the current solution method. The predicted resonances in rotordynamic forces under certain conditions were non-existent experimentally, showing that greater understanding of whirling annular flows is still needed.

Bibliography

BASKHARONE, E., & HENSEL, S. 1991. A Finite Element Perturbation Approach to Fluid/Rotor Interaction in Turbomachinery Elements: Part I. *ASME J. Fluids Eng.*, **113**, 353–361.

BASKHARONE, E.A., & WYMAN, N.J. 1999. Primary/Leakage Flow Interaction in a Pump Stage. *ASME J. of Fluids Engineering*, **121**, 133–138.

BJORKLUND, I., & KAYS, W. 1959. Heat Transfer Between Concentric Rotating Cylinders. *ASME J. Heat Transfer*, **81**, 175–500.

BLACK, H.F. 1969. Effects of Hydraulic Forces in Annular Pressure Seals on the Vibrations of Centrifugal Pump Rotor. *J. Mech. Eng. Sci.*, **11**, 206–213.

BOLLETER, U., WYSS, A., WELTE, I., & STURCHLER, R. 1987. Measurement of Hydraulic Interaction Matricies of Boiler Feed Pump Impellers. *ASME J. of Vibration, Acoustics Stress and Reliability in Design*, **109**, 144–151.

BOLLETER, U., LEIBUNDGUT, E., STURCHLER, R., & MCCLOSKEY, T. 1989. Hydraulic Interaction and Excitation Forces of High Head Pump Impellers. *Pumping Machinery, 3rd Joint ASCE/ASME Mechanics Conference*, **81**, 187–193.

CHILDS, D. W. 1983a. Dynamic Analysis of Turbulent Annular Seals Based on Hirs' Lubrication Equation. *ASME J. Lubr. Tech.*, **105**, 429–436.

CHILDS, D. W. 1983b. Finite Length Solutions for Rotordynamic Coefficients of Turbulent Annular Seals. *ASME J. Lubr. Tech.*, **105**, 437–445.

CHILDS, D. W. 1987. Fluid Structure Interaction Forces at Pump-Impeller-Shroud Surfaces for Rotordynamic Calculations. *ASME Symp. on Rotating Machinery Dynamics*, **2**, 581–593.

CHILDS, D. W. 1989. Fluid Structure Interaction Forces at Pump-Impeller-Shroud Surfaces for Rotordynamic Calculations. *ASME J. Vibration, Acoustics, Stress and Reliability in Design*, **111**, 216–225.

FONGANG, R., COLDING-JORGENSEN, J., & NORDMANN, R. 1998. Investigation of Hydrodynamic Forces on Rotating and Whirling Centrifugal Pump Impellers. *ASME J. of Turbomachinery*, **120**, 179–185.

GUELICH, J., FLORJANCIC, D., & PACE, S. 1989. Influence of Flow Between Impeller and Casing on Part-Load Performance of Centrifugal Pumps. *Pumping Machinery, 3rd Joint ASCE/ASME Mechanics Conference*, **81**, 227–235.

GUINZBURG, A. 1992. *Rotordynamic Forces Generated by Discharge-to-Suction Leakage Flows in Centrifugal Pumps.* Ph.D. thesis, California Institute of Technology.

GUINZBURG, A., BRENNEN, C.E., ACOSTA, A.J., & CAUGHEY, T.K. 1993. The Effect of Inlet Swirl on the Rotordynamic Shroud Forces in a Centrifugal Pump. *ASME J. Eng. for Gas Turbines and Power*, **115**, 287–293.

HIRS, G. G. 1973. A Bulk-Flow Theory for Turbulence in Lubricant Films. *ASME J. Lubr. Tech.*, April, 137–146.

JERY, B. 1986. *Experimental Study of Unsteady Hydrodynamic Force Force Matricies on Whirling Centrifugal Pump Impellers.* Ph.D. thesis, California Institute of Technology.

MARQUETTE, O. 1995. *Experimental Versus Theoretical Comparison of the Static and Dynamic Characteristics of One Smooth and Two Grooved Liquid Annular Seals with L/D = 0.45.* Tech. rept. TL-SEAL-5-95. Texas A&M Turbomachinery Laboratory.

MORRISON, G.L., JOHNSON, M.C., & TATTERSON, G.B. 1991. 3-D Laser Anenometer Measurements in a Labyrinth Seal. *Intl. J. of Engineering for Gas Turbines and Power*, **113**, 421–427.

MORRISON, G.L., WINSLOW, R.B., & THAMES, H.D. 1996. Phase-Averaged Wall Shear Stress, Wall Pressure, and Near-Wall Velocity Field Measurements in a Whirling Annular Seal. *Intl. J. of Engineering for Gas Turbines and Power*, **118**, 590–597.

NG, S. 1976. *Dynamic Response of Cavitating Turbomachines.* Ph.D. thesis, California Institute of Technology.

NORDMANN, R., & MASSMANN, H. 1984. Identification of Dynamic Coefficients of Annular Turbulent Seals. *Proceedings of Workshop on Rotordynamic Instability Problems in High-Performance Turbomachinery, NASA Conf. Publ. 2338*, 295–311.

OHASHI, H., & SHOJI, H. 1987. Lateral Fluid Forces on Whirling Centrifugal Impeller (2nd Report: Experiment in Vaneless Diffuser). *ASME J. of Fluids Engineering*, **109**, 100–106.

SHOJI, H., & OHASHI, H. 1987. Lateral Fluid Forces on Whirling Centrifugal Impeller (1st Report: Theory). *ASME J. of Fluids Engineering*, **109**, 94–99.

SIVO, J.M., ACOSTA, A.J., BRENNEN, C.E., & CAUGHEY, T.K. 1994a. The Influence of Swirl Brakes and a Tip Discharge Orifice on the Rotordynamic Forces Generated by Discharge-to-Suction Leakage Flows in Shrouded Centrifugal Pumps. *Fifth International Symposium on Transport Phenomena and Dynamics of Rotating Machinery, ISROMAC-5*, **B**, 86–97.

SIVO, J.M., ACOSTA, A.J., BRENNEN, C.E., CAUGHEY, T.K., FERGUSON, T., & LEE, G. 1994b. Laser Velocimeter Measurements in the Leakage Annulus of a Whirling Centrifugal Pump. *ASME Laser Anemometry-1994, Advances and Applications*, **FED-191**, 111–117.

SIVO, J.M., ACOSTA, A.J., BRENNEN, C.E., & CAUGHEY, T.K. 1995. The Influence of Swirl Brakes on the Rotordynamic Forces Generated by Discharge-

to-Suction Leakage Flows in Centrifugal Pumps. *ASME J. Fluids Eng.*, **117**, 104–108.

SMITH, G.P., & TOWNSEND, A. 1982. Turbulent Coutte Flow between Concentric Cylinders. *J. Fluid Mechanics*, **123**, 187–217.

TOWNSEND, A. 1984. Axisymmetric Coutte Flow at Large Taylor Numbers. *J. Fluid Mechanics*, **144**, 329–362.

TSUJIMOTO, Y., YOSHIDA, Y., & OHASHI, H. 1997. Fluid Force Moment on a Centrifugal Impeller Shroud in Precessing Motion. *ASME J. of Fluids Engineering*, **119**, 366–371.

UY, R.V. 1998. *Studies of Rotordynamic Forces Generated by Annular Flows.* Ph.D. thesis, California Institute of Technology.

UY, R.V., BIRCUMSHAW, B.L., & BRENNEN, C.E. 1997. A Parametric Evaluation of the Effect of Inlet Swirl on the Rotordynamic Forces Generated by Discharge-to-Suction Leakage Flows in Shrouded Centrifugal Pump. *3rd Pumping Machinery Symposium, ASME Fluids Engineering Division Summer Meeting.*

UY, R.V., BIRCUMSHAW, B.L., & BRENNEN, C.E. 1998. Rotordynamic Forces from Discharge-to-Suction Leakage Flows in Shrouded Centrifugal Pumps: Effects of Geometry. *JSME International Journal: Fluids and Thermal Engineering*, **41, No. 1**, 208–213.